PHYSICAL AND COMPUTATIONAL MODELS OF MARANGONI AND BUOYANCY FLOW DURING DISSOLUTION

by

Aniruddha Chatterjee

B.Tech. (Mechanical Engineering), SRM University, Chennai, India, 2008

A THESIS SUBMITTED IN PARTIAL FULFILLMENT OF

THE REQUIREMENTS FOR THE DEGREE OF

MASTER OF APPLIED SCIENCE

in

THE FACULTY OF GRADUATE STUDIES

(Materials Engineering)

THE UNIVERSITY OF BRITISH COLUMBIA

Vancouver

August 2012

Abstract

During the production of titanium products, the presence of aluminum-rich regions can cause Type II alpha stabilized defects which are deleterious to down-stream performance. Al-rich material can enter the melt via ballistic transfer from the melting hearth at various stages during electron beam cold hearth re-melting (EBCHR) of Ti-6Al-4V (Ti-6wt%Al-4wt%V) alloy. If this material is not fully dissolved and homogenized when solidification occurs, the ingot will contain Al-rich regions. Thus, in order to produce high-performance components for aerospace applications, titanium producers must understand the dissolution process for alloying elements entering the melt.

To study and characterize the phenomena associated with the dissolution and homogenization of alloying elements during EBCHR processing of Ti-6Al-4V, a water-ethanol physical analogue model has been developed to simulate the thermal, compositional and fluid flow behavior that are active in the dissolution process. The physical model consists of a hot water solvent contained in a transparent cell (beaker) in which solidified ethanol or ice solute is dipped. The data generated from the physical model was used to validate a coupled thermal- fluid flow-composition model (developed in the commercial CFD code ANSYS CFX).

The analogue model focuses on characterizing the effects of thermal and compositional variations on surface tension driven fluid flow (Marangoni flow) and buoyancy driven flow during the dissolution of a low density, low surface tension and low melting point solid material (frozen ethanol) in a high density, high surface tension and high melting point liquid (water), which was found to be analogous to the dissolution of solid Al in liquid Ti. In addition, the analogue model was also capable to predict the dissolution behavior when there was no compositional difference between the solute and the solvent. Based on a comparison of fluid flow pattern and interface shape, and temperature data obtained at discrete locations in the experimental and computational results, the numerical model has been shown to quantitatively and qualitatively predict the dissolution behavior observed in the physical process.

Table of Contents

List of Tables

List of Figures

Acknowledgement

This thesis was made possible thanks to the help, support and encouragement of many people and I would like to give special thanks to the following:

I would like to express my immense gratitude to my advisor and teacher: Prof. Daan M. Maijer and Prof. Steven L. Cockcroft for all their inputs and suggestions in successfully conducting the research on understanding the transport processes during dissolution of alloying elements. I would not have learnt so much, if both my advisors would not have been so kind with their time and so patient with my faltering steps. I am thankful to them for giving lessons on the fundamentals of transport processes and solidification during the weekly meetings. They taught me more than what books could ever have. I am highly thankful to them for their constant help and support in improving my technical writing skills. Presenting at a conference like TMS was a dream and I am thankful to my advisors for showing their faith and confidence in me and help enriching my Master's experience. Without the constant guidance, insight, sound advice, ideas, suggestions and encouragement of Prof. Cockcroft and Prof. Maijer, this work simply could not have been possible. Furthermore, I would also like to express my deep thanks to Dr. Carl Reilly and Dr. Lu Yao for their time and patience in correcting my thesis for first revision. Finally, I am highly thankful to TIMET Corp. for their financial support during the course of my study.

I am indebted to many student colleagues at University of British Columbia for providing me a stimulating and fun environment:

Jun Ou, for many evenings of fruitful modeling discussions and help in understanding many technical aspects of the project; Rahul Lodha, for many outings to great restaurants in and around Vancouver to discuss on project related affairs, topics of materials science, cricket, current affairs and life, and; Abhijit Pandhari, for his continuous guidance in clearing many of my technical doubts during this journey. I would also like to thank my friends in the Casting group for their friendship and constant help and support: Zhongkui Zhang, Farzaneh Farhang Mehr, Jianglan Duan, Matt Roy to name a few.

Further, I wish to thank my close friends Gagandeep Kaur Chawla, Nishant Chandgotia, Swiya Nath, Vasu Vineet Tewari, Ricky Dua, Gourab Ray and Harshul Srivastava for their patience, love and support, care and friendship over the years. Without them, I would not have survived so far away from home.

Lastly, and most importantly, I wish to thank my parents, Arup and Sutapa Chatterjee, and my sister, Ipsita Chatterjee. They have supported me, taught me, motivated me, believed in me and loved me. To them I dedicate this thesis.

1   Introduction

1.1   Titanium Alloy: Ti-6Al-4V

Ti-6Al-4V, known as the "workhorse" alloy of the titanium industry, is one of the most common titanium alloys, representing more than half of the world-wide titanium usage. It has a high strength-to-weight ratio, excellent resistance to corrosion, high ductility, high melting point, and is bio-compatible. It's most important properties, high strength and ductility, result from the precise quantities of alpha and beta stabilizers in its composition [1]. Ti-6Al-4V is a commonly used material in engine components, structural components and fasteners for the aerospace industry. Other applications for this alloy include: high performance automotive parts, marine applications, medical devices and high-performance sport equipment [2].

Table 1.1 Chemical composition of a typical Ti-6Al-4V, in weight percent

Al	V	O	Fe	Mo	C	Si	Mn
6.31	4.06	0.18	1.16	0.02	0.016	0.01	0.01
Cu	B	Zr	Y	N	Sn	Cr	Ti
0.02	0.001	0.02	0.001	0.008	0.02	0.01	Bal.

In pure titanium, the alpha phase (HCP) is stable up to 882 ℃ and the beta phase (BCC) is stable from 882 ℃ to the melting point, 1650 ℃. The temperature at which the alpha phase transforms to the beta phase is called the beta transition, or transus, temperature. The transus temperature and the equilibrium amounts of each phase changes with the addition of alloying elements. The addition of aluminum, gallium, or germanium to pure titanium stabilizes the alpha phase by elevating the transus temperature. The addition of vanadium, chromium, columbium, copper, iron, manganese, molybdenum or tantalum leads to the stabilization of the beta phase by lowering the temperature of alpha-to-beta transformation. The chemical composition of typical Ti-6Al-4V is shown in **Table 1.1** [3]**.** Ti-6Al-4V contains a mixture of both alpha and beta phases and is therefore known as an 'alpha-beta alloy'. The net

result of adding aluminum and vanadium to titanium to create Ti-4Al-6V is an increase in the beta transition temperature to 996 ℃ [4], [5].

1.2 Production of Titanium Alloys

The manufacturing method used for the production of titanium castings, forgings and mill products has essentially been the same since the 1940s. The commercial process for the production of titanium alloy components consists of three main stages as shown in **Figure 1.1**: Sponge production; Melting and Conversion.

During reduction, titanium sponge is produced following the reduction of ore using the commercial batch process called the Kroll process. Titanium sponge can be consolidated along with titanium scrap using one of the primary melting and casting operations called the Electron Beam Cold Hearth Re-melting (EBCHR) process, to produce ingot. Ingot is further processed or converted to the required shape of a billet or bar or sheet.

1.2.1 Sponge Production

Titanium sponge is produced using a multi-step batch process pioneered by Dr. Wilhelm J. Kroll in the 1930's [6]. Rutile (TiO_2) and Ilmentite ($FeTiO_3$) ores are two common sources of titanium. The reduction of Ilmentite ore to produce Fe, leaves behind a Ti-rich slag in the form of TiO_2 (rutile), which is then further reduced to titanium metal by means of a metallothermic reduction process [7, 8]. Rutile ore often contains fewer impurities compared to Ilmentite and is therefore preferred.

Figure 1.2 gives an overview of the Kroll process as practiced in industry today. Chlorination occurs in a chlorinator, which contains a fluidized bed of TiO_2, carbon and impurities from the ore. Chlorine gas, passed in at the bottom of the chlorinator, reacts with Ti to form $TiCl_4$, which is then purified using fractional distillation. The next step is the controlled reduction of $TiCl_4$ in an inert atmosphere, in the presence of metallic Mg (heated to $800 - 850\ ^oC$), to produce titanium and $MgCl_2$. After the Mg has been totally consumed, the $MgCl_2$ is removed and further processed in an electrolytic cell. The titanium sponge that remains is crushed prior to melting to form ingots [9], [10].
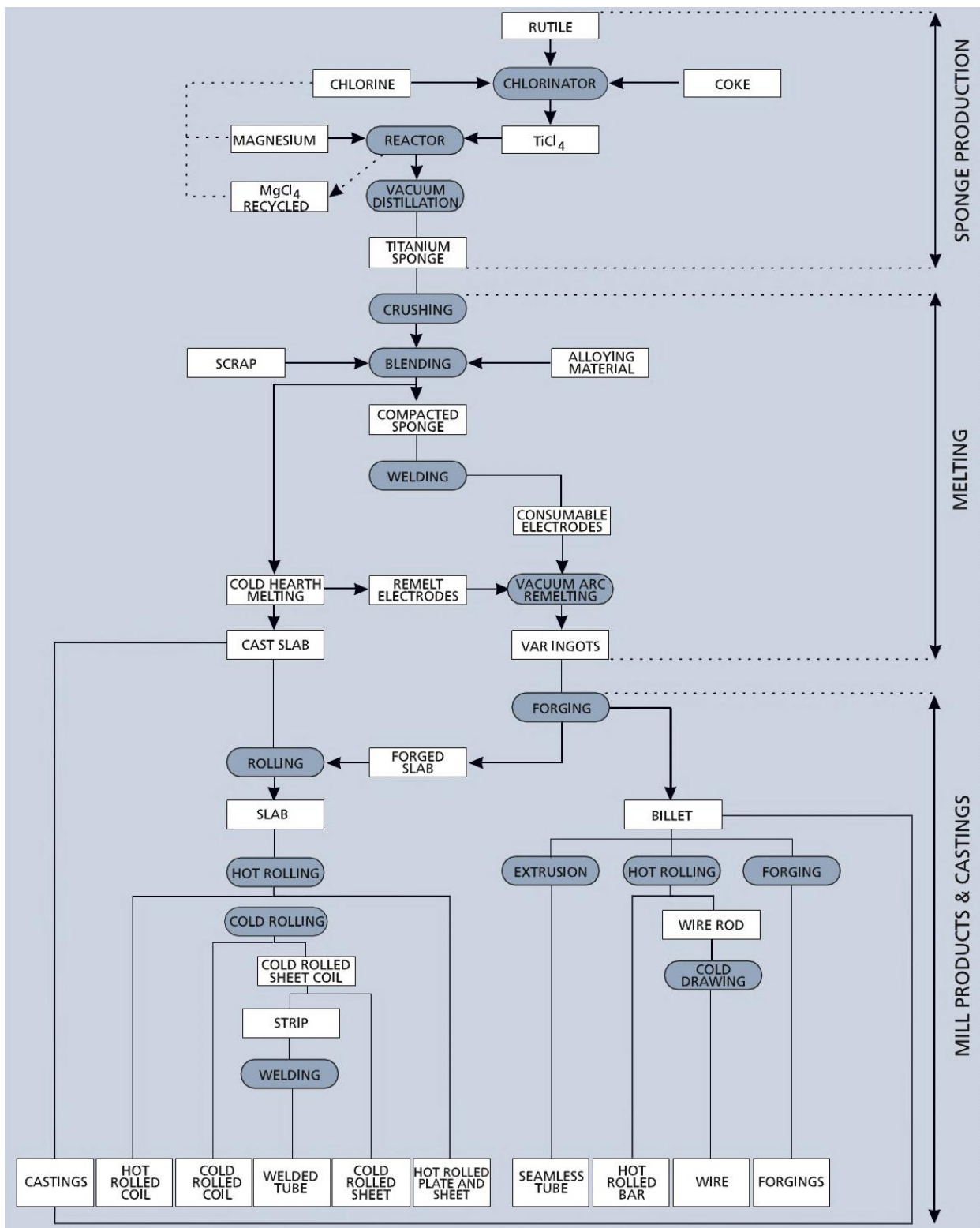
Figure 1.1 Production flow chart for Titanium sponge, mill products & castings [11]
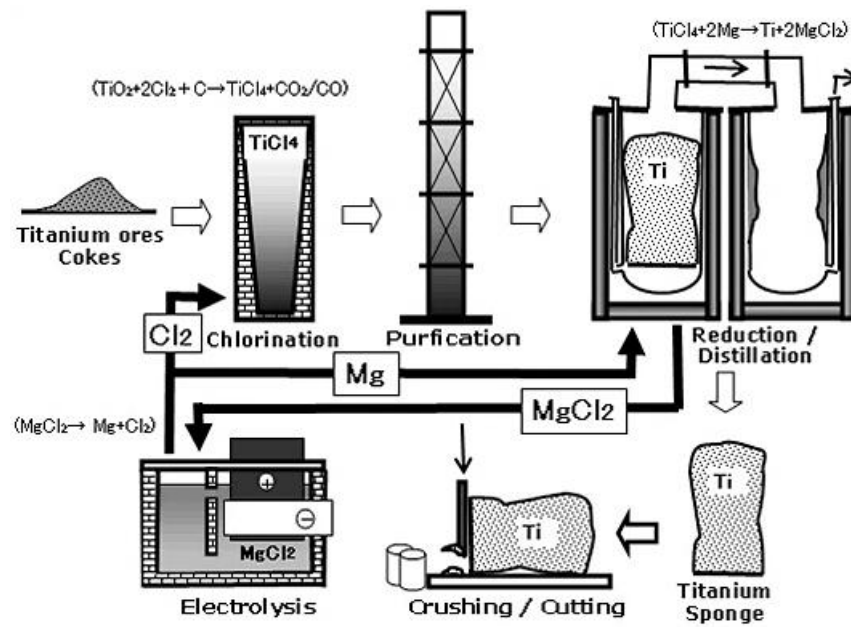
Figure 1.2 Overview of titanium sponge production [12]

1.2.2 Melting

Consolidation and alloying of titanium is performed through some combination of Vacuum Arc Re-melting (VAR) and/or Cold Hearth Re-melting (CHR) with either Electron Beam or Plasma Arc technologies. The specific combination and sequence of melting technologies used is based on customer requirements. In particular, the CHR process is typically followed by multiple VAR steps to produce rotating-grade alloy that can be used in turbine engines.

Prior to the VAR process, sponge titanium is crushed and blended in a carefully controlled manner with its alloys and scrap titanium (revert) to the desired composition. This composition is then pressed into compacts, welded to form consumable electrodes. Al, Cr, Cu, Fe, Mn, Sn and Zr are easy to add but Si and other refractory elements are conveniently and economically added as alumothermic reduced master alloys. Oxygen is added as powdered TiO_2 and nitrogen is occasionally added in very small quantities to impart strength [13].

A VAR furnace consists of a water cooled copper crucible, vacuum system, electrode drive and control system as shown in **Figure 1.3**. Initially, the furnace is pumped down to create the optimum vacuum and the electrode is lowered towards a layer of titanium in the water-cooled copper crucible. A

4

DC voltage is applied to the electrode and increased until an arc initiates between the electrode and the titanium in the crucible (arc length often a few centimeters). The arcing melts the electrode and the melted material eventually solidifies in the water-cooled copper mould. The magnetic field developed by the induction coils lead to electromagnetic stirring of the melt pool. By periodically reversing the coil current, the stirring direction is alternated. Once the entire electrode has been melted and the resulting ingot has solidified, the ingot is removed and then ground to remove surface defects and contaminants. A second re-melt is undertaken to ensure homogeneity and dissolution of inclusions. A third re-melt is also performed for metals for use in very high reliability or critical applications, like: turbine engine components. VAR ingots are cylindrical in shape, weighing several thousand pounds, and can be forged to slabs or billets and then converted to mill products [11],[10],[14], and [15].

(a)   **(b)**
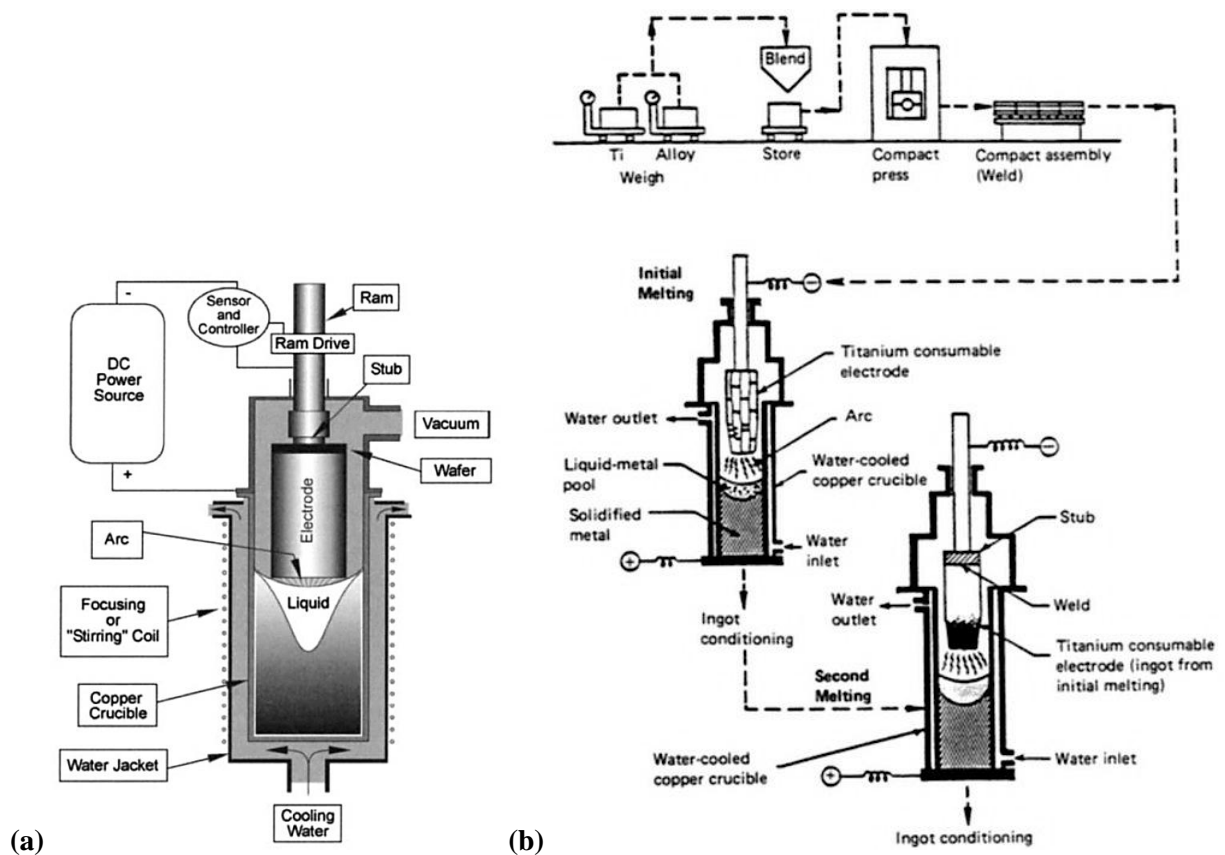
Figure 1.3 Process layout of Double Vacuum Arc Re-melting [10], [16]

5

The most important advantages of the VAR process are that the solidification rate can be controlled, the microstructure development can be controlled, and solidification is directional from the bottom to top which prevents macro-segregation and reduces micro-segregation thereby enhances the material properties of the solidified ingot. There are several other advantages including the ability to remove dissolved gases, such as nitrogen, oxygen and hydrogen, from the liquid metal. Finally, it lowers the concentration of high vapor pressure elements like carbon, sulphur and magnesium [17]. The key disadvantages of the VAR process include the high cost of production due to the labor intensive electrode preparation, the multiple melt requirement, the retention of undesirable low or high density inclusions [18], and intermediate and final conditioning with its associated yield loss (turning and grinding of the surface and removal of the ingot ends) [11], [7].

The second common consolidation process, cold hearth re-melting, operates by melting the titanium with a high intensity heat source in a water cooled copper hearth followed by some form of casting process. A "skull" of solidified titanium forms against the hearth protecting the hearth from damage and allowing the liquid metal to flow along a channel formed by an autogenous lining. There are two commonly used forms of CHM: Plasma Arc Re-Melting (PAM) and Electron Beam Cold Hearth Re-melting (EBCHR). **Figure 1.4 (a)** shows an image of the PAM process and **Figure 1.4 (b)** shows an image of the EBCHR process.

(a)   (b)
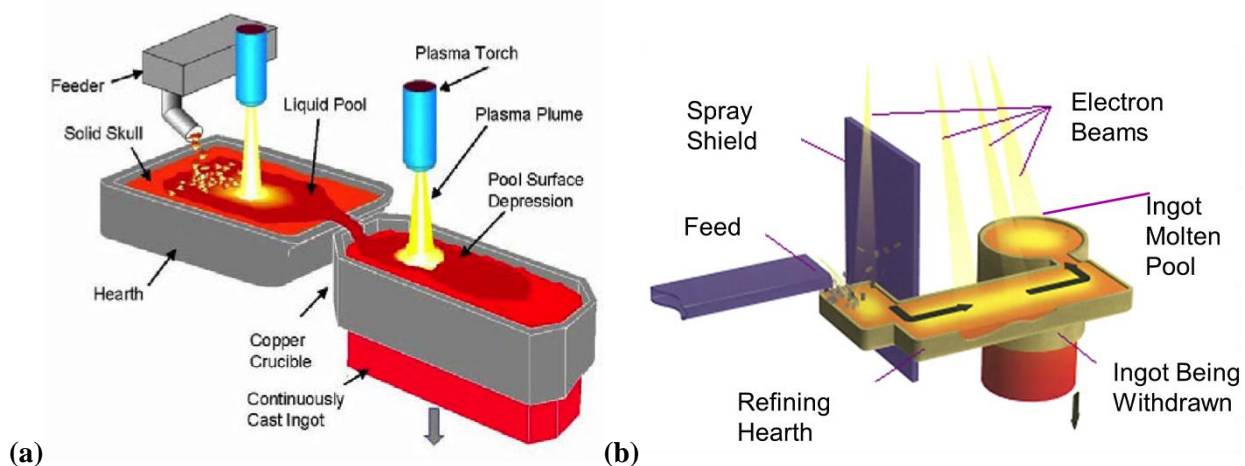
Figure 1.4 Schematic representation of (a) Plasma Arc Melting process [19] **and (b) EBCHR process for continuous casting**

6

In CHR, sponge and alloying elements are crushed and mixed with recycled titanium scrap before being melted. In both CHR processes, there may be one or more melting hearths where the raw materials are added [11]. The feed material is melted using multiple plasma arcs or electron beams. PAM is operated with a positive or reduced pressure of Helium/Argon which shields the titanium from contamination with oxygen and nitrogen, while EBCHR is carried out under a high vacuum to prevent the dispersion of the electron beams and limit oxygen and nitrogen pick-up. In both cases, the heat input is enough to melt the titanium and to keep it molten as it flows along the hearth into the casting mould. As the metal flows along the hearth impurities are able to either sink to the bottom or evaporate depending on their nature. The molten titanium is directly cast into ingots for further downstream deformation processing or for re-melting as electrodes in the VAR process to meet high precision aerospace requirements. The combination of CHR-VAR processing has been shown to eliminate inclusions/defects that triple VAR melt processing cannot remove [11].

The advantages of the CHR process, in comparison to VAR includes: improved scrap melting capabilities due to its ability to remove high density inclusions by gravity settling and entrapment in the mushy zone at the bottom of the hearth molten pool; improved process control; ability to cast both round ingots and rectangular slabs; improved economics due to the high percentage allowance of scrap and high production rate [7], [10]. All of these advantages are stated while noting the fact that CHR is a consolidation process before VAR.

As the current research is focused on the subject of EBCHR processing of titanium alloys, it is important to discuss and understand in detail the manufacturing process of titanium alloy ingots using this process. The EBCHR process is operated in a vacuum environment with pressures on the order of 10^{-5} Pa. The process consists of four regions: i) Feeding; ii) Melting; iii) Refining; and iv) Casting.

In the feeding region, the feed material consisting of virgin titanium sponge, alloying elements such as: aluminum, magnesium or vanadium and scrap material are introduced into the melting hearth. In the melting hearth, the solid feed material is melted using one or more high powered electron beams. During the melting process, the rapid heating provided by the electron beam can cause rapid expansion in the feedstock and may lead to the ballistic transfer of material to other regions of the process, such as the

casting region, refer to **Figure 1.4 (b)**. To help reduce this, the melting and casting regions are shielded from one another using a spray shield.

Once molten, the melt flows into and then along the refining hearth, which may consist of two sub stages to achieve the high purity targets. Whilst the material is flowing along the refining hearth, the low-density elements/inclusions either dissolve in the liquid metal or evaporate from the liquid pool after being exposed to the intense heating provided by the electron beams. At the same time, high-density elements/inclusions sink to the bottom and get trapped in the skull. The refining realized through CHR processing provides superior inclusion removal when compared to VAR. The vacuum environment necessary for EBCHR processing promotes significant evaporation of high vapor pressure elements such as Al and Cr, which-in-turn create challenges for chemistry control of the material.

In the casting section, the melt flows into a water cooled copper mould where it is cast into either rectangular slabs or round ingots of finite depth, depending on the needs of the application. The casting process is semi-continuous due to length constraints and therefore the casting process occurs in three phases: start-up, steady state and final transient state.

The advantages of EBCHR processing are the ability to efficiently refine large quantities of turnings, and the elimination of un-melted charge, high and low density inclusions and volatile elements (chlorine, hydrogen, etc.) [13]. EBCHR provides the versatility to use charge material which includes a high proportion of metal scrap and waste without complicated preparatory operations. It provides the flexibility to produce ingots and slabs of very different cross-sections. The main drawback of the EBCHR process is the significant losses of alloying elements such as Al, Cr by volatilization; high equipment cost; chemistry control of the as-cast ingot. [20]

1.3   Melt Defects in Titanium Castings
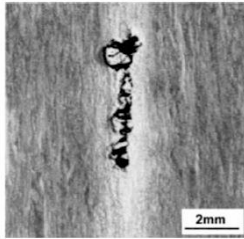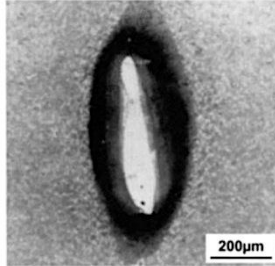
Considering the high cost of the extraction and production of titanium and the applications where it is used (i.e. highly safety critical aerospace applications), it is important to understand how defects form during the melting and consolidation processes and how they affect the material properties of the final
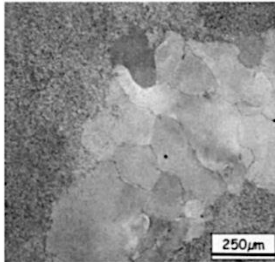
product. Therefore, a significant portion of this section is dedicated to understanding and characterizing melt related defects. It is because of the potential for these defects to form and their severe consequences that such expensive and comprehensive methods are used for titanium ingot production.

There are five principal types of defects in titanium [10], [13]. **Table 1.2** summarizes potential defects along with their primary cause and consequence, as well as how they can be eliminated during the melting stages to prevent catastrophic failure of the final product when in service. The table gives an indication of the complexity of producing defect-free titanium mill products for high performance applications and how defects alter the mechanical properties of the ingot if not eliminated. These defects once formed are hard to eliminate by subsequent processing steps and/or by re-melting. The primary source of these defects is inadequate melting or dissolution and homogenization of materials added as alloying elements or feed stock during metal processing. When material bypasses the melting hearth and is introduced into the melt pool, it can become a defect if the time required to melt and/or dissolve the materials is greater than the remaining process (cycle) time. Understanding the melting and/or dissolution of such material in the molten pool is difficult since it involves a complex combination of heat and mass transport. The extent of these transport phenomena is directly linked to the difference in the material properties, temperature and composition of the solid and molten pool. Further, the effects of the heat and mass transport associated with melting and/or dissolution of a solid particle in a molten pool are not clearly understood.

Therefore, the purpose of the research presented in this thesis is to improve the understanding of factors governing the melting and/or dissolution and homogenization of a solid melting in a liquid pool, especially that of solid Al in liquid Ti. Since there are difficulties associated with conducting experiments on liquid Ti, the ethanol-water system has been selected to study the flow behavior during dissolution via physical and computational models. This research work sets the stage for understanding the conditions that lead to the formation of alpha stabilizer rich region Type II defects.

Table 1.2 Key melt related defects in Titanium Ingots

Type of Defects	Causes of Occurrence	Features/ Characteristics	Consequences	Prevention
Low Density Hard Alpha defect – I (High Interstitial Defect, HID)	• Nitrogen rich compound TiN. • Sponge Production: - Fire during handling or shearing - Air contamination • Melt electrode production: - Fires during compacting - Improper conditioned scrap - Contaminated master alloy - Contamination, poor shielding during welding • Melting and re-melting: - Aggressive grinding during ingot conditioning - Water leak, Air leak • Unblended addition of TiO_2.	• Inclusions are hard and brittle. • High concentrations of oxygen and/or carbon. • An image of Type I nitrogen stabilized inclusion [10]: 2mm	• Causes fracture at relatively low stresses leading to incipient cracks. • Decrease the fatigue capability of the material. • Causes strain incompatibility between the matrix and the inclusion.	• Ultrasonic Inspection
Alpha stabilizer rich region II or, Soft Alpha Segregates	• Al-rich inclusions not adequately dissolved during EBM. • Improper removal of ingot top. • Improper final melt phase	• Large Al-rich regions • Less detrimental to properties than Type I defects • Unique to Ti-alloys and forms in shrinkage pipes. • Appear as light and dark etched lines in microstructure.	• These defects do not respond to heat treatment (aging) as much as the surrounding matrix and remain softer. • Deform preferentially in fatigue situations, leading to earlier crack nucleation. • Flaws can impair transverse mechanical properties.	• Can be eliminated by good "hot topping" practices. • Cropping the top portion of ingot. • Ingot homogenization
High Density Inclusions, HDIs	• Scrap additions: - Refractory metal carbides from carbide tool bits mixed with turning. - Tungsten welding electrodes (non-consumable during melting). (The above points are principal sources of Tungsten in melting hearth)	• High melting temperature of W and WC make these inclusions relatively stable during VAR. • Image below shows high density W inclusion [10]; dark etched matrix, adjacent to inclusion contains fine α precipitates in β-phase. This β-phase is enriched in W due to diffusion. 200μm	• Tungsten-rich high density inclusions resist melting and sink to the skull at the bottom of the pool.	• Allow permissible levels of turnings for different level of applications based on criticality.

Type of Defects	Causes of Occurrence	Features/ Characteristics	Consequences	Prevention
Beta stabilizer rich region - Beta Flecks	• Alloys containing β eutectoid forming elements: Fe, Cr, Mn, Ni, Cu. • Melting macro-segregation. • Conversion too close to transus. • (including adiabatic heating effects)	• Large localized concentration of beta-stabilized elements. • By heating α-β alloy close to its β transus temperature and cooling rapidly, flecks will be retained in macrostructures. • They partition to the liquid phase and lower its melting point. Some of this enriched liquid flows inter-dendritically as solidification and shrinkage occurs. • An image of Fe enriched region, known as beta fleck [10] is shown below: Size: Few hundred μm. to few mm.	• Solute segregation during ingot solidification. • Detrimental to the fatigue strength. • Site for early crack nucleation.	• Ingot homogenization.
Voids	• Gas entrapment during VAR. • Residual chloride in sponge, having no solubility in solid metal, forms vapor bubbles in liquid metal. • Improper conversion practices during casting.	• Shrinkage porosities, generally with inter-dendritic pore structure. • Size: Few microns to millimeters. • Spherical-shaped pores developed due to trapped gases.	• Large dendritic pores have serious consequences on the fatigue life.	• VAR essentially eliminates this defect.

2 Literature Review

During the EBCHR process, addition of alloy elements and scrap material into the hot molten metal pool (hearth) induces heat, fluid and mass transport. The fluid flow in the molten pool is strongly influenced by buoyancy (natural convection) and Marangoni (surface tension) forces. The buoyancy driven flow is induced in the metal pool by density differences that can occur by temperature gradients and/or concentration gradients. The addition of a particle into the molten liquid can become a surface phenomenon if the solid particle is of lower density and lower surface tension compared to the molten pool. Both buoyancy and Marangoni convection plays an important role in the transport of heat and mass within the pool. A discussion on the generation of surface tension driven forces has been presented in section 2.1. Section 2.2 reviews the information on how melting is different from dissolving and dissolution. Section 2.3 reports literatures published on mathematical models developed and experimental studies conducted in understanding the fluid flow and dissolution during EBM. While Section 2.4 reviews literatures on water model analogies to study their success in numerical validation and depicting the physical phenomena of interest.

2.1 Marangoni Flow

In the bulk liquid (sub-surface and below), all liquid molecules are surrounded by its neighboring molecules from all sides. Each of these molecules is pulled equally in every direction by their neighboring molecules such that the resulting net force is zero. But the liquid molecules at the surface have their neighboring molecules on their sides and below but not above them and therefore are pulled inwards which creates a surface tension. The resistance against extension of a free surface shows that the surface has an internal surface tension. When a region of lower or higher surface tension occurs in a liquid, the gradient in surface tension which develops gives rise to Marangoni flow on the surface. A region of liquid with high surface tension will pull more strongly on a low surface tension region causing a shear force on the surface which will lead the flow from regions of low surface tension to the regions of high surface tension. Such variation can arise from compositional variations and/or from temperature variations.

Surface tension generally decreases with rising temperature which is one of the reasons why hot water is used for washing. Unless balanced by other forces, shear surface forces cannot be sustained in a liquid at rest but will unavoidably set it into motion. Italian physicist, Carlo Guiseppe Matteo Marangoni formalized this while studying the effect of spatial variations in surface tension for his doctoral dissertation in 1865 [21, 22].

Mathematically, the Marangoni forces as a function of temperature or compositional differences are expressed as [23]:

$$M(T) = \frac{\partial \sigma}{\partial T}\frac{\partial T}{\partial n} \qquad\qquad \textbf{Eq. (2.1)}$$

$$M(C) = \frac{\partial \sigma}{\partial C}\frac{\partial C}{\partial n} \qquad\qquad \textbf{Eq. (2.2)}$$

where $M(T)$ is the thermal Marangoni force (N m^{-2}), $M(C)$ is the compositional (solutal) Marangoni force (N m^{-2}), σ is the surface tension (N m^{-1}), T is the temperature (K), C is the compositional fraction or mass fraction, n is a direction parallel to the surface (m), $\frac{\partial T}{\partial n}$ is the temperature gradient along the directional normal (K m^{-1}), $\frac{\partial C}{\partial n}$ is the composition gradient along the directional normal (m^{-1}), $\frac{\partial \sigma}{\partial T}$ is the surface tension coefficient with respect to temperature (N m^{-1} K^{-1}) and $\frac{\partial \sigma}{\partial C}$ is the surface tension coefficient with respect to composition (N m^{-1}).

2.2 Melting, Dissolving and Dissolution

During the melting and casting of titanium alloys (Ti-6Al-4V) in the EBCHR process, it is critical that aluminum-rich material is not carried over from the refining hearth to the cast ingot to avoid Type II hard alpha defects. Aluminum being a low density material and highly volatile (due to high vapor pressure) when exposed to the hard vacuum environment and high power electron beams will either melt and dissolve or evaporate, depending on the chemistry. Therefore, it is important to clearly understand the difference between the two common mass transfer phenomena that may be active: melting and dissolution

(or dissolving). There are subtle distinctions between each of them and knowing these will provide clarity in determining the final state of a particle (of size $< \sim 100$ mm^3) when introduced into the melt pool.

Woods [24] in 1990 carried out a detailed study on melting and dissolving. He described melting as a thermal process while dissolution as a chemical process. Melting requires that the heat flux supplied from a hot liquid (solvent) to the solid/liquid interface be higher than the heat flux resulting from conduction in to the cold solid (solute) from the interface, eg: there is no phase change when pure ice at 0 °C is placed in contact with pure water at 0 °C. Whereas dissolution results when a mass flux occurs to maintain chemical thermodynamic equilibrium, eg: pure ice at -1 °C may dissolve if placed in contact with salty water at -1 °C. It has been observed that in most systems the solutal diffusivity is lower than that of the thermal diffusivity. The rate of melting is governed by heat transfer whereas the rate of dissolution (or dissolving) is governed by mass transfer.

Based on this definition, it can be inferred that when a piece of Al melt stock (~300 K) is introduced into a Ti melt (~1800 K); the solute melts with the latent heat of melting supplied by the hot Ti. Simultaneously, Al from near the interface disperses into the liquid due to significant solutal diffusivity leading to a process that can be defined as a combined melting-dissolution process.

2.3 Fluid Flow during Electron Beam Melting

Several researchers have studied the combined effects of thermal and compositional (solutal) buoyancy and Marangoni flow on the fluid flow during EBCHR using experimental and numerical modeling techniques. However, the study of these phenomena is not limited to the field of casting and solidification. Other fields where significant research has been reported on understanding the implication of these forces are: crystal growth [25], micro-gravity studies [26], welding [27], droplet studies [28] etc. In Electron Beam Melting (EBM), research has been carried out experimentally, theoretically and mathematically to understand the effects of buoyancy and Marangoni flow [23, 29]. This research focused on understanding the importance of these fluid flow forces during the dissolution of inclusions (or α-rich or β-rich particles). But, understanding the fluid flow during the dissolution of inclusions during EBM is

challenging. Researchers from French and Canadian universities: Bellot and colleagues, Ablitzer, Mitchell and several others have attempted to study the dissolution of materials in molten Ti which lead to hard-α Type I defects [30]. Very little work has been published on the dissolution of materials that lead to hard-α Type II defects. Therefore this section will consider the important research activities reported in applications related to EBM processing, such as surface melting, evaporation, inclusion removal, etc., in order to develop insight in to the physical phenomena that drive fluid flow and develop a preliminary understanding of the kinetics of dissolution of Type II inclusions in molten Ti.

2.3.1   Surface Melting

Few researchers have published research involving surface re-melting and the effects of alloying. Velde et al. [31] performed a theoretical analysis of alloying and surface re-melting during electron beam heating by re-melting AISI 1045 - chromium deposited specimen to understand Marangoni convection, heat transfer, specimen transport and free surface deformation. Similarly, Simon et al. [32] studied the physics occurring within the melt pool/ingot during the physical vapor deposition (PVD) process assisted by electron beam heating. He observed that the fluid flow within the melt pool was driven by natural convection and Marangoni flow due to surface tension gradients on the melt pool surface. It was found that the temperature drops off smoothly and slowly until it reaches the very edge of the melt pool after which the temperature drops off quite suddenly over a very small distance. The Marangoni stress due to the large temperature gradient was responsible for the large velocities near the pool's top edge and the sharp turn the fluid was taking.

Though this section deals primarily with presenting work conducted in the area of electron beam melting, important research conducted by Lei et al. [33] has been added as an exception because of the similarity of the work and the methodology with the objectives of the present study. Lei et al. [33] investigated the influence of alloying element vaporization and Marangoni flow during laser surface re-melting. Results showed that the heat loss due to vaporization and/or the mass flux of evaporation were adequately described by the Langmuir relation due to the presence of alloying elements like, Fe, Mn, Cr, Ni which strongly reduced the peak surface temperature. Based on this observation, it was reported that the pool surface temperature is strongly dependent on surface-tension gradient. When the surface-tension

gradient is less than zero, flow is directed outward from pool center resulting in a shallow and wide pool shape whereas when the surface tension gradient is greater than zero, flow is directed inward causing a relative narrow and deep profile. These limiting cases are shown schematically in **Figure 2.1**.
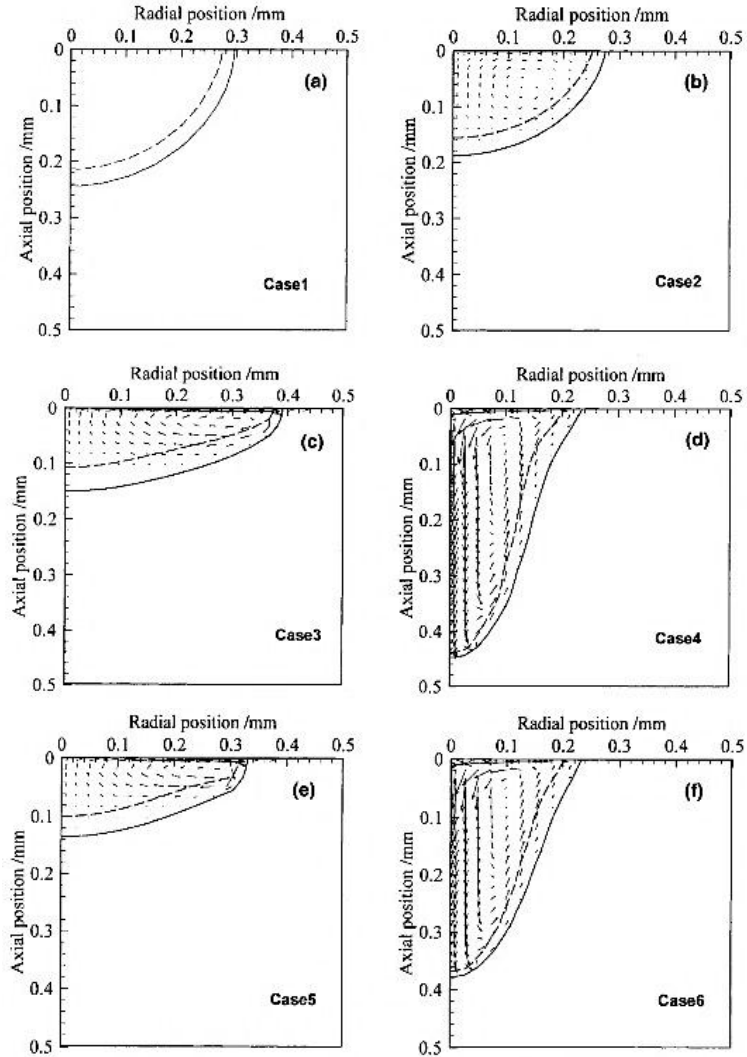
Figure 2.1 Molten pool size, profile and velocity fields for the cases: Case 1: $\partial\sigma/\partial T = 0$, $q_i = 0$; Case 2: $\partial\sigma/\partial T = 0$, $q_i \neq 0$; Case 3: $\partial\sigma/\partial T = -10^{-4}$, $q_i = 0$; Case 4: $\partial\sigma/\partial T = 10^{-4}$, $q_i = 0$; Case 5: $\partial\sigma/\partial T = -10^{-4}$, $q_i \neq 0$; Case 6: $\partial\sigma/\partial T = 10^{-4}$, $q_i \neq 0$. Solid line is solidus, and dashed line is liquidus [33]

Bergman et al. [34] used simulations to understand how Marangoni and buoyancy forces interact and influence the solid-liquid phase transformation process. They predicted the resultant shape and motion of the solid-liquid interface during the melting of a pure metal from an isothermal vertical wall. The results identified a complex interaction between the buoyancy forces in the melt and the Marangoni

16

effects at the melt surface. It was concluded that Marangoni forces have a significant impact on local melting behavior and the shape of the solid-liquid interface. Complex multicellular flow patterns were also observed which were related to local melting rates along the solid-liquid interface.

Goldschmied et al. [35] found that the Marangoni effect increased the transport of heat within the interior of a material during electron beam surface melting. The temperature distribution in the melt pool and heat affected zone were computed and verified with experimental results. It was found that the melt pool geometry is strongly dependent on the influence of Marangoni and buoyancy effects. It was also seen that the influence of the Marangoni effect is dependent on the melt depth: for shallow melt pools, the influence of Marangoni effect is significant.

2.3.2 Inclusion Removal

The presence of large thermal and concentration gradients in the melt pool can influence flow, and consequently the movement of an inclusion within the pool. Lee et al. [23] modeled and experimentally verified the dependence of Marangoni flow on temperature and surfactant (sulphur) concentration during electron beam melting of IN718 while studying inclusion removal. It was observed for the specific process condition used in the investigation that the flow is directed outward for a low concentration of S (6 ppm) with a maximum velocity of around 0.16 m/s whereas flow is inward for high sulphur concentration (20 ppm), moving in with a peak velocity of 0.19 m/s, refer to **Figure 2.2**. Al_2O_3 particles were used as surface trackers to determine the surface flow direction and velocities during the EBM process. It was concluded that Marangoni flow is the dominant driving force for fluid flow in electron beam melting.

An important study on inclusion entrainment and solute segregation in steel was carried out by Yin et al. [36]. Experiments were performed to understand the flow direction and velocity on the surface of a steel melt in the vicinity of the solid/liquid interface created using a He-Ne laser. They also studied the flow of inclusions, their removal and segregation. Three steel compositions were studied with decreasing concentrations of surfactants, sulphur and oxygen. At very low surfactant concentration (10 ppm), high velocity (~200 μm/s) solutal Marangoni was observed. For medium and high surfactant concentration (66 ppm and 105 ppm respectively), the increased surface tension gradient caused increased

17

flow velocity. During solidification, the solutal Marangoni flow was directed away from solid/liquid interface for all three surfactant concentrations and resulted in the transport of inclusions to the free surface. During heating and holding, thermally driven Marangoni flow combined with convective flow was dominant causing flow towards the solid/liquid interface. It was found that many inclusion particles were brought to the free surface by an upward flow generating a counter-clockwise motion in the right half of melt bath, shown in **Figure 2.3**.
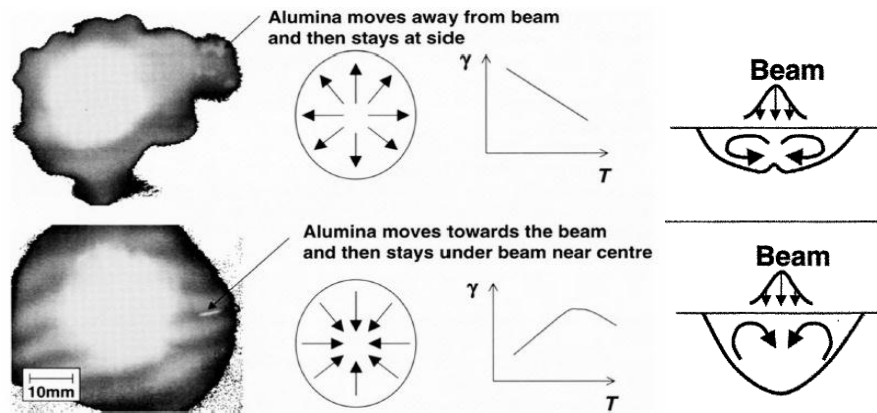
Figure 2.2 Effect of negative & positive gradient in surface tension on direction of Marangoni flow and the behavior of Al$_2$O$_3$ particles on surface of (a) low-S alloy and (b) high-S alloy [23]
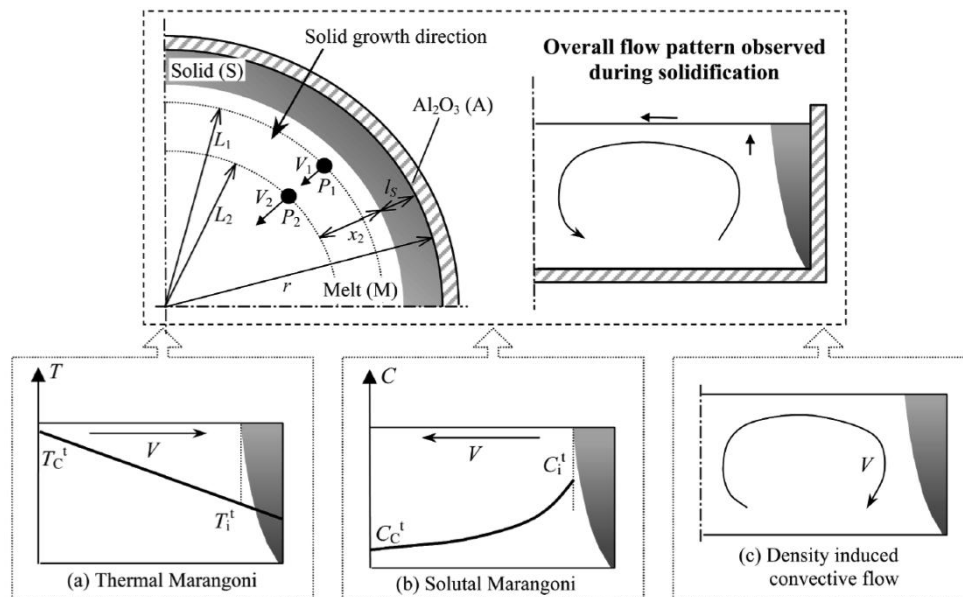
Figure 2.3 Possible flow patterns that can contribute to the observed overall converging surface flow during solidification of steel melt [36]

2.3.3 Evaporation

Electron beam evaporation is a technology for use in industries seeking to produce very thin coatings of high purity. In the process, an electron beam is used to melt the surface of a metal ingot to form a free surface and evaporate, leading to the generation of Marangoni and buoyancy flow on the free surface. Karcher et al. [37] confirmed the presence of strong turbulent convection on the free surface and the dominance of Marangoni flow (due to strong temperature gradients) over buoyancy during the electron beam (energy flux, 50 kW) evaporation of liquid iron. This experimental investigation was used to develop a 2-D computational model simulating the heat transfer in surface tension driven convection and evaporation of metals. The relation between the Nusselt number and Marangoni number was assessed for turbulent flow. A 10% difference in the experimental and numerical value of the Marangoni number was found due to the use of 2-D model and not a 3-D one.

A few studies related to EBM have been undertaken on the evaporation rate of Al in Ti-6Al-4V. Westerberg et al. [38] developed a steady state finite element model for an electron beam vaporization system. It was found that the flow in the metal pool is in the transition region between laminar and turbulent flow and that it is strongly affected by temperature induced buoyancy and capillary (Marangoni) forces. Another observation was that the liquid at the center moved towards cooler region (around sides) for cases where the beam was focused at the center, which was due to the formation of recirculating cell by thermally induced Marangoni and buoyancy forces.

Semiatin et al. [39] estimated the evaporation loss of aluminum during EBM of Ti-6Al-4V using finite domain and semi-infinite one-dimensional diffusion models that compute the solute concentration gradients and evaporation rate/mass loss at the melt surface using the Langmuir [40] equation. The accuracy of these models was validated using experimental data. It was concluded that both the model types showed similar predictions of concentration gradients and mass loss. It was found that in Ti-6Al-4V, the fractional mass loss of Ti is small compared to Al but because of the large concentration of Ti in the alloy, there is substantial Ti weight loss. The effects of melting parameters and material properties on mass loss were investigated and a sensitivity analysis was used to evaluate the effect of uncertainty in the value of diffusivity in the models.

19

Along similar lines, Powell et al. [41] used the Langmuir equation, based on interface reaction controlled kinetics, to predict the loss of Al in Ti-6Al-4V during EBM. The measured and predicted evaporation rates showed good agreement but a physically unrealistic value of the activity coefficient for Al was required. However, the rate controlling factor of solute diffusion in the melt was not considered. Ivanchenko et al. [42] and Akhonin et al. [43] later improved upon the work of Powell et al. [41]. Ivanchenko et al. [42] established the activity coefficients for the Langmuir equation and developed a semi-infinite diffusion model to show the kinetics of evaporation during EBM of Ti-6Al-4V. Akhonin et al. [43] developed a specialized approach to analyze industrial melting operations that considers evaporation kinetics, boundary layer diffusion, and the mass balance in the model.

2.3.4 Dissolution

Electron beam melting of Ti has a tendency to dissolve small inclusions of nearly any composition but not large inclusions, which act as a threat to the mechanical properties of the final metal. The EBCHR process has been successful in refining Ti alloys and removing hard-α inclusions by dissolution, floating and settling. The high density and hard-α inclusions are trapped in the refining hearth but would otherwise sink to the bottom of the molten pool during casting.

Three factors which decide the probability of survival of inclusions in the hearth are: size, density and residence time in hearth. Size is a significant factor affecting time required for complete dissolution, while size and density determines the buoyancy force and drag forces, which in turn determines the falling or rising velocity. The inclusion will not enter the final product if the residence time is greater than the dissolution or floating time. [29]

Several experimental investigations [44] have been carried out to understand the complex mechanisms controlling the dissolution of hard-alpha particles and the diffusion of nitrogen into the liquid. Most quantify the dissolution rate of nitride particles in Ti but without consideration particle size, geometry and/or the initial concentration of alloying elements. Jarret [45] related the dissolution rate of a hard-α particle with the trajectory of flow in the cold hearth. Considering the complexity of the experiments, a simplified representation of metal flow and dissolution were assumed to apply. In follow-

on work, Jarret et al. [46] derived the diffusion coefficient for nitrogen in Ti using Fick's second law but did not consider the formation of phases during dissolution.

Ablitzer [47] simulated the trajectory and dissolution rate of hard-α Type I inclusions in a melt. He developed an equation to describe the trajectory of an inclusion, given by:

$$\rho_p V_p \frac{\overrightarrow{du}}{dt} = \vec{P} + \vec{A} + \vec{F} \tag{2.3}$$

where ρ_p is the density of the inclusion particle, V_p is its volume, u is its relative velocity with respect to the fluid, $\vec{P}$ is its weight, $\vec{A}$ is the Archimedes thrust (buoyant force equal to the weight of the displaced fluid) and $\vec{F}$ is the resultant of the force of the fluid on the inclusion. A dissolution model of hard-α Type I inclusions was developed to calculate the dimensions of α and β phase according to the equilibrium phase diagram. Coupled with the trajectory model, this model enables tracking the flow direction, velocity and the rate of dissolution of an inclusion of known diameter. It was found that a 500 μm hard-α Type I inclusion was affected by the re-circulatory movements of the metal, while a 1000 μm particle was trapped in the solidification front after 22 s, before it dissolved completely.

Powell [29] characterized the dissolution of pure titanium nitride in liquid Ti. The dissolution was found to be 0.16 mm/min based on the results shown in **Figure 2.4**.
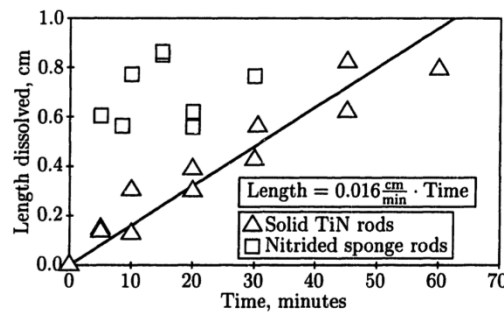
Figure 2.4 Titanium nitride dissolution rate [29]

It was found that the dissolution rate has an approximately linear relationship with time of dissolution and the length of pure nitride (solid TiN rods) dissolved. The results of nitride sponge with 15% nitride did

21

not show good co-relation because of the variation in porosity and nitride fraction in the nitride particles. It was determined that nitride particles should have a density close to that of liquid Ti so that they neither rise nor sink to the bottom of the refining hearth.

In 1996, Bellot [30] performed an experimental and theoretical study to understand the dissolution of hard-α inclusions in liquid Ti by dissolving synthetic hard-α particles (6 wt. % nitrogen) and nitride sponge (15 wt. % nitrogen). It was found that the dissolution process was controlled by the diffusion of nitrogen through an external layer of beta phase. A mathematical model was developed that included dissolution kinetics for dense, solid solution of Ti and nitrogen in alpha or beta phase immersed in pure liquid titanium, taking into account the bath temperature and liquid flow velocity around the particle.

Bellot et al. [48],[20] combined models of an EBCHR process and hard-α dissolution [49],[50] to develop a particle dissolution model that determines the trajectory of nitrogen-enriched dense hard-α TiN particles with binary composition, i.e. α and β intermediate phases; dissolving in a bath of liquid titanium. The model was capable of predicting the evolution of the particle in terms of position, size and composition during melting in the cold hearth. The composition of the two phases present in the particles, together with solute distribution in the particles and in the surrounding liquid was calculated. It was concluded that particles whose relative density in relation to the liquid was ±3%, flow with the fluid in the hearth while high density particles sink and low density particles rise.

Recently a relevant study has been published by Ghazal et al. [51] on the dissolution of high density inclusions (W, Mb) in CP-Ti (Commercial Pure) and Ti-6Al-4V bath in an electron beam furnace, a video-graphic image of which is shown in **Figure 2.5 (a)**. During this study cylindrical rods of 4 mm diameter and 30 mm length were dipped in molten Ti for a limited time. The dissolution rate was calculated by measuring the dimensions of the rod before and after the dissolution experiment, shown in **Figure 2.5 (b)**. It was found that the dissolution kinetics is strongly dependent on the temperature and velocity of the liquid metal (Ti bath). It was also found that the dissolution of inclusion materials studied was higher in CP-Ti than in Ti-6Al-4V. The results obtained from experimental and computational work showed good agreement.
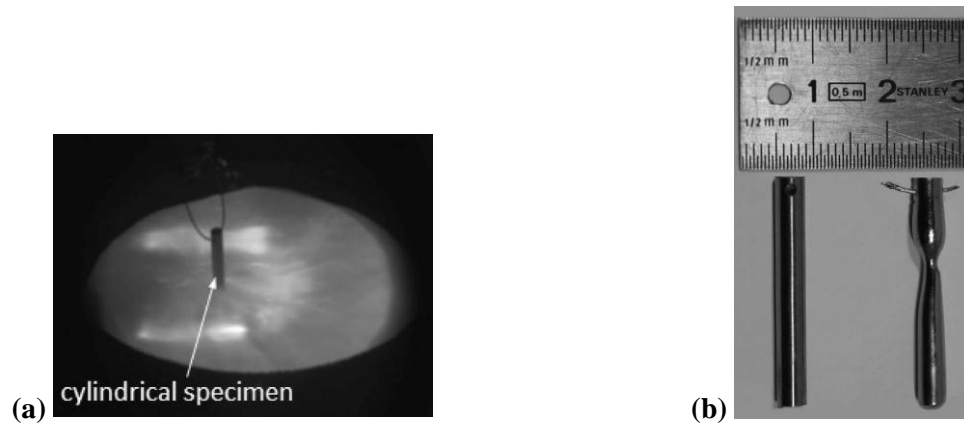
Figure 2.5 (a) Video image of the liquid pool surface during an experiment, showing the U-shaped scanning pattern of the electron beam; (b) Tungsten cylinder before (left) and after (right) a dissolution experiment [51]

2.3.5   Welding

During welding of steel, the shape of the weld pool is the deciding factor for weldability. Due to the strong differences in temperature between the center and sides of the pool, Marangoni flow occurs on the pool surface.

As in EBM, the center of the melt is heated while the melt at the sides coexist with the solid. The temperature variation of surface tension in steel is dependent on S and O contamination. **Figure 2.6** shows that in a reducing atmosphere, the temperature coefficient is negative and therefore Marangoni flow is outward from the center of the pool and the pool is shallow. If the surface tension has a positive temperature coefficient due to contamination above critical levels (around 50 ppm), the flow is directed inward from sides to the center; leading to deeper pool formation and better weldability. In addition to Marangoni, there are several other fluid flow phenomena occurring within the weld pool as shown in **Figure 2.7**.
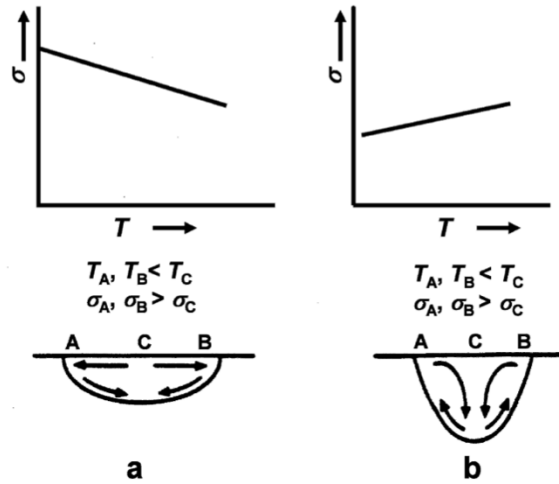
Figure 2.6 Relationship between temperature coefficients of molten steel and weld pool shape [52]
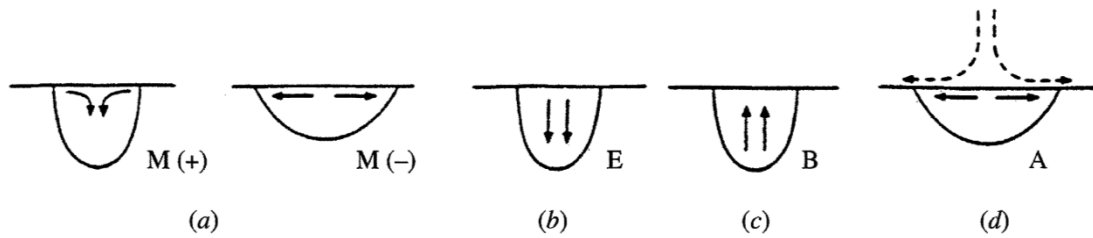
Figure 2.7 (a) Thermocapillary (Marangoni) forces M(+) or M(-); (b) Electromagnetic (Lorentz) forces E, resulting from interaction of current; (c) Buoyancy forces B, resulting from density differences caused by temperature gradients; (d) Aerodynamic drag forces A, caused by passage of plasma over surface [27]

Mills et al. [27] studied the directional behavior of the Marangoni flow during electron beam welding based on the concentration of sulphur (S) in steel. It was known that increased sulphur concentration in steel, decreases surface tension. Based on this data, Mills et al. found that Marangoni flow generated due to temperature and composition differences were directed from a region of high S (low surface tension) to low S (high surface tension). They concluded that the direction of Marangoni flow is strongly influenced by the concentration of sulphur in steel.

Limmaneevichitr et al. [53] performed a detailed study to understand the effect of beam power on Marangoni convection and weld pool shape using a laser beam. It was determined that increasing the beam power increases Marangoni convection as well as the pool size, characteristic length and velocity. Since heat is carried outward to the pool edge by the strong outward surface flow, the bottom of the pool becomes wide and flat. Also, it was found that decreasing the beam diameter increases Marangoni

convection (refer **Figure 2.8**) and the characteristic velocity. In this case the returning flow penetrates the pool bottom, making the bottom of the pool convex. It was confirmed that in both the cases the Marangoni convection dominated the gravity-induced buoyancy.
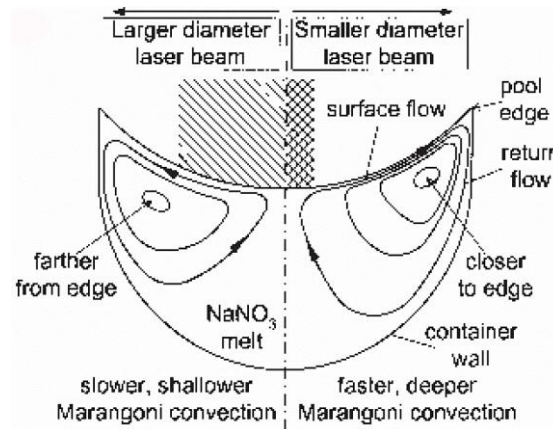
Figure 2.8 Effect of beam diameter on convection pattern under a constant power [53]

In summary, a number of experimental and modeling investigations have been undertaken to investigate the transport phenomena occurring within the EBCHR process. Several studies have been carried out to mathematically model the experimental results and have been shown to make realistic predictions. However, because of the significant challenges associated with conducting experiments on liquid Ti within the EBCHR process, there is little published work that is directly relevant to the dissolution of hard α-particles Type II. Understanding the transport of heat, mass and momentum during the dissolution of α-phase stabilizers (like Al) in a Ti melt is an area which requires further study.

2.4 Water Modeling

In practice, it is difficult to characterize the flow of metal (both on and below the surface) during the dissolution of a solid material i.e. Al in a high temperature Ti melt. This makes it difficult to validate numerical models of dissolution directly. Water analogue models that simulate the flow of liquid metal using water provide an efficient way to validate numerical models and observe physical phenomena. Since, the Navier-Stokes equation can be solved to determine the motion of fluids based on their material

25

properties such as density and viscosity, initial conditions and boundary conditions, a model validated with data from a water analogue model can be applied to accurately simulate the motion of other fluids such as liquid metals under similar conditions. The water analogue technique has been successfully implemented, tested and validated in various studies related to metal flow in die casting processes [54, 55], continuous casting [56], [57], strip casting [58, 59], entrapment phenomena [60] etc.

Incropera et al. [61-63] and several others [64] used water based (NH_4Cl-H_2O) analogue models with various domain sizes and heat transfer conditions to study fundamental aspects of binary solidification. The phenomena studied includes the relationship between channel flow occuring during early stages of solidification and the formation of A-segregates in the final casting [61, 65], the importance of mixed and thermo/diffusocapillary convection [66], the erosion of a double-diffusive interface in the melt [64, 67] and the influence of convection on the directional dendritic solidification [68]. Theoretical and experimental studies were also performed by Incropera et al. to determine the effect of thermo/solutal natural convection on the solidification of a $NaCO_3$-H_2O solution in a horizontal, cylindrical cavity [67].

Another interesting analysis was reported by Ecker et al. [69] where the fluid flow during the solidification of monotectic alloys was visualized. The primary sources of fluid motion were buoyancy and thermocapillary (Marangoni) forces. The aim was to understand the nature of fluid flow in the melt, its relation to alloy composition, and its influence on mass transport. Since the work required the use of a transparent alloy system, succinonitrile-water (SCN-W) and succinonitrile-ethanol (SCN-E) were selected to allow useful conclusions to be made on the effect of buoyancy and thermocapillary forces. The observations were made using holographic and shadowgraph techniques (qualitative measurements), and two-wavelength holography (quantitative measurement).

Dharwadkar et al. [70] developed an ice-water model to study the effects of various parameters governing the formation of skin and blowholes for comparison to steel ingots. By freezing water with high levels of dissolved CO_2 in a plexiglass cell it was possible to simulate a small horizontal element of an ingot. Various governing parameters were calculated and an attempt was made to explain the formation of the blowhole-free depth on the basis of a mathematical model comprising diffusional and

26

convective mass transfer. Similarly, Mahmoudi et al. [71] developed a mathematical model of the flow pattern in the liquid pool, to determine how molten copper is distributed through the nozzles during continuous strip casting. To verify the accuracy of the model, its predictions were compared with a transparent plastic water model. The analogue model correctly predicted the formation of the recirculating zone within the upper part as seen in the real system.

A more experimental approach was taken by Aubeterre et al. [72] to understand Marangoni effects induced by heat and mass transfer. The Marangoni number was calculated to analyze each effect. Four aliphatic alcohols were studied: methanol, ethanol, n-propanol, n-butanol. It was found that the Marangoni number decreases with increasing carbon number atoms because of the change in the surface tension and diffusivity as heat and mass transfer operations occur. It was also observed that with an increase in pressure, the diffusion characteristics of hydrocarbons decreased, leading to an increase in the Marangoni number.
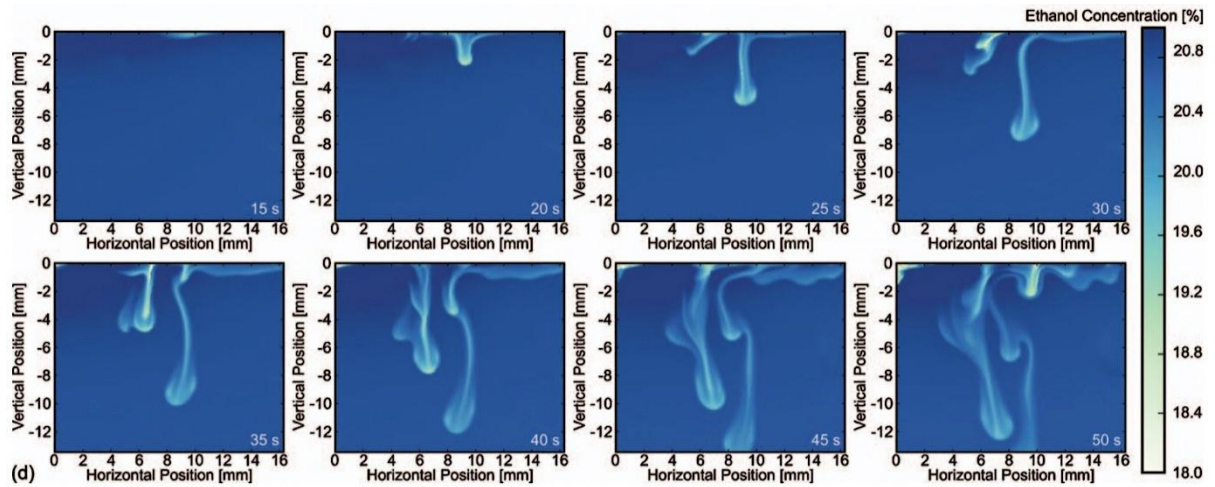
Figure 2.9 Ethanol concentration map at different moments after starting the evaporation

Along similar lines, Tatsis et al. [73] studied the effect of surfactants on Marangoni convection in the Isobutanol/Water system. The presence of surfactants increased the Marangoni convection and enhanced the mass transfer fluxes. The interface and the concentration profiles were characterized with Mach-Zehnder interferometry. Dehaeck et al. [74] studied the evaporation of water-ethanol mixtures

experimentally and interpreted the change in the ethanol concentration with time in the mixture using Mach–Zehnder interferometry, shown in **Figure 2.9**. These images were produced using a demodulation technique based on a Fourier transformation to compute the change in the refractive index field for each fringe pattern.

In summary, water analogue modeling techniques have been used to study the fundamental physical phenomena and validate numerical simulations of liquid metal processing. By using these techniques, it is possible to overcome the difficulties faced in visualizing the flow of hot molten metal during casting processes. The water analogue modeling technique has been successful employed to highlight the flow features in several casting problems through the capture of "clean" experimental images related to fluid motion and data related to transport of heat and mass. It can predict the shape and movement of solid, liquid or fluid in motion with acceptable accuracy.

3 Scope and Objective

3.1 Scope of this Research

In order to produce high quality Ti-6Al-4V ingots, Ti producers must understand the process of dissolution and homogenization of alloying elements. With regards to Al in the EBCHR process, Al-rich material may enter the melt in the refining hearth or casting process through ballistic transfer from the melting hearth. If this material is not completely dissolved and mixed before solidification Al rich regions may occur which result in hard alpha Type II defects that significantly reduces material performance.

This project is part of a larger research programme aimed at developing a comprehensive numerical thermo-fluid-compositional model to study the heat transfer, fluid flow and mass transport involved during the dissolution of Al-rich material in Ti-6Al-4V at an industrial scale. One of the goals of the programme is to simulate the dissolution process of ballistic-transfer material from its point of entry into the melt until full solidification of the casting. Understanding this dissolution process will allow Ti producers to optimize their process and to reduce the occurrence of Al rich defects. Understanding the role and the influence of the driving forces for dissolution and fluid flow is critical to the success of the project. Past research on this topic concluded that in addition to temperature, composition has a great influence on both buoyancy and Marangoni flow. Hence, understanding the role of the four forces: thermal and compositional buoyancy, thermal and compositional Marangoni is critical.

Electron beam melting of liquid titanium and understanding the process of dissolution of Al-rich material in molten Ti is a complex process to study. The temperatures and vacuum environment as well as the reactive nature of liquid Ti make performing quantitative experiments at either the industrial or lab scale extremely difficult and frequently impossible. Hence, the current work has focused on the development of a physical analogue model that incorporates the significant physical phenomena occurring in the EBCHR process. The physical model will provide data suitable for validating a computational model (which will also be developed to meet the overall aim of this research program).

3.2 Objectives of this Research

The objectives of this research are:

1. To gain fundamental understanding of the various factors impacting the dissolution of a lower melting point solid in a liquid of different composition. This is crucial to ensure that the model both includes the relevant physical phenomena and is capable of accurately describing the dissolution and homogenization (mixing) process.

2. To develop a physical water-ethanol analogue model to replicate some aspects of the dissolution process for Al-rich material entering the melt during EBCHR. This analogue system should help investigate factors that are critical to the understanding of the dissolution kinetics. Conducting experiments with the ethanol-water system simplifies the adverse and complex conditions present during the electron beam melting of Ti, thereby allowing better quantification of the heat, mass and momentum transport mechanisms.

3. To develop and verify a mathematical model of the dissolution process, considering the fluid flow that develops due to thermal and compositional buoyancy and Marangoni forces. Once validated with the results of the ethanol-water analogue experiments, this computational model can be applied to the Al-Ti system.

4 Experimental Methodology

The dissolution process for an alloying element in a molten Ti pool in an electron beam furnace under high vacuum involves transport of heat, mass and momentum. Understanding phenomena such as buoyancy forces, Marangoni forces and Darcy related flow that influence these transport process is difficult due to following challenges:

a) It is difficult to visualize and quantify the fluid flow within a molten pool of Ti prior to and during a dissolution event because the liquid is opaque. Hence, directional analysis of fluid flow and velocity measurements in the bulk liquid are not feasible.

b) Ti melts at a high temperature (1680 °C) which makes it difficult to source appropriate materials and to design robust experiment equipment.

c) Liquid Ti is highly reactive demonstrating very high affinity for oxygen which precludes the use of refractories for the containment of liquid Ti in industrial operations. Ti must be melted under high vacuum (10^{-5} Pa) or in an inert gas atmosphere and is often contained in an autogenous lining.

Thus to mitigate these challenges, a physical analogue model was sought that is capable of replicating many of the physical characteristics present in the Ti system like temperature and compositionally dependent buoyancy and surface tension driven flow. To select a suitable analogue system, the key characteristics of the Al-Ti metal system were carefully reviewed. It was determined that the analogue model needed to possess the following characteristics:

a) In the Al-Ti system, the solute (the solid material undergoing dissolution) is Al and the solvent (the molten pool/bath) is Ti-6Al-4V. Al has a low melting point (660 °C), low density (2.70 g/cm^3) and a low surface tension (1.07 J/m^2) when compared with Ti (1670 °C, 4.12 g/cm^3, 1.52 J/m^2), [75-79]. The solute and solvent in the analogue model must exhibit comparable differences in material properties to the Al-Ti system.

b) The solvent must be a transparent liquid to allow flow visualization and quantification during dissolution.

c) Material properties like density, surface tension coefficient, viscosity and thermal conductivity, as a function of temperature above and below the melting point must be available for both the solvent and solute.

d) Al is an alloying element in Ti-6Al-4V and is completely soluble. Thus, the solute should be completely miscible and soluble in the chosen solvent.

Water often referred to as the universal solvent is miscible with many liquids over a range of compositions. Also, water is transparent and its physical properties are readily available over a wide range of temperatures, both above and below its freezing point. Therefore, it was chosen as the solvent for the analogue model.

Many liquids were considered for use as solutes in this study. **Table 4.1** shows a list of the liquids considered and their relevant properties.

Table 4.1 Physical properties of various liquids

Name	Melting Point, °C	Density at ~298 K, g/ml	Solubility in 100g of water	Viscosity, 10^{-3} Pa·s	Surface tension at ~298 K, 10^{-3}, J/m^2	Comments (considered as a solute in water)
Water	0.0	0.997	-	0.890	71.98	-
Acetone	- 94.7	0.785	miscible	0.304	22.68	Suitable
n-Butanol, Butyl alcohol	- 88.6	0.806	8.3	2.593	24.30	Soluble not miscible
Diethyl ether	- 116.3	0.708	7.5	0.224	16.50	Similar to acetone
Diglyme	- 64.0	0.937	miscible	1.880	-	High density
Dimethylformamide, DMF	- 60.4	0.945	miscible	0.796	36.30	High density
Ethanol	- 114.1	0.785	miscible	1.078	22.00	Suitable
Ethyl methyl ketone	- 86.7	0.797	29.4	0.400	-	Less data available
Isobutanol	- 108.0	0.800	10.0	6.680	23.00	Very high viscosity
Isopropanol, 2-propanol	- 88.0	0.781	miscible	2.073	18.30	Suitable
Methanol	- 97.7	0.786	miscible	0.545	22.10	Suitable
Tetrahydrofurane, THF	- 108.5	0.884	miscible	0.461	26.40	High density
Triethylamine	- 114.7	0.723	13.3	0.341	20.10	Not miscible

In **Table 4.1**, only four liquids: Acetone, Ethanol, Isopropanol and Methanol were found to be suitable for use as a solute in a water-based physical analogue model. Among the four, ethanol was determined to be the best because it provides the maximum difference in melting point between itself and water. Additionally, it is cheap, readily available, safe and easy to use and its material properties are well known. **Table 4.2** compares the key properties of both the Al-Ti metal system and the ethanol-water analogue system.

Table 4.2 Properties of Al-Ti and ethanol-water systems [75-79]

Name	Al (Solid Solute)	Ethanol (Solid Solute)	Ti-6Al-4V (Liquid Solvent)	Water (Liquid Solvent)
Melting point (°C)	660	-114	1670	0
Density (g/cm^3 or g/ml)	2.70	0.79	4.12	0.99
Surface Tension (J/m^2)	1.07	0.02	1.52	0.07

4.1 Experimental Setup

A cylindrical cell (beaker) was selected to conduct the experiments because it encourages axisymmetric conditions that are convenient to model. The setup consists of a transparent cylindrical glass cell: 100 mm in diameter and 150 mm in height. The glass cell contained heated water (the solvent) into which a frozen solid solute was placed. T-type thermocouples (details in section 4.3.1) were used to measure the temperature at two different locations: one within solute center, T1, and one near to the edge of the cell (in the solvent region), T2, as shown in **Figure 4.1.**

Experiments were conducted with two different geometric configurations as shown in **Figure 4.2**. In **Figure 4.2 (a)**, the solid solute is completely immersed to the center of the solvent bath to eliminate Marangoni forces and to produce buoyancy forces only. In **Figure 4.2 (b)**, the solid solute is partially immersed into the solvent resulting in Marangoni forces at the surface along with buoyancy forces.
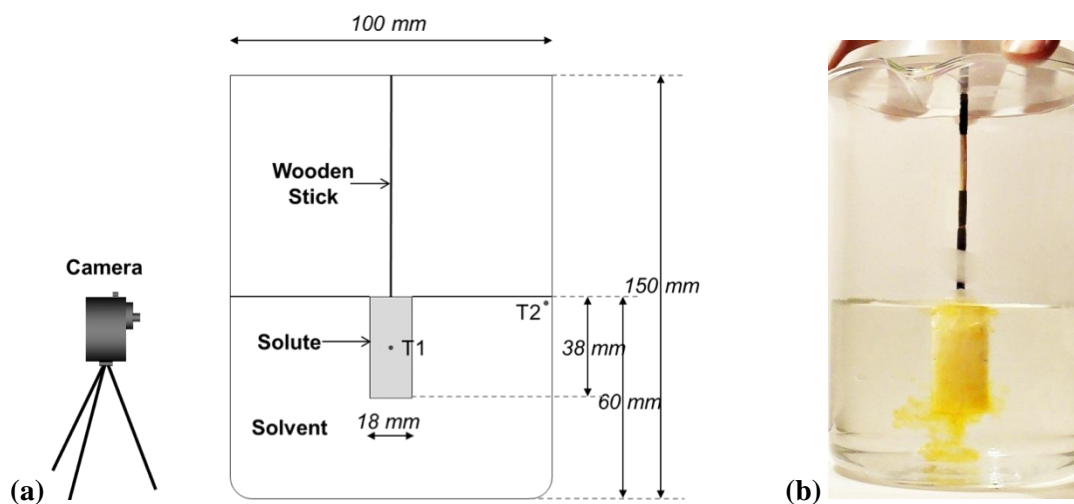
Figure 4.1 Experimental setup: (a) Schematic representation of the cylindrical setup; (b) Preview of the cylindrical setup
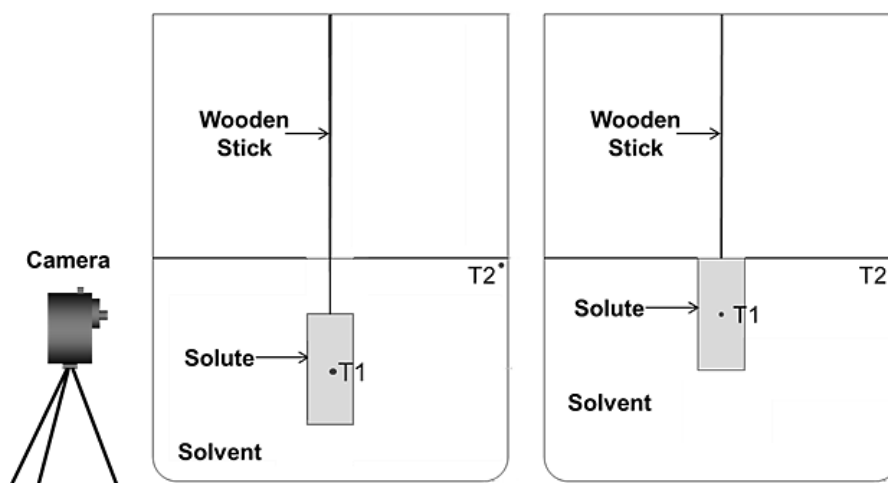
(a) Marangoni force on surface – Absent;   (b) Marangoni force on surface – Present

Figure 4.2 Two geometric configurations of the cylindrical setup used

A hollow ceramic rod, 4 mm in diameter and 150 mm in length, was used in studies where ice was used as solid solute. The hollow ceramic rod allowed the T-type thermocouple to pass through to the desired height of 19 mm (or mid-height) from the top surface of the solute which was 38 mm deep. A thin wooden stick, 3.5 mm in diameter and 150 mm in length was used in studies where solidified ethanol was used as the solute. Wood was used in these tests because it provided greater adhesion to the solid ethanol

solute compared to the hollow ceramic rods. A number of tests were performed to test the effects of the solute support material (wood, ceramic rod, copper rod, PFA insulted thermocouple) on the melting time or melting characteristics. No significant differences were observed in the overall dissolution time and the flow behavior.

Since, both the solute and solvent materials are transparent; dyes were used to mark the solute. An organic soluble dye, Aniline blue (spirit soluble, insoluble in water), was used to distinguish ethanol from water while a water soluble dye, Methyl orange (water soluble, insoluble in organic liquid), was used for cases when water was both solute and solvent. A data acquisition system was used to record the temperature data from the T-type thermocouples. A Measurement Computing USB-TEMP device was monitored with TracerDAQ, real-time measurement display/recording software. Measurements were taken at a frequency of 2 Hz. A camera (digital point-and-shoot type, DSC-H55 from SONY, video image size 1280×720 recording at 30 fps) was used to record the dissolution event of the solid solute melting into the liquid solvent. The video was subsequently processed to interpret the solid/liquid interface, velocity and compositional profiles using video-image editing software (ImageJ and VirtualDub).

Generation of frozen solute: A large diameter shallow glass beaker, 200 mm in diameter and 100 mm in depth, was used to contain liquid nitrogen. Liquid nitrogen was used as a medium to solidify both ethanol and water to produce solidified ethanol and ice solute samples for the respective experiments. To produce solid solute of consistent diameter and height, a graduated cylinder, with an inner diameter of 20 mm and a height of 200 mm, was used as the mould for freezing the samples in liquid nitrogen. An apparatus stand was used to grip the glass mould in the liquid nitrogen bath. To remove the solidified solute from the glass mould, another glass beaker, 100 mm in diameter and 150 mm in depth, was filled with hot water maintained at ~333 K. Additionally, a heater was used to increase the temperature of the water solvent to desired levels. A laboratory-grade thermometer with a scale between 0 °C (273 K) and 110 °C (383 K) was used to measure the water temperature when heating.

Safety gloves, chemical protection coat and face shield were required personal protection equipment during the transfer of liquid nitrogen into the large diameter beaker and while performing the experiments with dye mixed absolute ethanol.

4.2 Procedure

The experimental methodology followed prior to each test was: 15 ml of solute in liquid form was poured into the graduated cylinder mould. A hollow ceramic rod or wooden stick, with a T-type thermocouple (T1) mounted on it, was inserted into the mould to the desired depth into the liquid. A second thermocouple (T2) was mounted, using adhesive tape, on the inside wall of the cylindrical beaker to record the change in solvent temperature during the experiment. The thermocouples and the data acquisition system were calibrated and tested for errors. The graduated cylinder mould - thermocouple setup was then placed in a large diameter shallow beaker/vessel. Using the apparatus stand, the liquid solute filled mould was gripped and adjustments were made to ensure that the stick/rod (with thermocouple) was positioned at the center of the mould. Liquid nitrogen was then poured into the vessel to solidify the solute liquid. The data acquisition system was activated to record the temperature at locations T1 and T2.

The solute temperature was allowed to equilibrate (~83 K) for 5 minutes. The mould with the solidified solute sample was then dipped in to a beaker filled with warm water (~333 K) to enable the removal of the sample from the mould. Once removed, the top surface of the cold solute was trimmed using a knife to ensure a straight profile across the top eliminating the concave or convex surface that develops due to capillary forces and/or shrinkage or expansion during solidification. The shaped solute was then dipped in liquid nitrogen again to reduce the temperature to at least 10 K below its melting point. In the meantime, the cylindrical cell was filled with warm distilled water at a temperature of 318 K, up to a height of 60 mm.

Testing: The solidified and trimmed solute samples with temperatures of ~263 K for ice and > ~80 K for solid ethanol, were dipped into the water solvent maintained at 318 K, making sure that the stick/rod (with thermocouple) was aligned vertically and positioned at the center of the beaker. The stick/rod was supported using a circular lid that extended across the opening of the glass beaker cell. The data acquisition system, activated earlier during the preparation phase, continued to monitor temperatures. The dissolution of the solid solute in the liquid solvent was recorded using the video-camera.

Interestingly, the dipping temperature of the cold solid solute and the temperature of the water solvent govern the initial dissolution behavior along with the fluid flow at the interface. It was observed that when the temperature of the solvent bath was less than or equal to ~293 K, the solvent had a tendency to freeze around the cold solute sample, restricting the momentum and mass transport across the interface till the boundary breaks (melts). Hence, the water solvent temperature was raised to 318 K at which no freezing of the solvent was observed. This temperature was set after repeating the experiment with a variety of different solvent temperatures. The reason behind the occurrence of such phenomena will be discussed later in Chapter 6, Results and Discussion.

4.3   Data Acquisition and Processing

Quantitative measurements have been made on the physical analogue experiments to provide insight into the phenomena that are active and to provide data to validate a mathematical model of the experiment. Four quantitative measurements based on velocity, composition, temperature and dissolution profile of the solute were sought. Unfortunately, there were significant challenges experienced while attempting velocity profile and compositional mapping measurements.

Attempts were made to quantify the velocity of particles placed on the liquid surface and in close proximity to the cold solute to measure the Marangoni velocity. This method proved to be unsuitable as the particles (same density as water in the solute or solvent) hindered the flow and the dissolution process. Similarly, quantitative mapping of the variation of the composition of solute in the solvent was attempted. A grey scale plot (8-bit) of one of the video frames was obtained for which the quantitative grey intensity value was extracted vertically down along the center. The grey intensity values obtained along y-distance (vertically) from the image were then compared with the grey intensity values for known ethanol concentrations. In this manner, the ethanol concentrations corresponding to grey-scale intensity were obtained. This measurement was found to be very sensitive to lighting and maintaining a consistent light intensity throughout the depth of the solvent could not be achieved.

Therefore in this study, two types of measurements were performed based on procedures developed after conducting numerous repeatability evaluations. The results of these evaluation tests will be discussed in the later sections: Chapter 6, section 6.1 and will detail:

a) Measuring the evolution of temperature in both the solute and solvent.

b) Measuring the profile of the solid-liquid interface with time at specific locations.

4.3.1   Temperature

In this study, the T-type thermocouples used were 30 AWG in diameter, 36 inches in length and PFA (partially fluorinated polymer) insulated. The temperature range over which T-type thermocouples are functional is 73.15 K to 623.15 K. T-type thermocouples were used for this study because the experiments involved ethanol at temperatures below its freezing/melting point (close to 77 K) using liquid nitrogen and T-type thermocouple are the only type of thermocouples which are operational at such low temperatures. The temperature data was recorded from each thermocouple using the data acquisition system at a frequency of 2 Hz.

Initially, three thermocouples were embedded along the centerline of the solute (axially) at three different heights: top (~2 mm below the top surface of the solute), center (~19 mm below the top surface of the solute) and bottom (~2 mm above the bottom surface of the solute). During trial runs with this configuration, it was observed that the maximum amount of flow occurred from either the top surface during the dissolution of ethanol solute in water solvent or from the bottom surface during the dissolution of ice solute in water solvent. Under these conditions, the flow of low temperature liquid to the top or bottom disturbed the temperature response. Based on these observations, it was decided to use only one thermocouple located at the center of the solute, both diametrically and axially. Hence, T1 (solute thermocouple) was located 19 mm below the top surface of the solute on the centerline.

Trial runs were also performed to determine if more than one thermocouple was necessary within the water solvent. It was observed that there was negligible difference (on the order of 2 °C) in the temperature readings from three thermocouples located at different heights in the solvent. Therefore, it was decided to use only one thermocouple T2 located 3 mm. below the top surface of the water.

4.3.2 Solid-Liquid interface

Video of each experiment was recorded at 30 frames per second with an image resolution of 1280 by 720 pixels. The recordings were post processed using VirtualDub, a video capture/processing utility software. Prior to starting each experiment, an object of known length and width was dipped into the beaker at the same location where the solid solute would be placed. A short video sequence was recorded to enable accurate scaling to limit the effects of parallax and refraction of the video images of the experiment.

a) The lens of the camera was centered vertically with the center of the solute; and

b) The solute was located diametrically at the center of the beaker to avoid the distortion caused by the curvature of the glass beaker.

The video-images were edited in VirtualDub, by over-laying a grid over the whole image (size: 15 unit) to facilitate scaling and measurement. Scaling factors were determined based on the number of grid squares overlapping the object of known length. Using this data, the length and height of a single grid box was calculated. The measurement was used as the basis for calculating the change in the diameter and height of the solute sample during each experiment, as shown in **Figure 4.3**. The diameter and height of the solute were determined in this manner every 5 seconds in each experiment.
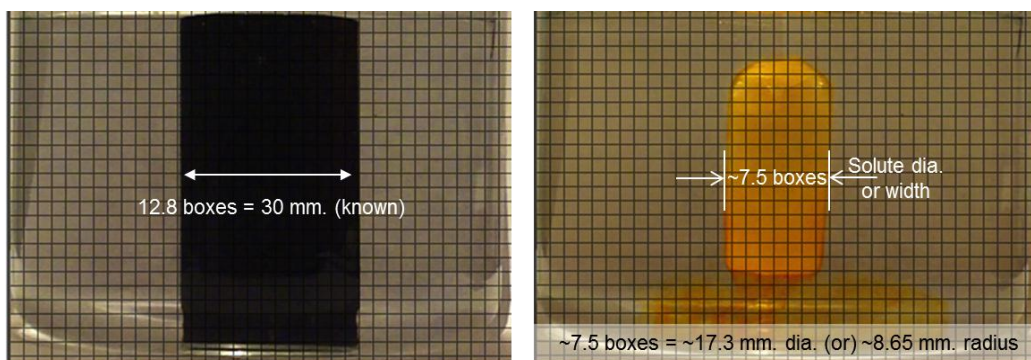
Figure 4.3 Dimensional scaling of the solid solute

5 Mathematical Model Development

To aid in understanding the dissolution process, a thermal-compositional-fluid flow model of the water-ethanol physical model has been developed. The model has been used to study two specific experimental cases: the dissolution of ice in water and solidified ethanol in water. These cases were selected because they enable the factors influencing fluid flow during the dissolution process of a solid solute in a liquid solvent to be evaluated:

a) **Ice in water:** The solute and solvent have the same composition but different initial temperatures. Thus, isolating fluid flow to thermally driven processes.

b) **Ethanol in water:** The solute and solvent have different compositions and different initial temperatures. In this case, both thermal and compositional phenomena will affect the fluid flow conditions

The ultimate goal of developing a dissolution model in this work is to assess the dissolution process of Al-rich material in a Ti-6Al-4V melt. As a first step in model development, the water-ethanol system will be studied for the reasons described in Chapter 4. The ethanol/water model will provide useful information regarding the influence of each of the critical process parameters, such as viscosity, specific heat, liquid fraction and conductivity, on the overall dissolution behavior. The model has been developed using the commercial CFD package, ANSYS CFX version 12.0. The model has been developed in collaboration with Jun Ou, a Ph.D student in the department of Materials Engineering at University of British Columbia. The development process employed an incremental approach, where model features and complexity were added sequentially, in order to produce a model that accurately represents the physics of the problem. This section details the development of the model including assumptions, geometry and mesh details, formulation, material properties and boundary conditions. It also discusses methods to describe latent heat absorption as a material property, flow dampening (Darcy resistance) as a part of the model formulation and Marangoni force as a boundary condition.

5.1 Model Physics

The model developed is a multi-component dissolution model, consisting of two different components in a domain, one being the solute (solid region) and the other being the solvent (liquid region). The solid and the liquid state of the region are decided based on the liquid fraction data assigned for the respective component, which is in turn a function of temperature. The solute is a low temperature component that absorbs heat from the liquid solvent to provide the latent heat of melting or fusion. The assigned kinematic diffusivity (molecular diffusion) of one component in another - i.e. solute in solvent – controls the motion of the components and influences the mixing between the two components. The overall mixing of the solute in solvent is dependent on the advective mass transport and molecular diffusivity. The advective mass transport is dependent on the magnitude of the Marangoni forces, buoyancy forces and the resistance to flow (Darcy force) cause by the mushy zone. Buoyancy and Marangoni forces are generated by temperature and/or composition variations in the bulk or at the surface, respectively.

5.2 Model Assumptions

The following assumptions have been made in this mathematical model:

1) The fluid flow in the cylindrical cell (beaker) has been assumed to be laminar. This results from the low Reynolds number (1815) estimated based on a rectangular cell of hydraulic length of 0.055 m, maximum velocity 0.1 m/s, density 990 kg/m^3 and dynamic viscosity 0.003 Pa s. The flow can be considered laminar if Re < 2300.

2) The fluid in the beaker cell has been assumed to be incompressible. Liquids are generally incompressible, i.e. they cannot be compacted or compressed (made more dense) and then retract back to original density. In the model, the liquid density is a function of temperature. It is not related to pressure and the change in pressure with the change in density is minimal.

3) The top surface of the solid solute and the solvent has been assumed to be flat. During the experiments, this was not the case. The curvature of the water at the walls of the glass cell has been

neglected. Also, the waves generated in the free surface of water by dipping of the solid solute have been neglected.

4) The heat transfer from the top surface of the water to the atmosphere is negligible since the experiment was of short duration (around 80 s) and the temperature difference between the ambient air and the water was relatively low.

5) The heat transfer from water through the sides and bottom of the beaker cell was assumed to be negligible because the glass beaker is a good insulator and there is a small driving force for heat transport between the ambient air and the beaker.

5.3 Governing Equations

In the model, the governing equations of mass, momentum, energy and mass fraction conservation [80, 81] are solved in order to predict the fluid flow, compositional fields and the heat transport during the process of dissolution:

$$\frac{\partial \rho}{\partial t} = - (\nabla \cdot \rho v) \qquad \qquad \textbf{Eq. (5.1)}$$

$$\frac{\partial (\rho v)}{\partial t} = -[\nabla \cdot \rho v v] - \nabla p - [\nabla \cdot \tau] + \rho g + S_M \qquad \qquad \textbf{Eq. (5.2)}$$

$$\rho C_p \left(\frac{\partial T}{\partial t} + v \cdot \nabla T \right) = \nabla \cdot (k \nabla T) + S_E \qquad \qquad \textbf{Eq. (5.3)}$$

$$\frac{\partial (\rho_\alpha)}{\partial t} = -(\nabla \cdot \rho_\alpha v) - (\nabla \cdot j_\alpha) + r_\alpha \qquad \qquad \textbf{Eq. (5.4)}$$

where ρ is the density (kg m^{-3}), t is the time (s), v is the velocity (m s^{-1}), p is the pressure (kg m^{-1} s^{-2}), C_p is the specific heat (J kg^{-1} K^{-1}), g is the acceleration due to gravity (m s^{-2}), T is the temperature (K), k is the thermal conductivity (W m^{-1} K^{-1}), τ is viscous stress (N m^{-2} or kg m^{-1} s^{-2}), S_M is a momentum source term (N m^{-3} or kg m^{-2} s^{-2}), S_E is an energy source term (W m^{-3} or kg m^{-1} s^{-3}), ρ_α is mass concentration of species α (kg m^{-3}), j_α is the molecular mass flux of species α (kg m^{-2} s^{-1}), r_α is the rate at which species α is produced by chemical reaction (kg m^{-3} s^{-1}).

Equations 5.1 – 5.4 are applicable to transient problems, assuming the fluid to be incompressible and of Newtonian behavior. For Newtonian fluids, the stress tensor is linearly proportional to the velocity gradient tensor and viscosity μ (Pa s or kg m^{-1} s^{-1}), shown in **Eq. (5.5)**:

$$\tau = -\mu \left(\nabla v + \nabla v' \right) \qquad\qquad \textbf{Eq. (5.5)}$$

where ∇v is the tensor of velocity gradient with components $\frac{\partial v_j}{\partial x_i}$, $\nabla v'$ is the transpose of ∇v.

Eq. (5.1) describes the conservation of mass in vector form. The vector ρv is the mass flux and its divergence equals the net rate of mass flux per unit volume. Equation (5.1), also called the Continuity Equation, states that the rate of increase (accumulation) of mass per unit volume is equal to the net rate of mass addition per unit volume by convection. This equation is developed by writing a mass balance over a volume element, fixed in space and through which fluid is flowing.

Eq. (5.2) is the momentum conservation equation which equates the rate of increase of momentum per unit volume to the sum of the rate of momentum addition by convection per unit volume $(\nabla \cdot \rho v v)$, rate of momentum addition by molecular transport per unit volume $(-\nabla p - [\nabla \cdot \tau])$, external forces applied to the fluid per unit volume (ρg) and sum of the momentum source terms (S_M). The convective terms describe the transport of momentum by the bulk flow of the fluid while the molecular transport terms describe momentum transfer by interaction between the adjacent rows of molecules thereby transmitting the momentum in the direction normal to the velocity.

Eq. (5.3) is based on the conservation of energy equation where the total energy of a thermodynamic system includes the internal energy of the system and the work done on the system. Since the fluid is incompressible, the change in pressure in the system is zero and hence the work done on the system is zero as well. In this case, the conservation of energy is also called the heat balance equation and equates the rate of increase of energy per unit volume to the rate of energy addition per unit volume by convective transport, heat conduction and external addition / internal heat generation.

Eq. (5.4) is based on the general advection-diffusion conservation equation for a component in a multicomponent fluid. In the form presented, this equation is the equation of continuity for species α in a multicomponent mixture. It describes the change in mass concentration of species α with time at a fixed

point in space through the diffusion and convection of α, as well as by chemical reactions that can produce or consume α. This equation has been used to predict composition of species α in a two-component mixture.

In a two species or component system, the components mix with each other through the combined effects of convection and molecular diffusion. The convective mixing occurs through differential bulk motion of the species while the molecular mass diffusion is by interaction between the molecules of the two species. Molecular mass diffusion is possible if the species (or components) in the system are soluble in each other. The molecular transport of one component (α) relative to another (β) is known as 'mass diffusion' or concentration diffusion. The concentration of these components is given by 'mass fraction', ω_α and ω_β. The mass fraction, ω_α is defined by the mass of a component α divided by the mass of all the components (α and β) in a given volume.

The molecular mass transport between the components in a system is defined by Fick's law of binary diffusion which in simple terms states that the mass diffusion of one component in to another is proportional to the difference in the mass fraction between the two components over a known distance, **Eq. (5.6)**. In other words, Fick's first law postulates that the flux of material across a given plane is proportional to the concentration gradient across that plane, **Eq. (5.7)**. It quantifies the movement of molecules from a region of higher concentration to a region of lower concentration. Fick's first law can be expressed as:

$$\frac{w_{\alpha y}}{A} = -\rho D_{\alpha\beta} \frac{d\omega_\alpha}{dy} \qquad\qquad \textbf{Eq. (5.6)}$$

or,

$$j_{\alpha y} = -\rho D_{\alpha\beta} \frac{d\omega_\alpha}{dy} \qquad\qquad \textbf{Eq. (5.7)}$$

where $w_{\alpha y}$ is the mass flow of species α in the y-direction (kg s^{-1}), A is the area of the plane (m^2), ρ is the density of the system (kg m^{-3}), $D_{\alpha\beta}$ is the diffusivity or diffusion coefficient of α in β (m^2 s^{-1}), $j_{\alpha y}$ is the mass flux of species α in the y-direction (kg m^{-2} s^{-1}), y is the direction along which the concentration

gradient exists (m), ω_α is the mass fraction of species α (no unit). The negative sign indicates that the direction of flow is from high to low concentration.

5.3.1 Momentum source term

5.3.1.1 Buoyancy driven flow

Density differences caused by temperature and compositional gradients in the domain will cause buoyancy driven flow where denser liquid tends to sink while low density liquid rises. During the dissolution of ice in water, significant temperature gradients are present which produce significant density gradients. During the dissolution of solid ethanol in water, both temperature and compositional gradient exists which offset each other to determine the buoyancy induced flow. The buoyancy effect in the domain is implemented by adding a momentum source term $S_{M,buoy}$ to the right hand term in the **Eq. (5.2)**:

$$S_{M,buoy} = g\,(\rho - \rho_{ref}) \qquad\qquad \textbf{Eq. (5.8)}$$

where $S_{M,buoy}$ (kg m^{-2} s^{-2}) is the momentum source term for driving the fluid flow by buoyancy, g (m s^{-2}) is the acceleration due to gravity, ρ_{ref} (kg m^{-3}) is a reference density, and ρ is the current local density which varies with both temperature and composition.

The density difference $(\rho - \rho_{ref})$ which causes buoyancy can be evaluated by either: a) Boussinesq approximation, or b) the actual density difference. Both of these methodologies have been considered in this model.

In addition to absorbing heat during melting, there is a change in volume: ice contracts and ethanol expands. In either case, there will be a net change in the volume of the system after the solute completely melts assuming no solute/solvent mass change occurs during the experiments. The computational model developed in ANSYS CFX is a constant volume model based on a fixed mesh. The model domain does not deform or change to account for the change in volume due to thermal contraction or shrinkage. Instead, the change in density associated with the phase change and temperature variation will result in a change in mass in the system. Considering the change in density due to the phase change (refer to section 5.5), the overall mass change due to the ice to water phase transformation is calculated to

45

be 0.02 g over the entire simulation time. Additionally, the mass loss associated with the temperature variation of the solvent was estimated to be ~1% (ice/water case, from 275 K to 323 K: temperature range of liquid water in the experiments). Thus, the errors associated with density variation and mass conservation are small and have been neglected.

5.3.1.2 Darcy Flow

In addition to buoyancy, another effect that has been included in the momentum source term (S_M) is the mushy zone resistance to flow or Darcy force. ANSYS CFX solves the mass, momentum and energy equations throughout the prescribed domain and treats the three phases: solid, liquid and mushy zone as a single continuum with varying properties where the transition from solid to liquid melting behavior is taken into account by dampening the flow at the solid-liquid interface. Darcy forces are caused by the resistance to flow through the partially solid structure in the mushy zone. To include the restriction to the flow within the mushy zone, a Darcy momentum source is included:

$$S_{M,darcy} = -\frac{\mu}{K}(v)$$

Eq. (5.9)

where, μ is the viscosity (kg m^{-1} s^{-1}), K is the permeability (m^2) and v is velocity (m s^{-1}). The permeability K can be calculated using Carman-Kozeny equation which has been successfully used to describe the variation in permeability for porous dendritic structures:

$$K = \frac{(1 - f_s)^3}{Df_s^2}$$

Eq. (5.10)

where f_s is the fraction solid, D is a coefficient (m^{-2}) related to the specific solid-liquid interfacial area in the mushy zone. For simplicity, D has been assumed to be equal to 1.67×10^{10} m^{-2} [82]. The temperature range over which the phase change from solid to liquid occurs - i.e. f_s changes from 0 to 1 in **Eq. (5.10)** - is set to 1 K in the model, consistent with the range used for the change in viscosity. A more detailed explanation of the variation of f_s with temperature for both ice/water and ethanol/water in the mathematical model is provided in section 5.5.

The total momentum source term is the combination of buoyancy (both thermal and compositional) and Darcy forces calculated in each cell of the domain is given by:

46

$$S_M = S_{M,buoy} + S_{M,darcy}$$ <div align="right">**Eq. (5.11)**</div>

5.4 Domain

The domain used in the model is a section of a cylinder with 50 mm radius and 60 mm depth whose dimensions are based on the experimental cell employed in the water analogue model. The geometry was simplified to a 5° segment (pie-shaped geometry), assuming axisymmetric conditions, to reduce the computational requirements. CFX does not support 2-D geometries, so a symmetric 3-D geometry was implemented. Details of the model domain are shown in **Figure 5.1**.

The mesh size was selected to allow accurate prediction of the transport processes associated with dissolution while limiting the computational time. The mesh used for the analysis is shown in **Figure 5.1 (b)** and summarized in **Table 5.1**. The mesh was produced using the pre-processing software, ANSYS ICEM CFD version 12.1. The whole domain was meshed with hexahedra elements with radial and axial edge lengths of 0.5 mm and one element in the circumferential direction. The domain was cropped at the center edge by one element length along the centerline of 60 mm. This was done because the quality of the mesh in the removed section of the pie was poor and led to instabilities, shown in **Figure 5.1 (a)**.

The initial solute and solvent regions were defined via a variable calculated using the CFX Expression Language (CEL). Algebraic equations were developed to define the initial mass fractions for the two regions consistent with the experiments, described in Chapter 4.

Table 5.1 Summary of the mesh geometry

Number of Nodes	23760
Number of Elements	11662
Element type	Hexahedra
Min x, Max x	0.5 mm, 50 mm
Min y, Max y	-60 mm, 0 mm
Min z, Max z	-4.35 mm, 0 mm
Max Edge Length Ratio	11.46
Mesh size	0.5 mm
Volume	6514.45 mm^3

(a)   **(b)**
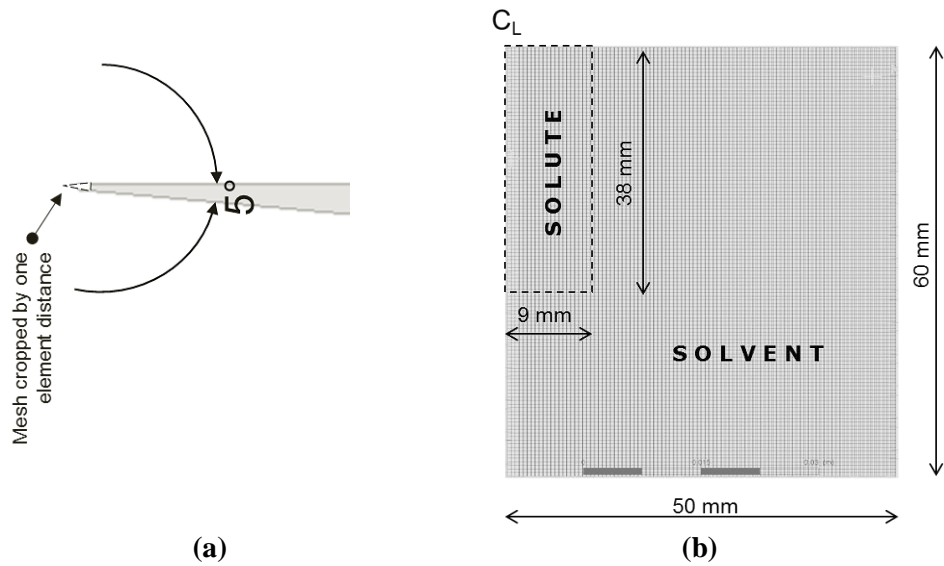
Figure 5.1 Domain: (a) Cropped section in Mesh; (b) Geometry, Front view of Mesh

5.5 Material Properties

To accurately predict the results of the water analogue experiments, it is important to have an accurate description of the material properties over the relevant range of temperature and compositions. Most of the thermo-physical properties like density, specific heat, viscosity, thermal conductivity, and latent heat were based on the values reported in the literature [76, 77, 83, 84]. In some cases, data for the

48

relevant temperature ranges above the liquidus temperature was obtained while in a few cases, some of the properties were extrapolated as a function of temperature to match theoretical understanding. Obtaining values for temperatures below the melting point proved difficult. Therefore, below the solidus temperatures the values of the material properties were based on theoretical understanding with just one constant value over the whole temperature range.

For a multi-component model like: ethanol in water or ice in water; the fluid system is comprised of two components, one component as solute and other as solvent. In the model, density, specific heat and thermal conductivity were calculated assuming an ideal mixture rule where the properties of the mixture are based on the properties of the components and their proportions (mass fraction or concentration) in the mixture, according to:

$$\frac{1}{P} = \frac{\omega_\alpha}{P_\alpha} + \frac{\omega_\beta}{P_\beta} \qquad\qquad \textbf{Eq. (5.12)}$$

where P is the relevant fluid/material property (density, specific heat or thermal conductivity), P_α and P_β are the properties of solute and solvent, respectively, and, ω_α and ω_β are the mass fractions of the solute and solvent, respectively. The sum of ω_α and ω_β is equal to 1.

The default functionality of ANSYS CFX is to compute thermodynamic properties of mixtures assuming that they are ideal mixtures. This is not appropriate if the solute has no effect on the solvent properties. Therefore in the ethanol/water case, one of the mixture properties has been explicitly specified to override the ideal mixture rule implemented by the solver. This exception has been applied to define the dynamic viscosity for ethanol dissolution in water as a function of liquid fraction. The data for the liquid fraction of ethanol-water mixture was defined based on the ethanol-water phase diagram.

The material properties used to describe ethanol and water in the computational model are:

a) Liquid Fraction: The liquid fraction of ethanol as a function of temperature was computed based on ethanol-water phase diagram. The ethanol-water system exhibits complex phase change behavior depending on ethanol concentration. The phase diagram or the melting-point diagram for ethanol-water developed by Ohkubo et al. [85] is shown in **Figure 5.2 (a)**. At all concentrations (ethanol mass fraction) except the eutectic (92 %, -125.5 °C), there is a temperature range where the solid and liquid phases co-

exist together. The liquid and solid phase boundaries in **Figure 5.2 (a)** were approximated with straight lines. The modified phase diagram which was incorporated into the computational model is shown in **Figure 5.2 (b)**. When two liquids mix, the mass fraction (concentration or composition) of ethanol and the temperature at each location are used to determine the fractions of solid or liquid phases by employing the lever rule.

$$f_l = \frac{\omega_s - \omega_\alpha}{\omega_s - \omega_l}$$

Eq. (5.13)

where ω_α is the mass fraction of solute (ethanol) α for the given composition, ω_s is the mass fraction of solute (ethanol) α at the solidus, ω_l is the mass fraction of solute (ethanol) α at the liquidus and f_l is the fraction liquid.

For the ice/water system, the phase diagram was not required because the experiment involved the dissolution of solidified water in liquid water. Since both the solid and the liquid were of same composition, a linear variation of f_s over a temperature range of 1 K was employed, as shown in **Figure 5.3**.

(a)

(b)
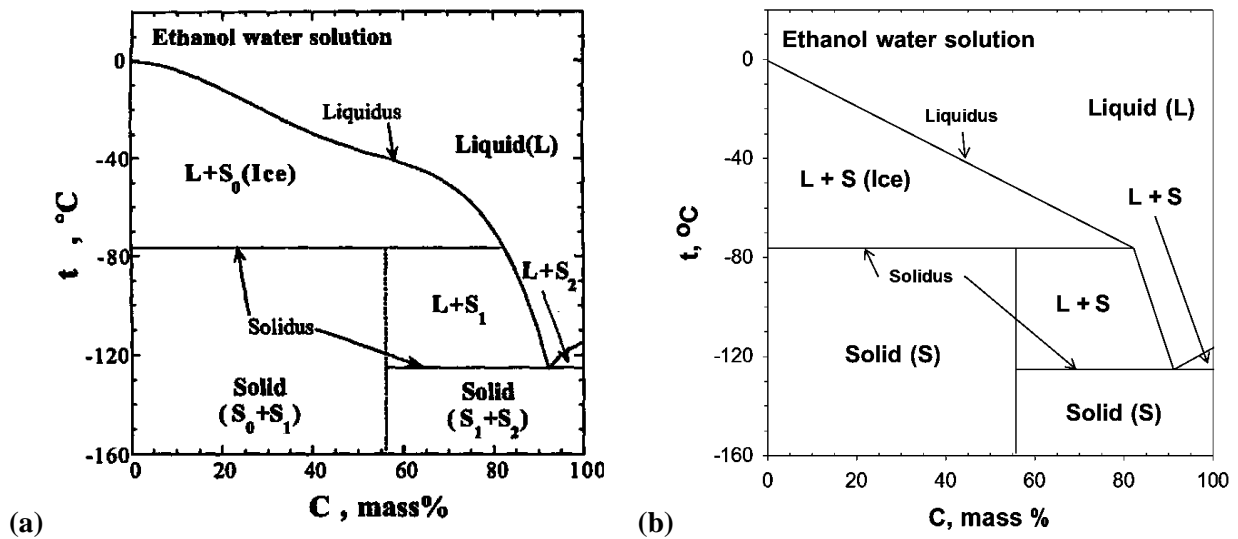
Figure 5.2 Ethanol/water: Variation of liquid fraction with temperature in accordance with ethanol-water phase diagram: (a) Phase diagram of ethanol-water solution [85] **(b) Approximated phase diagram (included in model) for ethanol-water solution**
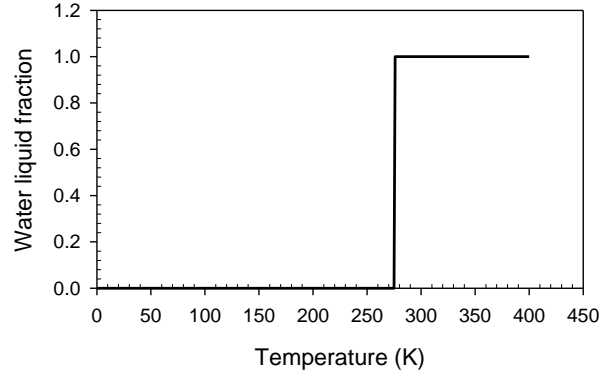
Figure 5.3 Ice/water: Variation of liquid fraction with temperature

b) Effective Specific Heat: During melting, latent heat is absorbed during the solid to liquid phase transformation. This phenomenon can be described in a computational model as either an energy sink term or an effective specific heat. For easy implementation and faster computation, an effective specific heat methodology has been used in this work. In this methodology, the specific heat values used in the model are augmented to correct for the variation in enthalpy over the phase change interval. The specific heat (C_p) is increased to an effective specific heat ($C_{p,eff}$) by adding the specific heat due to latent heat of melting ($C_{p,latent}$) during the phase change temperature interval, given by:

$$C_{p,eff} = C_p + C_{p,latent}$$ **Eq. (5.14)**

where

$$C_{p,latent} = -L\frac{df_s}{dT}$$ **Eq. (5.15)**

In the above expressions, f_s is the fraction solid, L (J kg^{-1}) is the latent heat absorbed, C_p is the specific heat (J kg^{-1} K^{-1}) and $\frac{df_s}{dT}$ is the slope of the fraction solid curve with respect to temperature (K^{-1}).

The melting point of ethanol is 159 K [75] and the latent heat of melting is 109 kJ kg^{-1} [75]. The use of a melting point, as opposed to a melting temperature range, could not be incorporated in to the mathematical model due to convergence problems. To address this issue, the phase transformation in ethanol was assumed to take place over a temperature range of 15 K, with the liquidus at 150 K and solidus at 165 K. In the ice/water case, a similar concession was made to change the melting point of ice

51

from 273 K. For water, the phase transformation was assumed to take place over a temperature range of 6 K, with the liquidus temperature of 272 K and the solidus temperature of 278 K. The latent heat of melting for water is equal to 334 kJ kg^{-1} [75]. As explained, the specific heat has been modified to account for the latent heat absorption. The temperature range over which it has been modified is larger than the temperature range over which the fraction solid, density, dynamic viscosity and thermal conductivity vary in both the ice/water and ethanol/water cases. **Figure 5.4** shows the variation of specific heat as a function of temperature for ethanol and water.
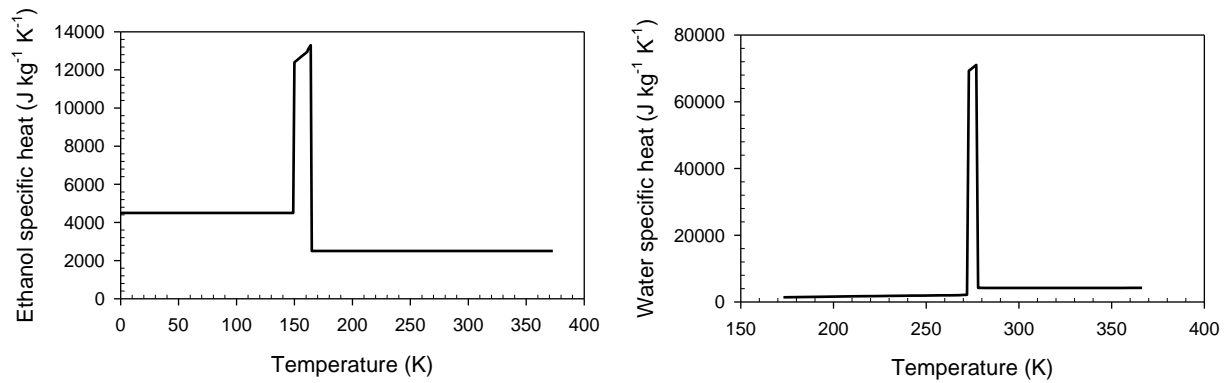
Figure 5.4 Variation of specific heat with temperature for ethanol and water

c) Density: The density of ethanol was approximated to be 880 kg m^{-3} from 0 to 159 K. Above 159 K, the material properties of ethanol transition and the density data for ethanol are available from [77]. Similarly, the density values for water below 275 K were assumed to be 916 kg m^{-3}. Above 275 K, the material properties of water were assumed to transition to the liquid values and the density values for water above 275 K were obtained from [76]. **Figure 5.5** shows the variation of density as a function of temperature for ethanol and water with a solid-to-liquid transition of 1 K.
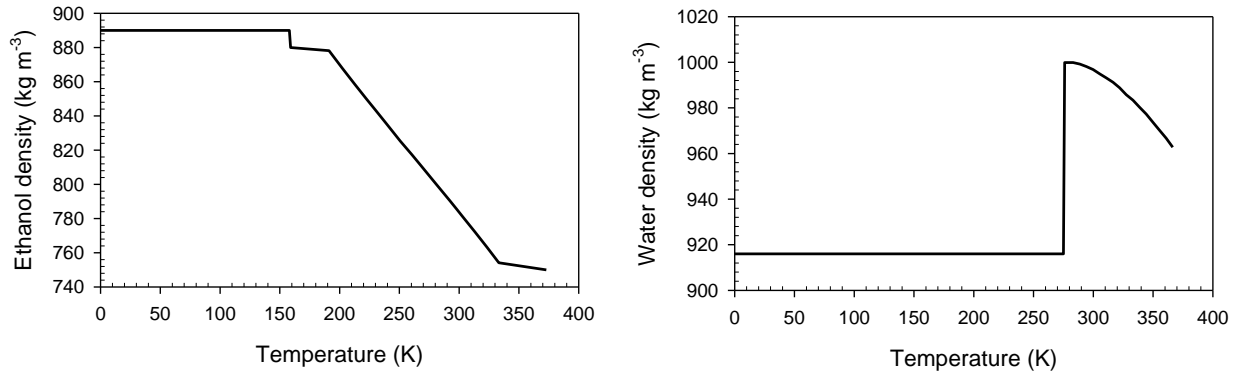
Figure 5.5 Density variation with temperature for ethanol and water

d) Dynamic viscosity: The viscosity of both ethanol and water below their solidus temperatures was assumed to be 10 Pa s. This assumption is necessary to restrict the motion of the material that should be solid but is treated as a fluid because of the continuum approach applied in this model. Above the liquidus temperature, the viscosity data were taken from the literature [82], [86]. The viscosity variation for ethanol and water as a function of temperature is shown in **Figure 5.6** for a solid-to-liquid transition of 1 K. In both cases, there is a fourth order change in the viscosity between the solid and liquid phases.
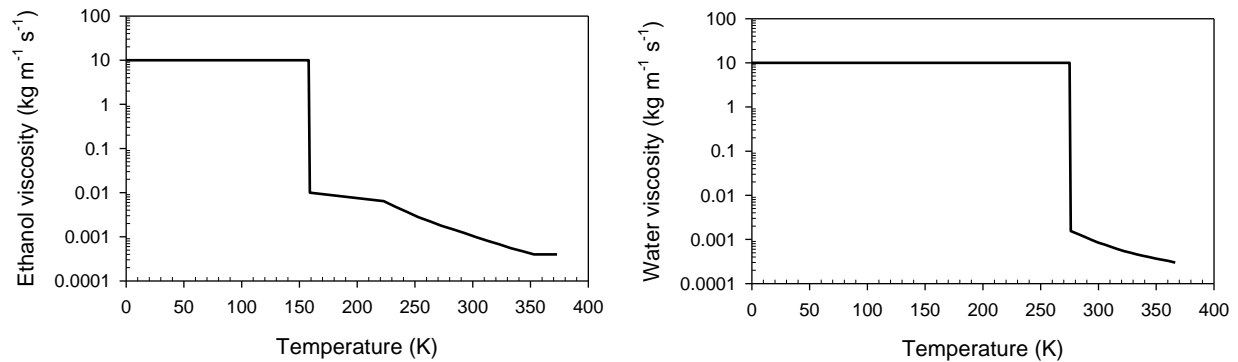
Figure 5.6 Dynamic viscosity variation with temperature for ethanol and water

e) Thermal conductivity: The thermal conductivity of ethanol below the solidus temperature was assumed to be 1.5 W m^{-1} K^{-1} because no literature could be found. Likewise for water, the thermal conductivity data was found for 276 K (2.2 W m^{-1} K^{-1}), but below this temperature, a value of 2.8 W m^{-1}

53

K^{-1} was assumed. The thermal conductivity for ethanol and water above the liquidus temperature were obtained from [76, 77]. The variation of thermal conductivity for ethanol and water as a function of temperature is shown in **Figure 5.7** for a solid-to-liquid transition of 1 K.
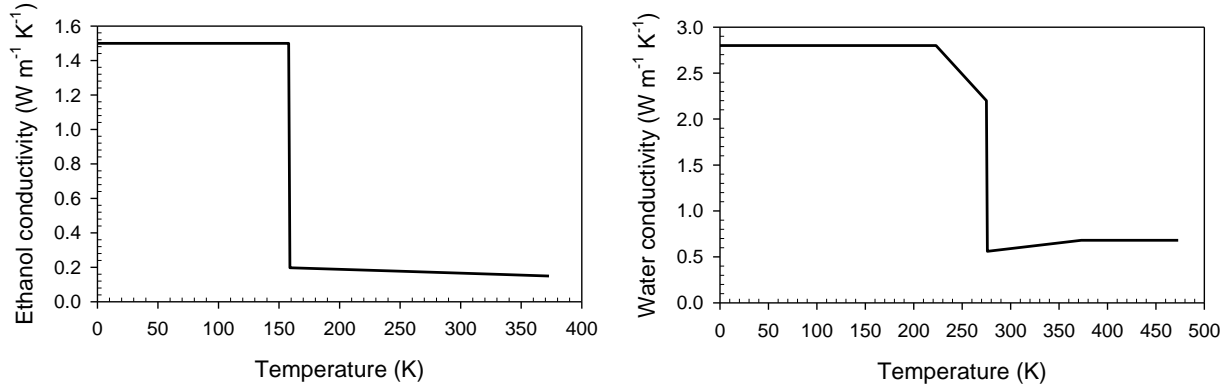
Figure 5.7 Thermal Conductivity variation with temperature for ethanol and water

f) Solute diffusion: The solute diffusivity is described by the molecular diffusion coefficient of a solute in a particular solvent. It defines how rapidly the solute would move through the solvent in the absence of convection. For convection dominated flows, solute diffusion generally has a little effect since the convective processes dominate. The molecular diffusion in fluids is dependent on its viscosity, the higher the viscosity, the lower is the molecular diffusion. Therefore, molecular diffusion in solids is negligibly zero. In this model, the solute kinematic diffusivity is dependent on the viscosity of the mixture. The viscosity of the mixture is a function of liquid fraction which is calculated using the ethanol-water phase diagram (as discussed earlier). The change in solute kinematic diffusivity with viscosity of fluid mixture is shown in **Figure 5.8**.

In ice/water case, there is limited molecular diffusion because there is no compositional gradient between the two components. In this case, both the components consist of identical molecules of identical size and concentration; therefore, it is not applicable for the ice/water case. The diffusion of the water soluble dye (mixed in ice solute) in the water solvent has been neglected because the mixing is primarily by advection and it is believed that the diffusion of dye is very slow in comparison to it.
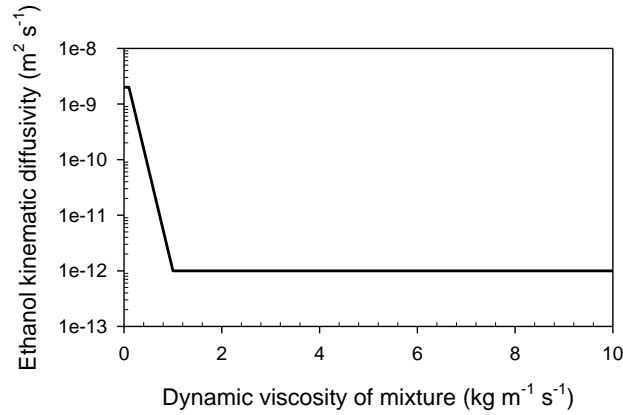
Figure 5.8 Kinematic diffusivity variation with temperature for Ethanol

g) Surface Tension Coefficient: The influence of Marangoni forces on the top surface flow pattern is dependent on the surface tension coefficients of the fluid. The surface tension coefficients for the solute and solvent are known to be functions of composition (mass fraction) and/or temperature. The data for the surface tension coefficient for ethanol with respect to temperature and mass fraction were obtained from Vhquez et al. [84]. The surface tension coefficient variation for ethanol in water as a function of mass concentration is shown in **Figure 5.9 (a)**. **Figure 5.9 (b)** shows the surface tension variation with temperature for both water and ethanol. The slope of the curve for the surface tension variation with temperature for both ethanol and water is constant and parallel, in other words the surface tension coefficient with respect to temperature for both liquids is same.

(a)   **(b)**
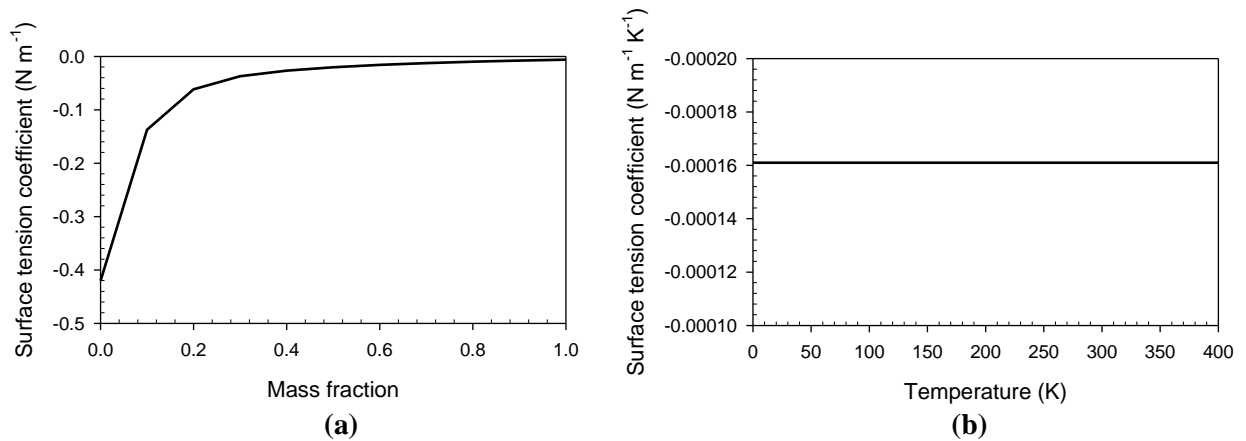
Figure 5.9 Surface tension coefficient variation with (a) mass fraction ethanol and (b) ethanol and water temperature

5.6 Initial Conditions

The initial conditions of temperature, pressure, velocity and mass fraction for both ice in water and ethanol in water were defined based on the water analogue experiments. These initial conditions are summarized in **Table 5.2**. For each experiment, the starting temperature for both the solute and the solvent were recorded and has been used as the initial or starting temperature in the computational model. Fluid motion (small velocities) was initiated when dipping the solid solute in to the stationary solvent during the experiments. These small velocities have been neglected in the model because it was not possible to characterize the velocity and it was observed that this motion was small compared to that generated by dissolution. Therefore, it was assumed that at time 0 s, the model is stationary and there is no residual velocity in the solvent due to the presence of the solute. On a similar note, the initial pressure was set to 0 Pa.

Table 5.2 Initial conditions

System	Initial Temperature		Water Mass Fraction	
	Solute	Solvent	Solute	Solvent
Ice in water	261.35 K	317.85 K	1	1
Ethanol in water	81.6 K	318 K	0	1

5.7 Boundary Conditions

When solving the governing conservation equations, appropriate boundary conditions are needed. Boundary conditions are specified based on the experimental conditions, described in Chapter 4. The boundary conditions are the same for both experimental cases, i.e. ice in water and ethanol in water cases. The boundary conditions have been selected to represent the physics of the experimental cell in order to achieve accurate results. Where assumptions were necessary, the rationale and effect of these assumptions has been assessed. **Figure 5.10** shows a schematic representation of the domain and the boundary conditions applied.

a) Top surface: The top surface of the solvent and solute has been treated as an adiabatic, free-slip wall. The surface tension gradient caused by temperature and/or compositional variation on the liquid surface leads to the development of Marangoni force, which causes the liquid to flow from regions of low surface tension to the regions of high surface tension. This force has been applied to the top surface (boundary) of the liquid as a specified shear stress, through a user-written subroutine using the following mathematically expression:

$$F_{Mara} = F_{Mara,Ther} + F_{Mara,Comp} = \frac{\partial \sigma}{\partial T}\frac{\partial T}{\partial n} + \frac{\partial \sigma}{\partial C}\frac{\partial C}{\partial n} \qquad \textbf{Eq. (5.16)}$$

where σ (N m^{-1}) is the surface tension, T (K) is the temperature, C is the composition fraction, n (m) is the direction normal, $\frac{\partial \sigma}{\partial T}$ (N m^{-1} K^{-1}) is surface tension coefficient with respect to temperature, $\frac{\partial \sigma}{\partial C}$ (N m^{-1}) is the surface tension coefficient with respect to composition, $\frac{\partial \sigma}{\partial T}\frac{\partial T}{\partial n}$ is the Marangoni force caused by temperature gradient, and $\frac{\partial \sigma}{\partial C}\frac{\partial C}{\partial n}$ is the Marangoni force caused by compositional gradient.

The directional components of these forces are calculated as **Eq. 5.17 - 5.19**, given by the sum of the Marangoni stresses based on temperature and composition in a given direction. Since, this force is applicable parallel to the surface; the y-component of this force is zero.

$$F_{Mara,x} = F_{Mara,Comp,x} + F_{Mara,Ther,x} \text{ (kg m}^{-1}\text{ s}^{-2}) \qquad \textbf{Eq. (5.17)}$$

$$F_{Mara,y} = 0 \text{ (kg m}^{-1}\text{ s}^{-2}) \qquad \textbf{Eq. (5.18)}$$

$$F_{Mara,z} = F_{Mara,Comp,z} + F_{Mara,Ther,z} \text{ (kg m}^{-1}\text{ s}^{-2}) \qquad \textbf{Eq. (5.19)}$$

$F_{Mara,Comp,x}$ is the compositional Marangoni force acting in the x-direction, given by the product of the coefficient of surface tension with respect to composition in x-direction and the associated solute compositional gradient in the x-direction. Similarly, $F_{Mara,Ther,x}$ is the thermal Marangoni force acting in the x-direction, given by the product of the coefficient of surface tension with respect to temperature in the x-direction and the associated temperature gradient in the x-direction. Likewise, for $F_{Mara,Comp,z}$ and $F_{Mara,Ther,z}$.

b) Bottom and side surfaces: The bottom and side walls are no slip walls assuming that the velocity of the solvent at the glass wall is zero due to the adherence of the fluid to the wall. These walls are also assumed to be adiabatic.

c) Front and back surface: A symmetry boundary condition is applied to both the front and the back faces of the 5° geometry slice. This boundary condition imposes a constraint that the flow on one side of the plane is the mirror image of flow on the opposite side. Thus, the normal component of any variables like, velocity, etc. is set to zero at the symmetry plane boundary.

d) Center: The thermal boundary condition was set as adiabatic thereby allowing no heat transfer to occur from and to the center. Also, the fluid flow boundary condition was set as free slip thereby providing no restriction to the fluid flow at the interface.
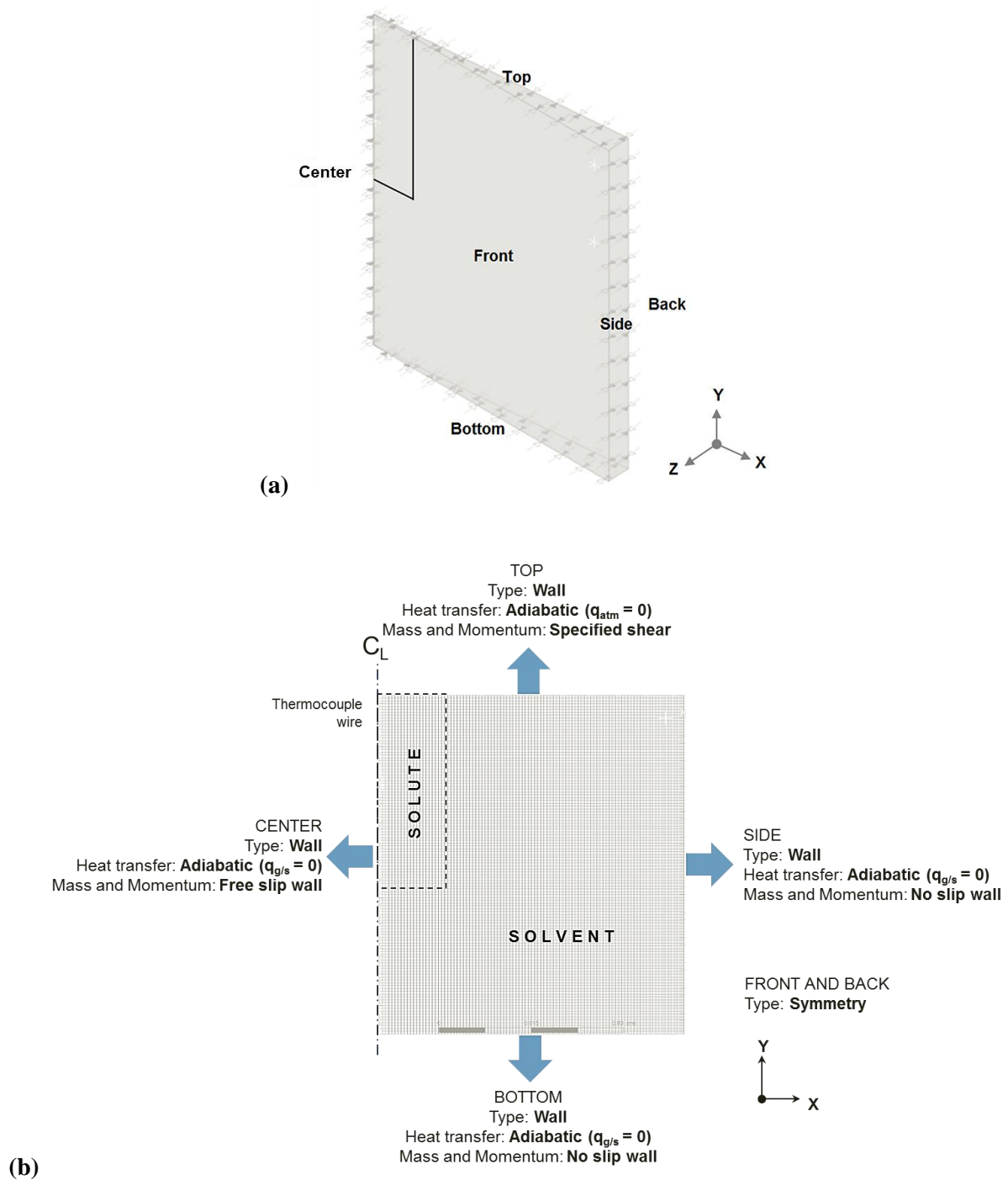
(a)

(b)

Figure 5.10 Boundary conditions: (a) Nomenclature of the boundaries (b) Thermal and fluid boundary conditions applied at each of the boundaries

6 Results and Discussion

In this chapter, the results from the computational model and the water analogue experiments will be presented. A comparable result between the two indicates that the thermo-fluid-compositional model developed in ANSYS CFX 12.0 has the capability to predict the dissolution and homogenization process. By extension, this model should then accurately describe the relevant phenomena in the Ti-6Al-4V system. The key factors impacting dissolution of a lower melting point solid in a liquid of different composition include: thermal buoyancy (B_T), compositional buoyancy (B_C), thermal Marangoni (M_T) and compositional Marangoni (M_C). **Figure 6.1** schematically represents the specific cases that will be discussed and the expected outcomes. A brief description on each of the cases is described below:

Case I - B_T only: A simple case selected as the starting point of this study. In **Figure 6.1 (a)**, solid water (ice) acts as a solute dipped in water solvent allowing evaluation of thermally-driven buoyancy fluid flow forces in the absence of compositional effects. By completely immersing the ice to the center of the pool, it is possible to suppress Marangoni forces.

Case II - B_T and M_T (baseline): The first step in adding complexity was the generation of surface tension driven flow due to the presence of temperature gradients only. In **Figure 6.1 (b)**, ice acting as solute was partially dipped into the solvent allowing the evaluation of thermal Marangoni forces along with thermal buoyancy forces. Since, there was no compositional difference between the solute and solvent material, compositional effects were absent.

Case III - B_T and B_C: The next step in complexity was to change the composition of the solute material from water to pure ethanol and completely immersing the solute. In this case the effects of compositionally dependent buoyancy are combined with those of thermal buoyancy in the absence of Marangoni forces. **Figure 6.1 (c)** shows the schematic of the fluid flow pattern developed and the presence of two fluid flow drivers active in this case.

Case IV - B_T, B_C, M_T and M_C: This case involves the dissolution of solid pure ethanol in water where the effects of both thermal and compositional Marangoni forces at the top surface and thermal and

compositional buoyancy in the bulk are active. In **Figure 6.1 (d)**, there is a noticeable change in both the flow pattern, fluid forces involved and the interface profile when compared to the previous cases.

(a) Case I- B_T only;   (b) Case II- B_T & M_T;   (c) Case III- B_T & B_C;   (d) Case IV- B_T, B_C, M_T, M_C
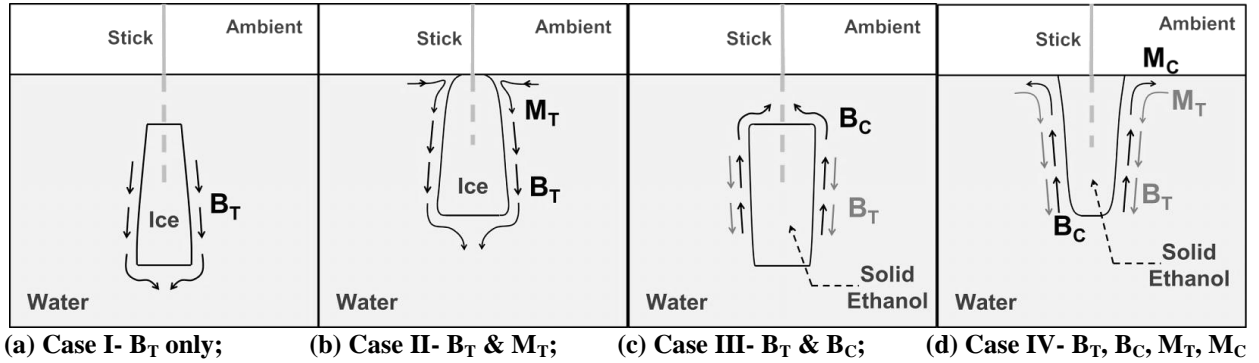
Figure 6.1 Schematic representation of the flow pattern, forces involved and solid/liquid interface

In the coming sections, the results of the water-ethanol numerical and physical analogue models are presented in three segments: i) study of the fluid flow drivers, ii) the change of temperature, and iii) the evolution of the solid-liquid interface profile. Following this, the experimental repeatability of the water-ethanol physical model will be discussed. Later, a sensitivity analysis was performed with the water analogue experiment and the numerical model to assess the sensitivity of the system to the changes in key numerical and process parameters. Finally, the results of the model applied to Al/Ti system are presented.

6.1 Water Analogue Model

6.1.1 Fluid Flow

Ice/Water: Starting with the cases limited to thermal effects, **Figure 6.2** and **Figure 6.3** show experimental results and model results for Case I and Case II, respectively at every 10 seconds after the ice is dipped into the water. The transient development of the solid/liquid interface profile and the fluid flow can be observed from 0 s to 65 s. At 0 s, the initial conditions in the model are nearly identical to that of the experiment, both in terms of geometry and temperature of the solute and the solvent.

In Case I, the fluid flow is predominately directed downward along the solid-liquid interface. This is due to the drop in solvent temperature around the cold solute which leads to an increase in density,

resulting in a downward flow of water adjacent to ice. At 10 s, the experiment and the model prediction of the solute interface are nearly identical because both the image shows preferential dissolution of the ice solute from the bottom interface. The experimental image show deep-orange region near the bottom-center of the solute suggesting high amount of dissolution around that region. Similar trend can be observed with the model prediction; the velocity vectors in that area suggest a velocity of ~0.02 m/s in that region.

Case II, in addition to the downward directed temperature-dependent buoyancy flow, there exists temperature-dependent Marangoni flow. The presence of the cold solute (ice) on the surface of the water results in high surface tension liquid at the interface compared to that of the liquid away from the interface. The cold liquid with high surface tension pulls strongly on the surrounding liquid with low surface tension, causing the liquid to flow away from regions of low surface tension, resulting in flow directed towards the center. The inward flow of the liquid on the surface due to thermal Marangoni increases both heat and mass transfer at the top surface resulting in increased dissolution of the solute sample on the top surface, as observed in **Figure 6.3**, 10 s.

In both the cases, the model correctly determines the excess dissolution occurring along the bottom of the solute sample towards the center, as seen at 20 s leading to a concave shape. In both the cases, the shape of solid/liquid interface in the experiment and in the model prediction, begin to diverge from 30s onwards, i.e. the solute is wider at the top than the bottom in model, and the opposite is observed in the experiment. At 50 s and above, for both the cases the model correctly predicts the height over which cold liquid settles at the bottom (highlighted in the figure) which matches with the height over which the dyed water in the experiment settled at the bottom.

There is good agreement between the experimental results and modeling results in terms of the shape of the solid-liquid interface, the direction of the flow pattern and total time for dissolution in both the cases. It should be noted that the width of the solid solute in experimental images appears <10% wider than the model due to refraction.

Ethanol/water: **Figure 6.4** and **Figure 6.5** show the flow patterns of the ethanol/water case at every 5 s from the time of dipping for Case III and Case IV, respectively. Ethanol has a lower density than water in both the solid and liquid states. As ethanol melts, the increased concentration of ethanol at the solid/liquid interface causes the adjacent fluid flow due to compositional buoyancy to be upwards in contrast to the thermal buoyancy effects. This causes the ethanol mixture to accumulate at the top for both Cases III and IV.

Case III is assumed to be not influenced by Marangoni force. It is known that the movement of low density ethanol to the top surface will create a gradient in composition and temperature at the surface which will give rise to thermal and compositional Marangoni forces at the surface. But since the solute is immersed >10 mm beneath the surface, the Marangoni force acting at the solute interface is nil. Also, the magnitude of the velocity at the top surface due to Marangoni force in Case III was found to be ~0.12 to 0.14 m s^{-1} in comparison to Case IV where the velocity was found to be ~0.18 – 0.22 m s^{-1} respectively.

In Case III, (**Figure 6.4**) the model was able to predict the enhanced erosion occurring on the top face of the solute. In fact, it can be noted that the predicted profile of the solid-liquid interface near the top edge of the solute in the model at time 5 s look identical to the experimental image. At 10 s, it can be seen that the entire fluid flow is directed upward above the solute towards the center. The colored temperature contours in the model match well with the dark blue region of fluid flow in the experimental image around the same region. The interface profile and the flow directions at that time frame show a good comparison. Also, at the vertical edge adjacent to solute, there are few velocity vectors which are directed downwards indicating the presence of thermal buoyancy in areas where thermal gradients are dominant over compositional differences. At 15 s, the tall velocity vectors can be seen for the fluid flow directed upward which matches with the experimental observation. From 15 s to 25 s, it can be seen that the velocity of the natural (free) convective flow due to thermal and compositional buoyancy forces in the bulk liquid away from the cold ethanol solute is much high with few of the velocity vectors directed upward while few downwards.

While in Case IV (**Figure 6.5**) in contrast to the Case II, the compositional Marangoni force at the top surface drives the fluid outward. Since ethanol is a low surface tension liquid, its increased

concentration at the interface with subsequent melting of the solid, decreases the surface tension of the fluid mixture at the interface, causing a flow directed outward from the low surface tension region (at the interface) to the high surface tension region (surrounding liquid). Thus although the two sets of surface tension driven forces (thermal and compositional) oppose one another, the compositional effects dominate. Preferential erosion of the solute at the solvent surface was negligible in contrast to the ice/water case. The interface at the top surface appears to expand as the ethanol dye is pulled outward. The model correctly predicts the dissolution process at the interface. At 10 s, the erosion of the material along the vertical face is highlighted in both the model prediction and the experiment in **Figure 6.5**. The interface profile at 20 s and 25 s looks very similar to the experiment. The total dissolution time in both experiment and model was observed to be the same (28 s) and provided the confidence in the results achieved.

In the results for both cases, the water solvent around the ethanol solute was observed to freeze between 3 s and 7 s (refer to the 5 s frames in **Figure 6.4** and **Figure 6.5**). The material properties of ethanol below the solidus which have been assumed were altered to correct this prediction. No significant change in the degree of freezing was obtained. Considering the large temperature difference between the initial temperature of the ethanol solute (88 K – blue region) and the water solvent (316 K – red region), it is expected and observed (however not measured) that the temperature of the water at the interface in the experiment decreased to the freezing point of water. In the video of the experiments, discrete frozen ice particles formed in proximity to the ethanol solute were observed to flow upward. One of those particles is visible in the 15 s frame in **Figure 6.5** and has been marked with a black-dotted circle.

Apart from this, the ethanol/water computational model has been able to display a good prediction of the development of the fluid flow vectors and interface profile with time.

Figure 6.2 Case I, B_T only, ice/water - completely dipped to the center: Comparison of solid/liquid interface and fluid flow pattern at every 10 seconds from the time of dipping

Note: The dotted region at 20 s surrounds the concave profile in both experiment and model. At 50 s, the dotted region surrounds the height/region over which the water from the melted ice has settled.
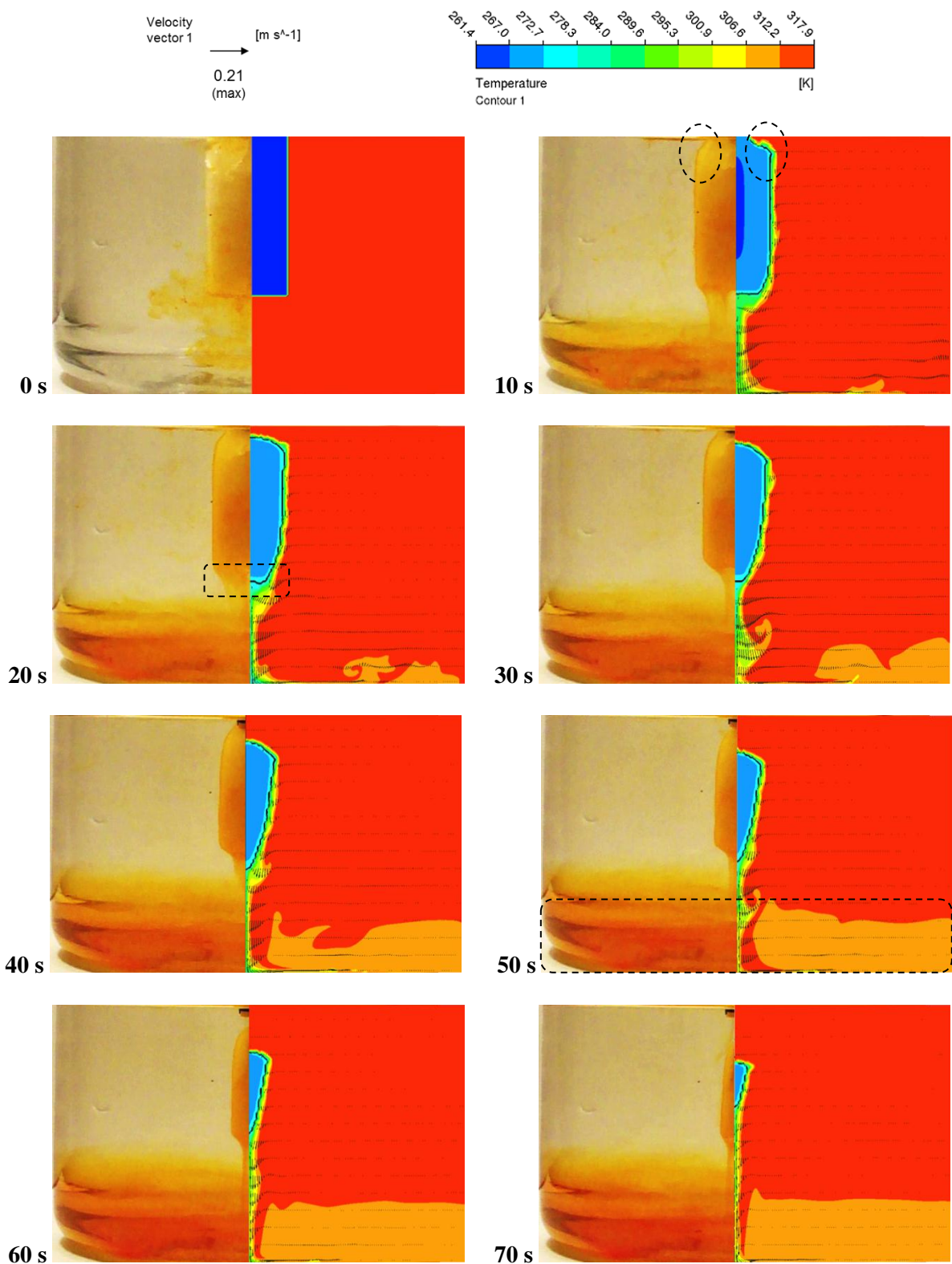
Figure 6.3 Case II, B_T and M_T, baseline, ice/water - from free surface: Comparison of solid/liquid interface and fluid flow pattern at every 10 seconds from the time of dipping

Note: The dotted region at 10s surrounds the erosion in the solute due to thermal Marangoni forces. At 20 s, the concave interface profile in the solute developed over time during dissolution can be observed. At 50 s, the dotted region surrounds the height/region over which the water from the melted ice has settled.
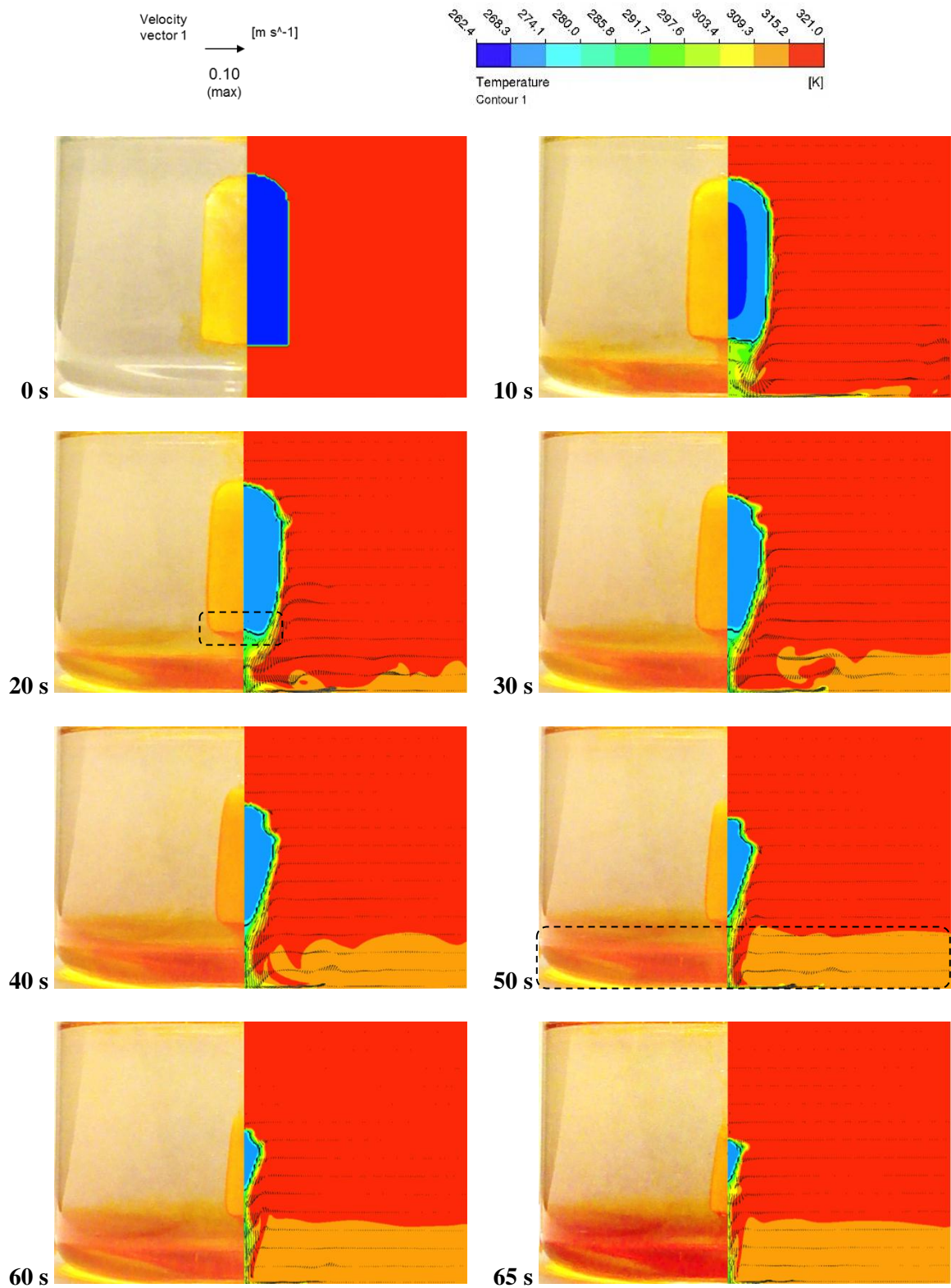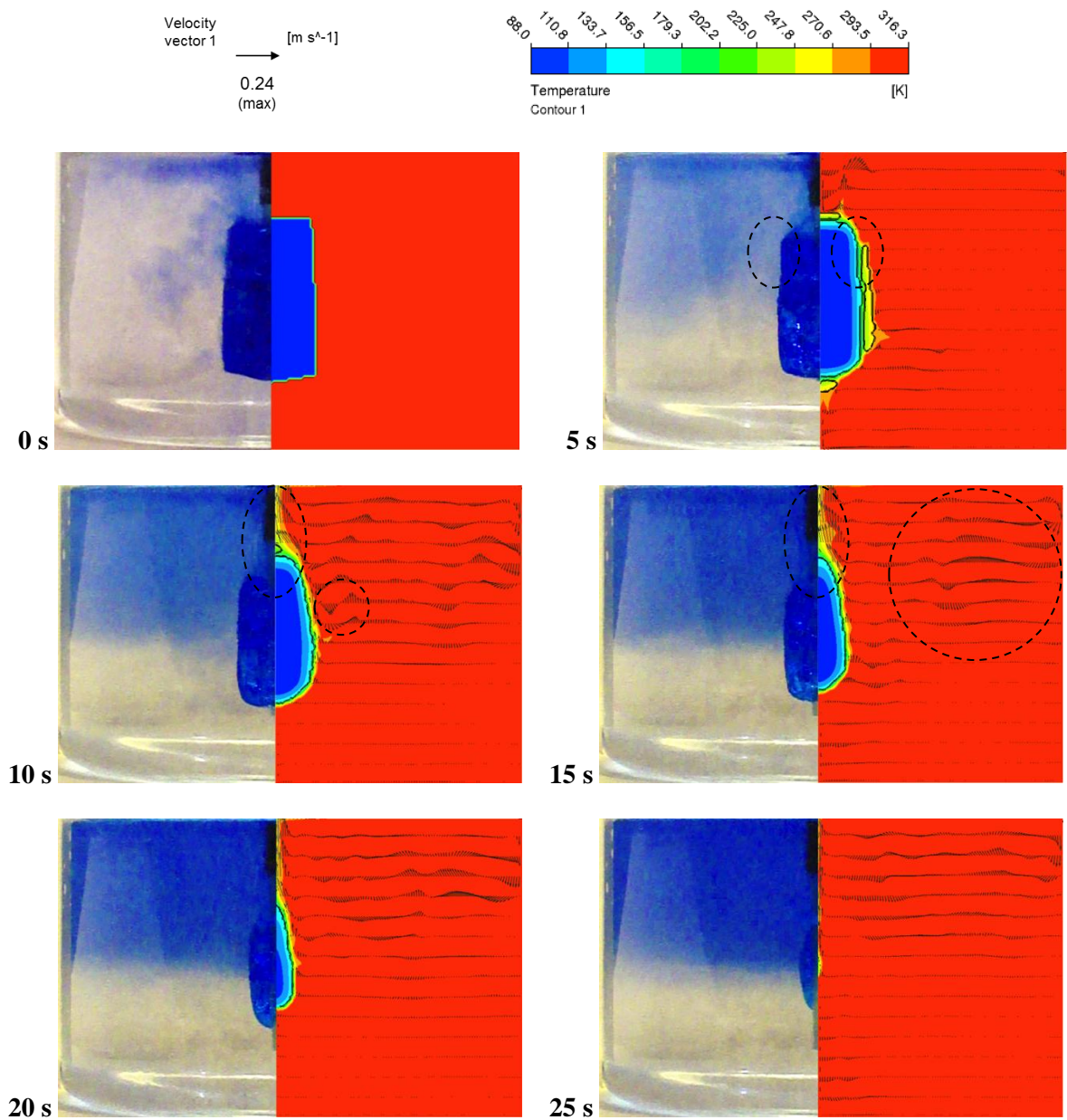
Figure 6.4 Case III, B_T and B_C, ethanol/water - completely dipped to the center: Comparison of solid/liquid interface and fluid flow pattern at every 5 seconds from the time of dipping

Note: At 5 s, the freezing region adjacent to the solute can be observed and the erosion of the ethanol solute due to compositional buoyancy can also be observed in region surrounded by dotted lines. At 10 s, the upward flow region in the experiment matches with the upward directed velocity vectors and temperature contours in the region highlighted with dotted lines. At 15 s, the dotted lines surround the presence of upward and downward directed flow vectors driven by compositional and thermal buoyancy forces, respectively.
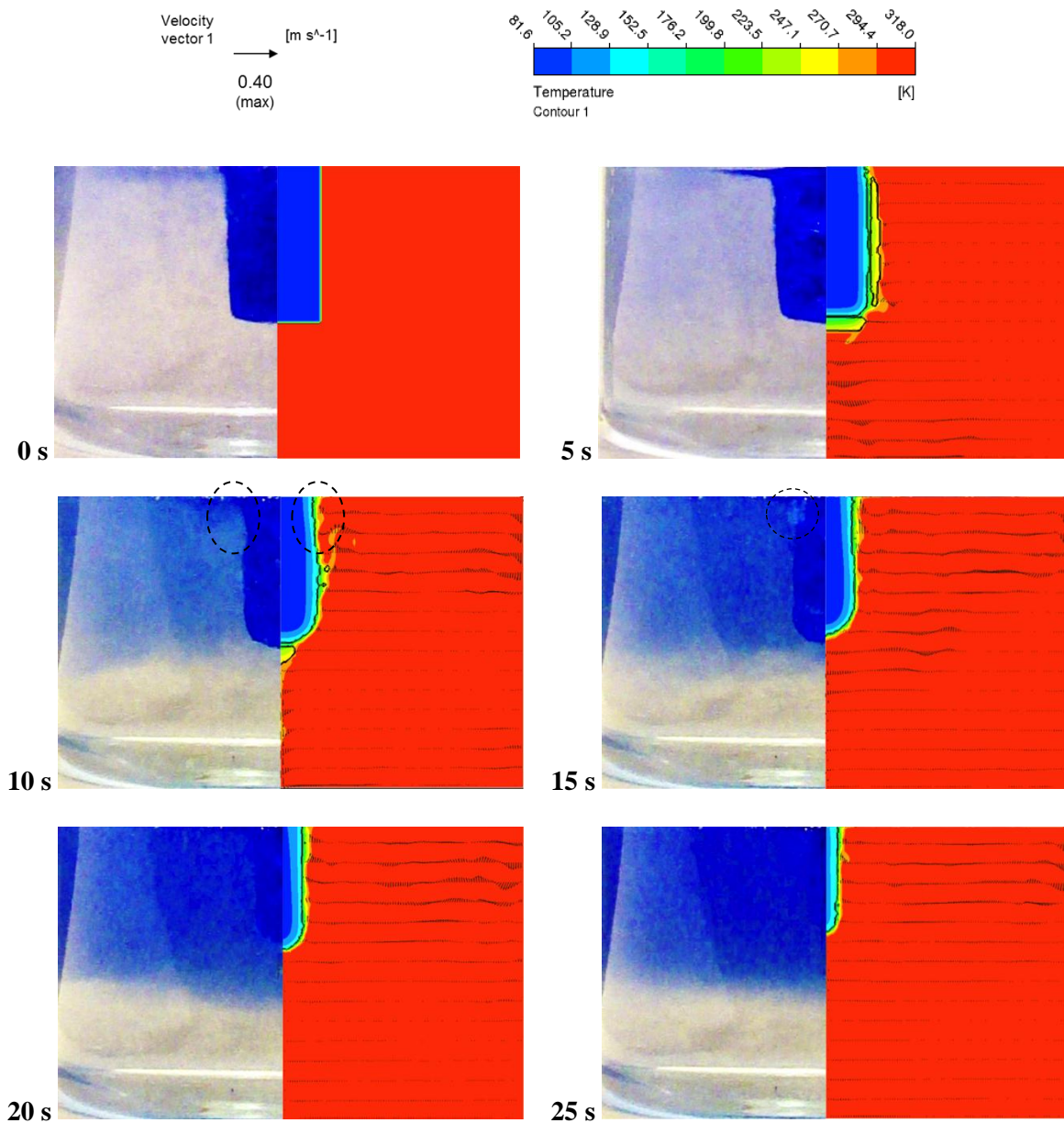
Figure 6.5 Case IV, B_T, B_C, M_T and M_C, ethanol/water - from surface: Comparison of solid/liquid interface and fluid flow pattern at every 5 seconds from the time of dipping.

Note: At 5 s, the freezing region adjacent to the solute can be observed. At 10 s, the erosion of the ethanol solute due to compositional buoyancy and Marangoni flow can be observed and is highlighted in the region surrounded by black dotted lines. At 15 s, a frozen ice particle that is floating upwards has been marked with black dotted lines.

6.1.2 Temperature Evolution

Ice/water: The temperature variation as a function of time measured by the two thermocouples (one in the solute and other in the solvent) is compared with the numerical predictions and presented in **Figure 6.6** for Cases I and Case II. In both the cases, the solute mould was warmed up close to 273 K to remove the ice from the mould. The solute was then cooled again to a temperature below 263 K, which was then adopted as the initial condition for the ice in the model.

In Case I, the solute was dipped with an initial temperature of 262.4 K into the water solvent bath maintained at 321 K. The time for complete dissolution in the experiment was observed to be ~72 s. The horizontal section of the solute temperature curve at 272 K represents the time range over which the latent heat is absorbed by the ice solute as it melt. After this, the system approaches equilibrium as the solute temperature and solvent temperature equalize. The temperature predictions for both ice solute and water solvent show excellent correlation with the measured temperatures. In the experiment, latent heat is absorbed at 272 K while in the model the temperature range over which this transformation takes place is assumed to be between 272 K and 278 K. The phase change temperature range is used to define the effective specific heat in the temperature range over which phase transformation occurs. Apart from the effective specific heat, the phase transformation also affects other material properties, like: viscosity, density and conductivity which are varied to account for the solid-to-liquid transformation. A 1 K temperature range i.e. between 275 K and 276 K is used to vary these properties. Increasing the temperature range over which these properties are varied has an effect on the dissolution time and will be discussed in Section 6.3, Sensitivity Study.

In Case II, the initial temperature in the model was based on the experimental temperature of 261.3 K. The temperature evolution predicted by the model for the ice solute correlates well with the experimental temperature measurements. The temperature range over which the material melts and latent heat is absorbed in the numerical analysis is from 272 K to 278 K, overlapping well with the experimental results for the same.

Comparing Case I with Case II, the main difference lies in the fact that in Case I, the surface area of solute exposed to the water solvent is higher than that in Case II and hence the total time of dissolution

for Case I is less than Case II despite the presence of additional convection in Case II caused by Marangoni forces.

Ethanol/water: For the ethanol/water cases shown in **Figure 6.7**, the initial condition applied in the model for the ethanol was 88 K and 81.6 K for Case III and Case IV respectively, consistent with the thermocouple data. The phase change phenomenon in the model was assumed to occur over a 15 K temperature range, from 150 K to 165 K during which the latent heat of melting is absorbed by ethanol. The other material properties were varied over 1 K, from 158 K to 159 K. The experimental and modeling results for the ethanol/water cases show continuous variation of temperature even during the ethanol phase transformation. This is due to the fact that the latent heat of melting of ethanol is 119 kJ/kg, which is three times lower than that of water (334 kJ/kg) and also because the ethanol starts at an initial temperature of ~88 K, far below its melting point of 159 K, and requires heating prior to the transformation. Comparing the ethanol/water results, the temperature in Case III shows a moderate increase in temperature between 0 and 25 s at which point the ethanol melts, while in Case IV, this increase in temperature is very slow until 15 s beyond which the increase is gradual from ~22 s to ~27 s.

The model prediction for Case III in comparison to its experimental results does not show a good agreement. In fact, the model prediction in Case III looks similar to that of the Case IV but not the experimental prediction. In ice/water cases, the experimental measurements and model predictions for Case I and Case II look similar unlike in ethanol/water case. Several trials on experimental measurements were performed for Case III and all the trials showed similar temperature evolution curves for the ethanol solute. However, Case IV shows a relatively good match with the experimental measurements.

The reason for the thermal behavior exhibited in Case III is unknown. It was initially thought that the rapid temperature increase may be due to increased heat conduction along the wooden stick that is in contact with the solvent above the cold ethanol solute. An alternate model including the stick geometry in the domain (1.5 mm in thickness and 46.5 mm in length) and its thermo-physical properties from [87] was developed. With a mesh size of 0.5 mm (3 mesh cells of wood), time steps equal to 0.01 s and the viscosity of wood being 20 Pa-s, the model predicted movement of the solid wood. When the mesh size and time step were decreased to 0.25 mm (6 mesh cells of wood) and 0.005 s, respectively, and the

viscosity of wood was increased to 1000 Pa-s, the movement of the wood during the dissolution event was eliminated. As noted during the experiment trials with different materials (copper, wood and ceramic) used to support the solute, no change in behavior was observed as shown in **Figure 6.8**.
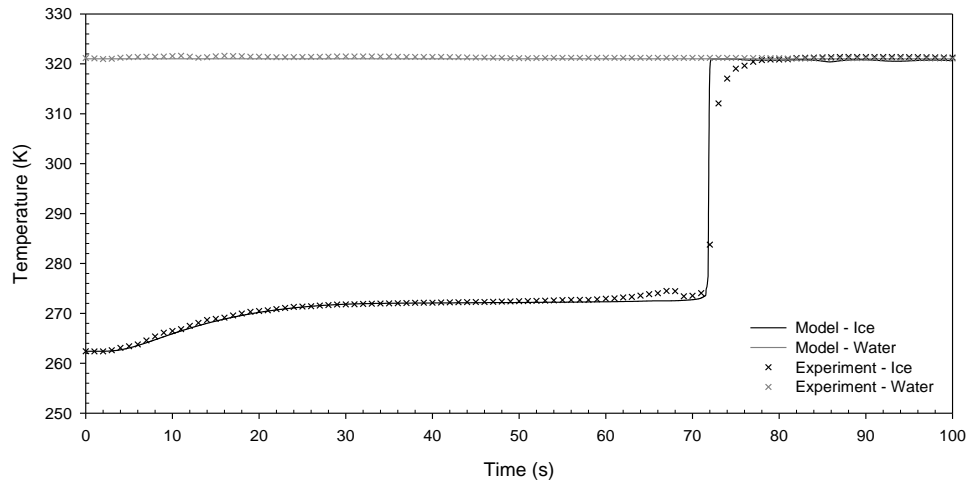
(a) Case I, B_T only (completely dipped to the center)
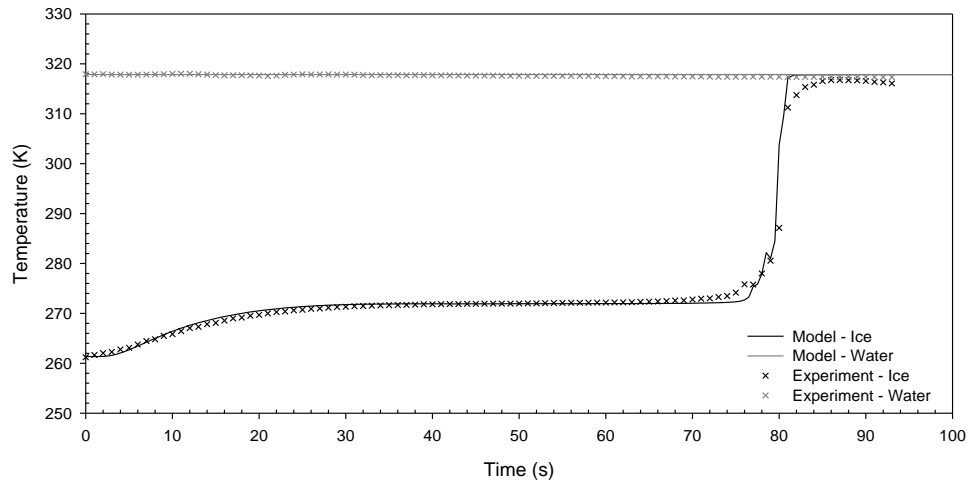
(b) Case II, B_T and M_T, baseline (from free surface)

Figure 6.6 Ice/water: Temperature comparison between experimental data and model prediction
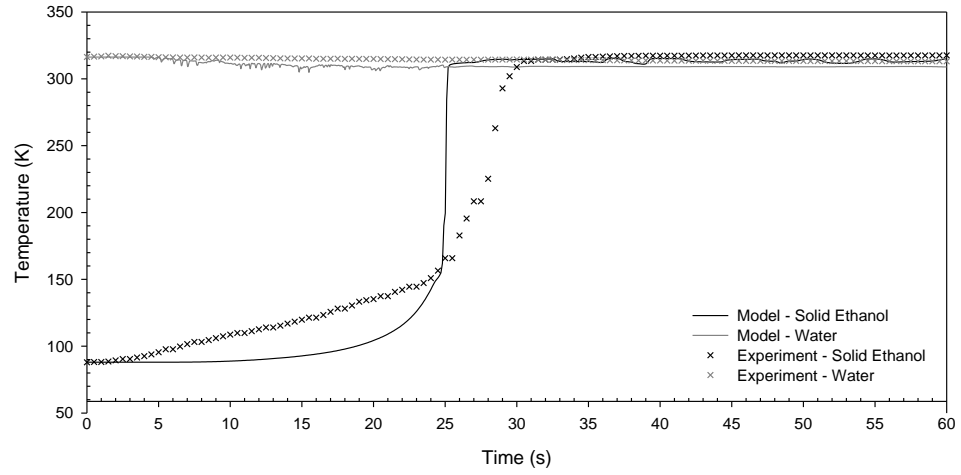
(a) Case III, B_T and B_C (completely dipped to the center)
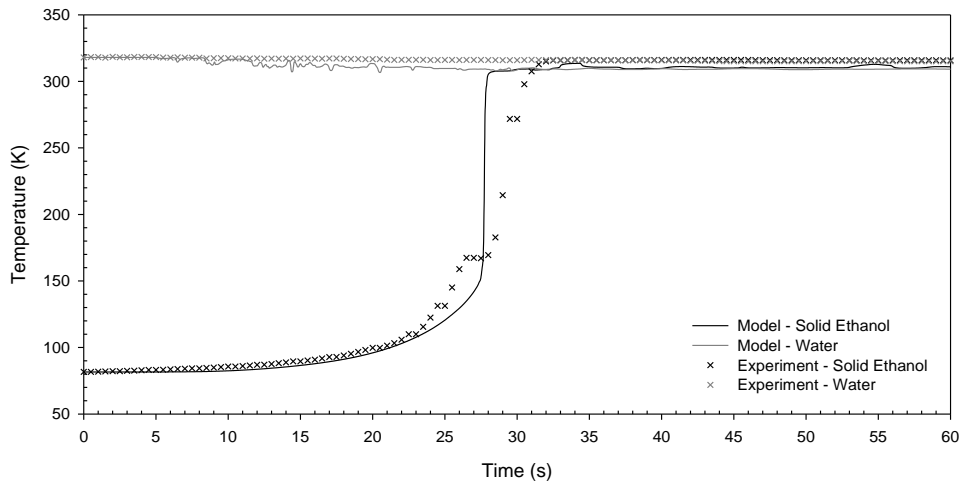
(b) Case IV, B_T, B_C, M_T and M_C (from free surface)

Figure 6.7 Ethanol/water: Temperature comparison between experimental data and model prediction
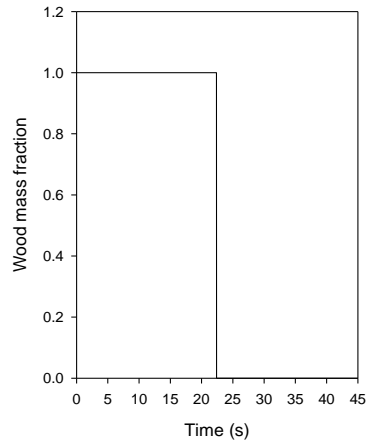
(a) Change in mass fraction of wood with time

(b) Schematic representation of the thermocouple location (experiment) and monitor points (model) in the cell/domain
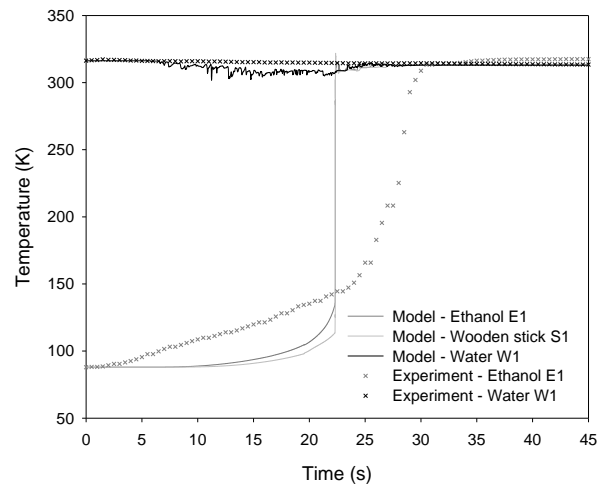
(c) Comparison of the temperature evolution curve between the experimental data and numerical data obtained for wood (stick material), ethanol (solute) and water (solvent)

Figure 6.8 Case III, B_T and B_C, ethanol/water with wooden stick addition in the domain - completely dipped to the center

6.1.3   Interface Profile

Ice/water: The dissolution versus time was quantified by characterizing changes in the solid solute radius at the mid-height. Measurements were performed for both the experimental and numerical results at 5 s intervals. The results for Cases I and II are shown in **Figure 6.9**. For the experimental data, the presence of dye in the solute helped delineate the solid-liquid interface. The maximum difference is 0.98 mm dia. at 40 s in Case I and 1.18 mm at 70 s in Case II. In spite of these small differences, the experimental measurements and the model results show satisfactory agreement for both the cases. Thus indicating that overall the model is able to correctly predict the dissolution process for thermally-driven conditions.

Ethanol/water: **Figure 6.10** shows a comparison of the diameter measurements of the ethanol solute at mid-height for both the experimental and model predictions, measured at 2.5 s intervals. In both the cases, the results show adequate comparison between the experimental and numerical results. In Case III, the maximum difference between the experimental and model results is 2 mm at 25 s. The model predictions deviate from the experimental measurements during the initial 10 s because of the layer of solvent that freezes around the solute between 2.5 s to 7.5 s. The momentum and mass transfer across the interface is restricted during this time and therefore the model predicts a gentle slope in comparison to steeper slope observed in the experiment. The results for Case IV show adequate agreement. The maximum deviation occurs at 10 s where a difference of approximately 1.44 mm is observed. The large deviation at 10 s occurs because of enhanced solute dissolution in the experiment caused by the interface. The release of gas bubbles from the ethanol solute during the experiment caused enhanced material loss from the solute in a few instances. The change in diameter of the ethanol solute between 7.5 s and 10 s was ~2.3 mm in comparison to ~1 mm for the previous 2.5 s time period and ~0.7 mm for the next 2.5 s time period.

**Figure 6.9 Ice/water: Diameter measurement of the solute (at mid) with time, (a) Case I, B_T only (completely dipped to the center); (b) Case II, B_T and M_T, baseline (from free surface)**

Figure 6.10 Ethanol/water: Diameter measurement of the solute (at mid) with time, (a) Case III, B_T and B_C (completely dipped to the center); (b) Case IV, B_T, B_C, M_T and M_C (from free surface)
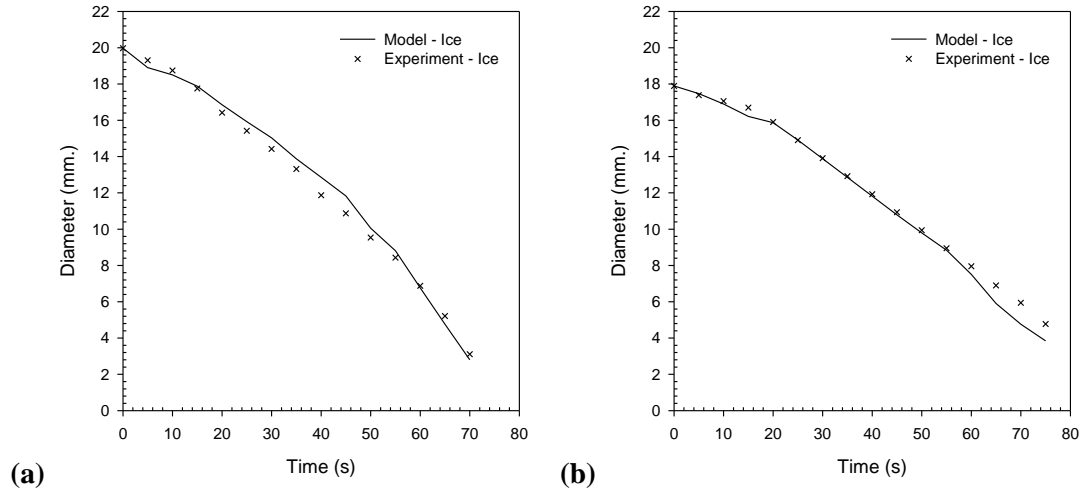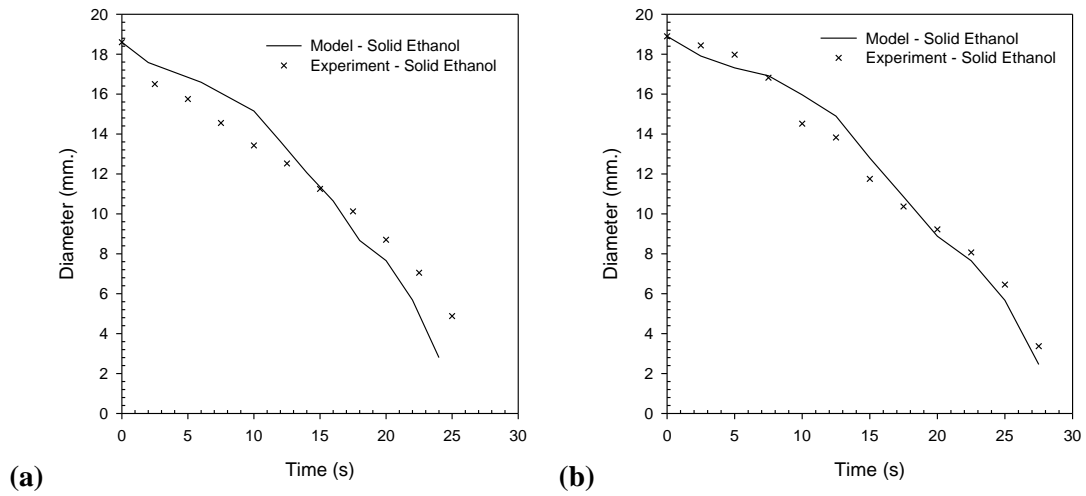
6.2 Experimental Repeatability

The repeatability of the experimental procedure was studied by performing a series of the same dip tests for both ice/water and ethanol/water systems. Each test was conducted by partially dipping the solute in the solvent (i.e. Case II and IV). Three trials were conducted for each system with similar starting temperatures for both the solute and the solvent. The experiments were conducted based on the experimental procedure described in Chapter 4, section 4.2.

Ice/water: The starting temperature of the solute was ~260.9 ± 0.2 K and the solvent temperature was ~318.4 ± 0.7 K. The temperature curves for the three trials (W1, W2 and W3) shown in **Figure 6.11 (a)** overlap between 0 and 75 s and the dissolution time for all three trials is 77 ± 2 s. Thus, there is excellent repeatability for this system. The variation of solute diameter is shown in **Figure 6.11 (b)** for the same trials. Overall the slope of the diameter curves versus time is the same for each trial. The initial diameter of the solute at time 0 s was observed to vary for each trial because of the variability in the extraction during the removal of the sample from the mould. These three trials demonstrate good repeatability both in terms of temperature evolution and diameter variation.

Ethanol/water: The ethanol was dipped with a starting temperature of 81.1 ± 0.5 K with a water solvent temperature of 317.5 ± 0.6 K. The temperature evolution curves for the three ethanol/water system trials (E1, E2 and E3) is shown in **Figure 6.12 (a)** exhibit invariability. The total dissolution time varies between 22 s and 29 s. Overall the repeatability of the ethanol/water is satisfactory in **Figure 6.12 (b)**, the initial diameter of the ethanol solute for the three trials is similar with the smallest being 17.64 mm and largest being 18.22 mm. Although the variability is greater than that shown in the ice/water system, the slope of the curve for all three trials is nearly identical and it can be said that this system ensures good repeatability.
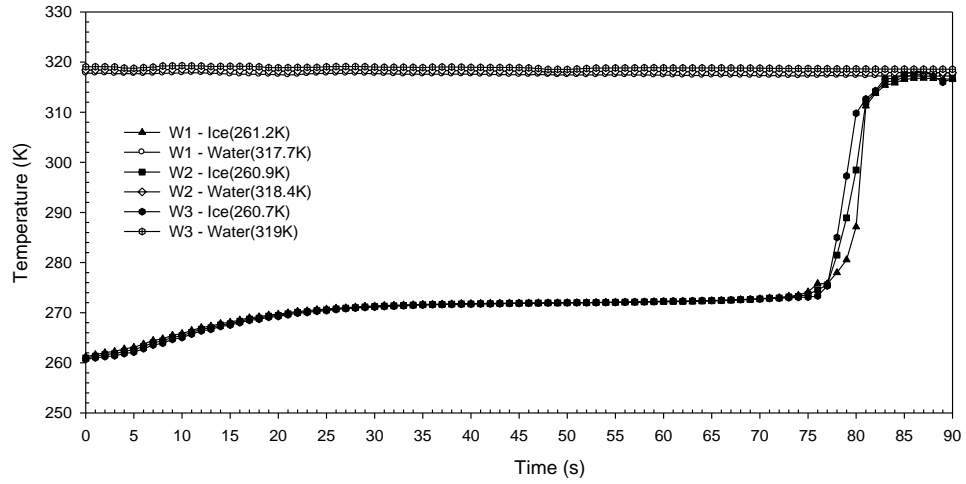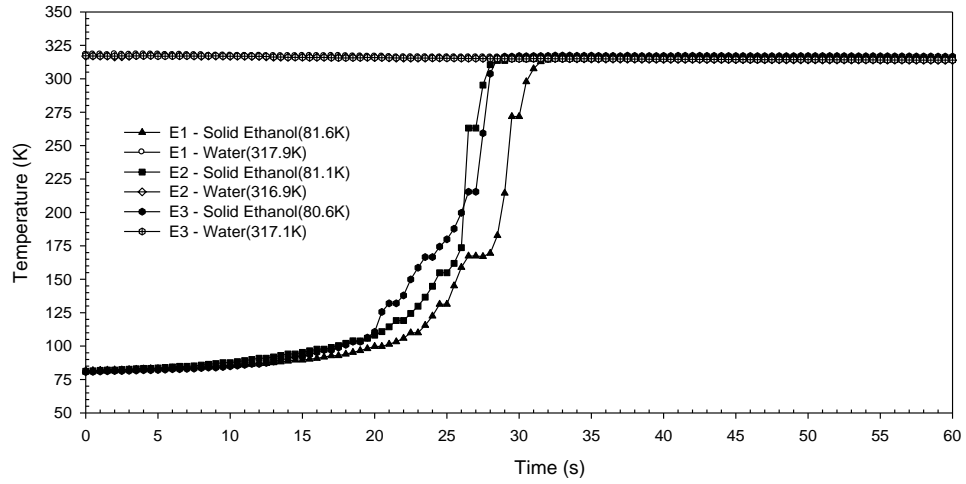
(a) Temperature evolution curve
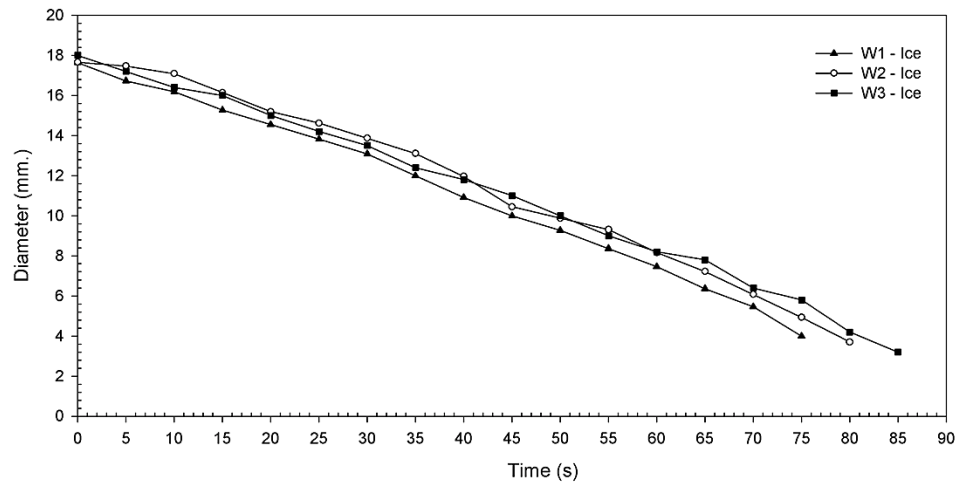
(b) Solid-liquid interface profile

Figure 6.11 Repeatability study on ice/water (Case II, baseline)

(a) Temperature evolution curve
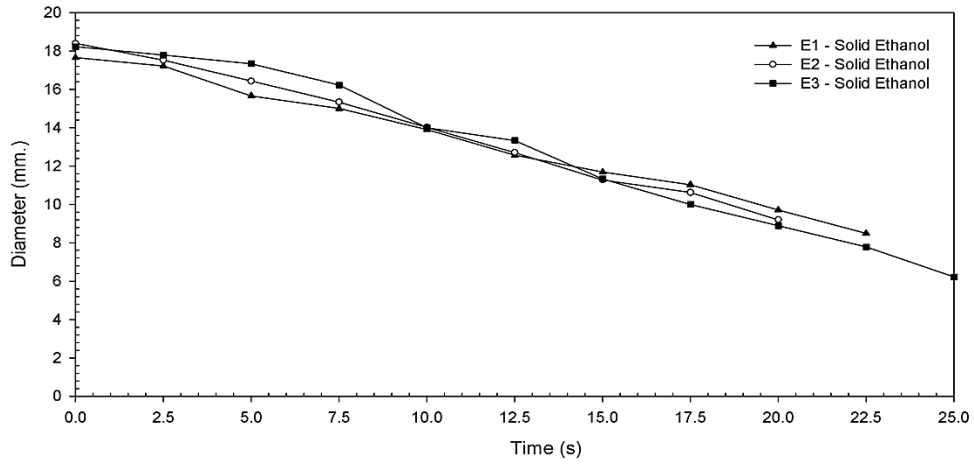
(b) Solid-liquid interface profile

Figure 6.12 Repeatability study on ethanol/water (Case IV)

6.3   Sensitivity Study

A sensitivity analysis was performed with the physical analogue model and the numerical model of the ethanol-water and ice-water systems. The objective is: a) to assess the impact of changing experimental variables; b) to assess the methods used to describe certain phenomena like, Marangoni, and c) to evaluate certain critical model and numerical parameters used in model formulation. **Table 6.1** summarizes the factors that were assessed.

Table 6.1 Summary of the factors investigated in the sensitivity analysis

Type		Factors investigated	Baseline	Variations
Experimental		Dipping temperature	268.1 K	265.6 K, 260.7 K
		Marangoni forces	With Marangoni	Without Marangoni
Model	*Numerical*	Mesh size	0.5 mm	0.25 mm, 1 mm, 1.5mm
		Time step	0.01 s	0.005 s, 0.02 s
	Process Parameter	Solidus Temperature	272 K – 277 K	270 K – 275 K, 274 K – 279 K
		Temperature range over which latent heat is absorbed	272 K – 277 K	272 K – 275 K, 272 K – 276 K, 272 K – 278 K, 272 K – 279 K
		Temperature range over which material properties are varied	1 K	0.5 K, 2 K, 3 K, 5 K

6.3.1   Experimental Sensitivity

6.3.1.1 Dipping Temperature for Ice/Water

The temperature results of three ice/water experiments with different initial ice temperatures are shown in **Figure 6.13**. While conducting the ice/water experiments, it was observed that when ice with a low temperature (i.e. 260.7 K) was dipped into water with a temperature of ~319 K (refer to T1 in **Figure 6.13**), the melting time was ~77 s. When ice with a higher temperature was dipped into water with approximately the same temperature as the first experiment, the overall dissolution time increased, ~78 s

and ~82 s, for T2 and T3 respectively. The specific heat of water increases with increasing temperature [76] as shown in **Figure 5.4.** Considering thermal energy, ice samples of identical size with initial temperatures below the solidus will require increasing amounts of thermal energy to reach the same equilibrium temperature as their initial temperature decreases. For similar heat transfer conditions, longer melting times would be expected for samples requiring increasing amounts of thermal energy. Interestingly, the opposite trend has been observed where ice solute starting at a lower temperature melts faster. This may be due to differences in the heat transfer conditions caused by enhanced fluid flow. In general, it has been observed that warm water freezes faster than cold water, although the reason for this is still not clear (Mpemba effect) [88] . The present work is focused on understanding the effect of fluid flow during the dissolution of alloying elements and therefore, no further work has been done to develop a more thorough understanding of these results.
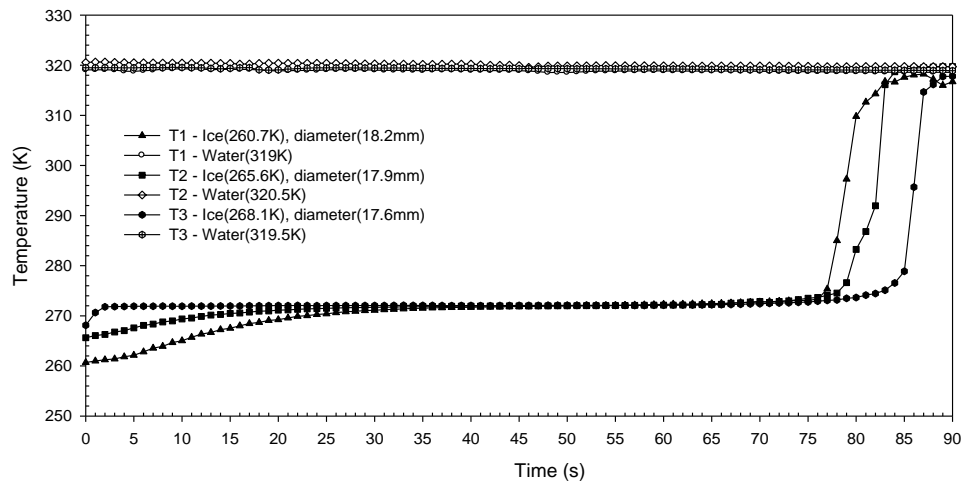
Figure 6.13 Effect of the dipping temperature on the dissolution time for ice/water

6.3.1.2 Marangoni Forces

Since it was not possible to quantify the change in surface tension (or, surface tension coefficient) on the top surface experimentally, the results for different experiment conditions were compared (i.e. Case I with Case II and Case III with Case IV) to assess the influence and impact of Marangoni force at the surface on the dissolution of both ice/water and ethanol/water system. This analysis was performed by

measuring the rate of change of solid-liquid interface diameter for both ice and solid ethanol at the top surface. The results are shown in **Figure 6.14 (a)** and **(b)** for the ice/water and ethanol/water cases, respectively. The qualitative comparison of picture frames at specific times during the experiment for both the cases is shown in **Figure 6.15 (a)** and **(b)** for ice/water and ethanol/water cases, respectively.

Figure 6.14 (a) shows that for ice, the rate of change of diameter during the 'partially dipped' experiment is faster than that of the 'fully dipped' experiment from 0 s to 25 s. This indicates that the ice erodes faster at the water surface. This can also be verified visually by examining the length of the black line marked in **Figure 6.15 (a)**, where the left hand side (L.H.S.) image shows the 'partially dipped' experiment and the right hand side (R.H.S.) image shows the 'fully dipped' experiment.

Figure 6.14 (b) and **Figure 6.15 (b)** shows the influence of the compositional Marangoni forces in the ethanol/water case. Initially the ethanol-water interface moves outward at the top surface of the water as shown in 'partially dipped' case image at 2.5 s. After expanding the interface diameter begins to decrease as the dissolution progresses. The meniscus can be seen to be spread outward along the top surface of the water. At the same time, for the fully dipped case (R.H.S. of **Figure 6.15 (b)** frames) few measurements could be made because the ethanol melts very quickly when completely dipped in water ('dotted while line' at 5 s and 7.5 s indicates absence of ethanol solute). It can be clearly observed from the frames that the effect of Marangoni force in the 'fully dipped' is absent at the solute interface.

(a)   (b)

Figure 6.14 Effect of Marangoni forces for 'partially dipped' and 'fully dipped' experiments for ice/water and ethanol/water: (a) Comparison of change in solid-liquid interface diameter for ice/water; (b) Comparison of change in solid-liquid interface diameter for ethanol/water

(a) Comparison of the experimental frames taken at every 5s for ice/water cases

(b) Comparison of the experimental frames taken at every 2.5s for ethanol/water cases

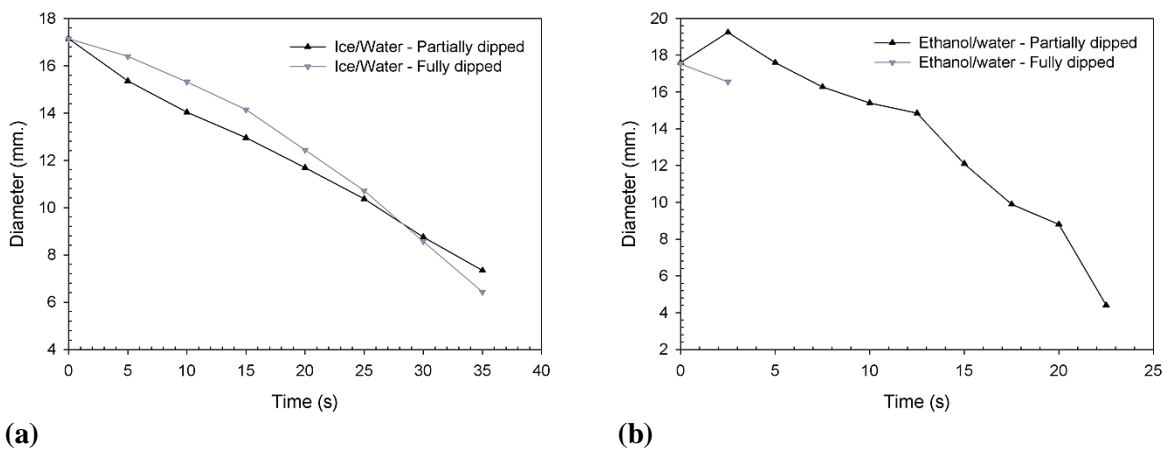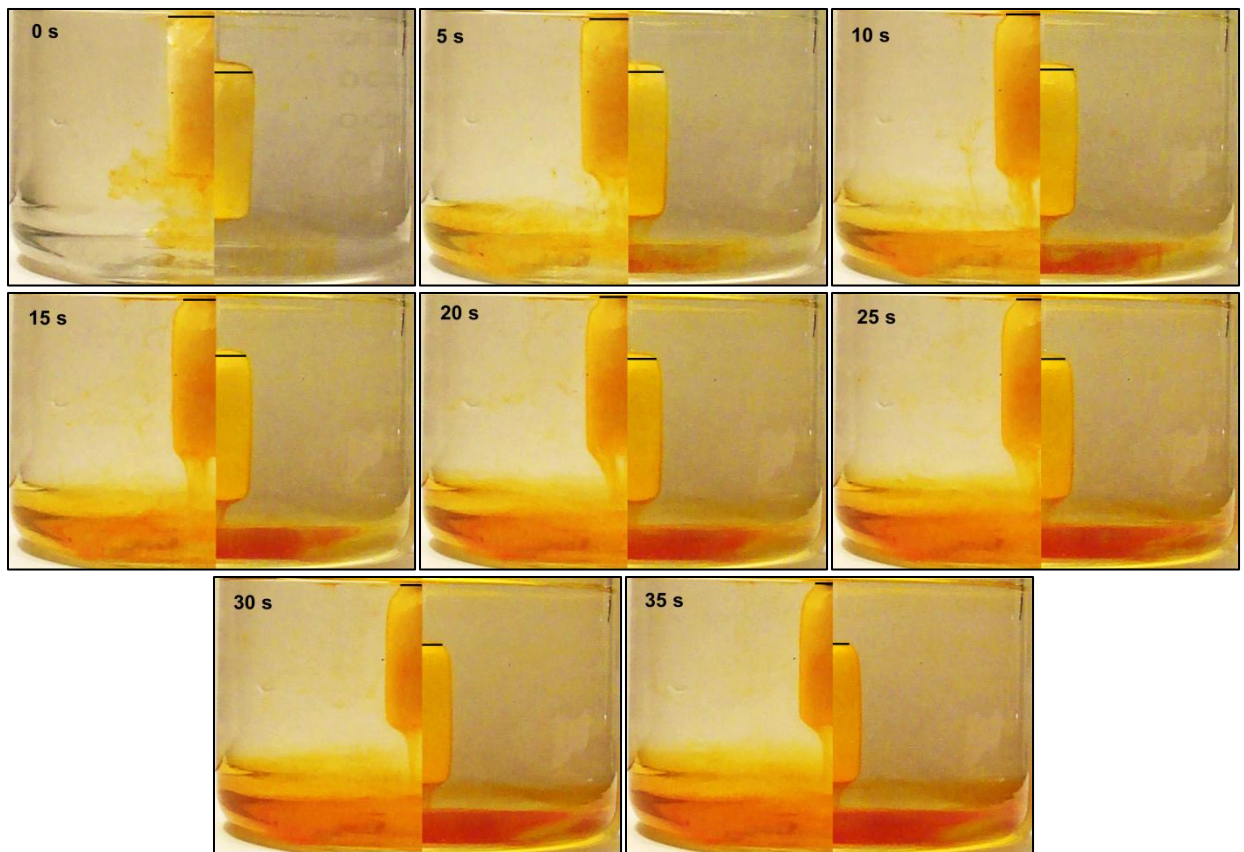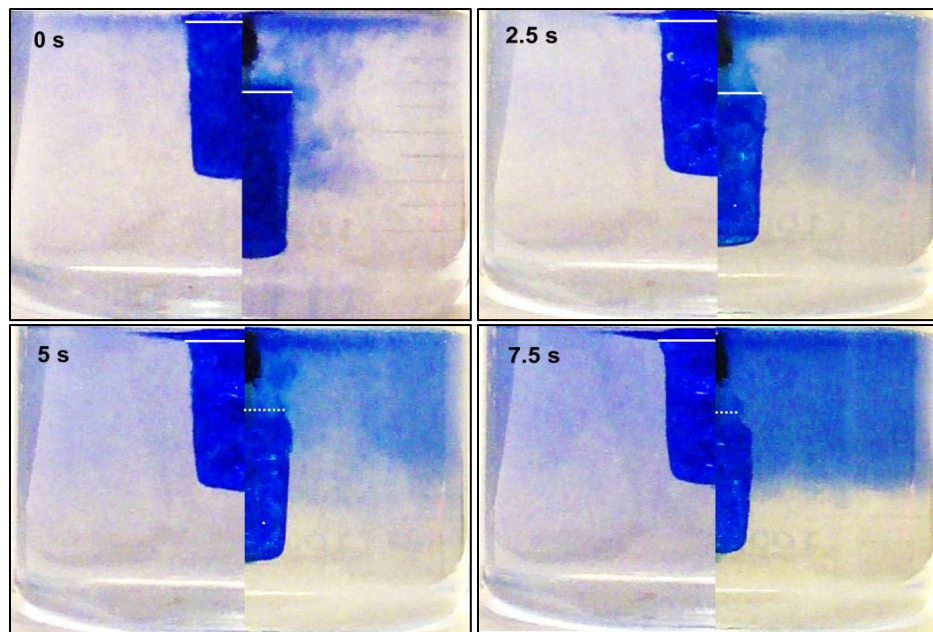**Figure 6.15 Effect of Marangoni forces for 'partially dipped' and 'fully dipped' experiments for ice/water and ethanol/water**

6.3.2 Model Sensitivity

The sensitivity of the numerical model was assessed to determine the impact of critical numerical and process parameters used in the dissolution model. The ice/water system (Case II) with effects of thermal buoyancy and Marangoni (B_T and M_T) was used as the base-case for the model sensitivity study. The starting temperature and resulting dissolution time of the base-case were 268 K and 82 s, respectively.

6.3.2.1 Numerical Parameters

The sensitivity of the model to the variations in numerical parameters like: mesh size and time step has been assessed.

6.3.2.1.1 Mesh

The effect of mesh size was assessed by comparing the computation time, temperature evolution curves and temperature contours plots for model geometries with mesh sizes ranging from coarse to fine. The mesh size for the baseline model was 0.5 mm. The baseline mesh size was increased by a factor of 2 and 3, as well as decreased by a factor of 2 to obtain mesh sizes of 1 mm, 1.5 mm and 0.25 mm, respectively. The domain for each mesh was meshed with hexahedral elements. The time step for the cases with increased mesh size was unchanged from the baseline value of 0.01 s. However, running the 0.25 mm mesh with 0.01 s (baseline value) and 0.005 s time steps resulted in significant numerical instability and poor convergence. Convergence is dependent on both spatial (related to mesh size) and temporal (related to time step selected) factors. In general, as mesh size decreases, smaller time steps are required to prevent numerical instability. The 0.25 mm mesh case was modeled with 0.001 s time step to reduce instabilities and improve convergence at the expense of computation time. **Table 6.2** summarizes the mesh statistics and the respective computation time.

Table 6.2 Mesh and computation data

	Finer: 0.25 mm	*Fine: 0.5 mm*	*Medium: 1 mm*	*Coarse: 1.5 mm*
Number of Nodes	95520	23760	5880	2640
Number of hexahedron elements	47322	11662	2832	1248
Computation time (hours)	>250	~25	~9	~4

Figure 6.16 compares the temperature variation at the mid-point of the solute for each mesh size case. The predicted temperature is sensitive to the mesh size selected. The case with a 0.25 mm mesh size results in a dissolution time of ~79 s, which is comparatively close to the baseline case (~82 s). On the other hand, the 1 mm and 1.5 mm mesh size cases result in melting times of ~97 s and ~109 s, respectively. The selection of a coarser mesh appears to have a greater effect on the melting time compared to the finer mesh size models. **Figure 6.17** shows the effect of mesh size on the temperature distribution evaluated at 10 s. The features exhibited in the temperature distribution of the 1 mm and 1.5 mm mesh size cases are similar to the baseline 0.5 mm mesh size case. However, both the 1.5 mm and the 1 mm mesh size cases failed exhibit the effects of Marangoni forces on the top surface of the solute which the baseline 0.5 mm mesh size case predicted appropriately. In contrast, the 0.25 mm (finer mesh) showed less variation/sensitivity in terms of solid-liquid interface behavior, temperature distribution in comparison to the 0.5 mm (fine mesh) baseline case. The 0.25 mm mesh size case showed a slightly larger effect of Marangoni forces on the top surface through increased erosion and the solid-liquid interface appears to be much smoother compared to the baseline case. However, considering the flow features that were resolvable and the overall accuracy of the predictions using 0.5 mm mesh size along with the ten-fold decrease in computation time in comparison to 0.25 mm mesh size, it was determined that the 0.5 mm mesh is a reasonable compromise.
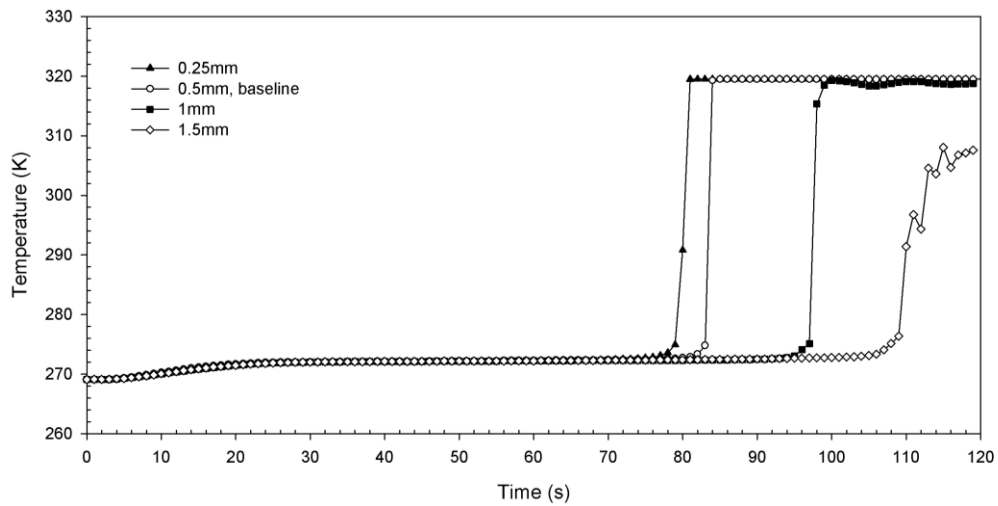
Figure 6.16 Comparison of the dissolution time for ice/water case with four mesh sizes 0.25 mm, 0.5 mm, 1 mm, 1.5 mm

84

0.25 mm mesh at 10 s   **0.5 mm mesh at 10 s**   **1 mm mesh at 10 s**

1.5 mm mesh at 10 s

Figure 6.17 Thermal and velocity distribution on the symmetry plane for cases modeled with 0.25 mm, 0.5 mm, 1 mm and 1.5 mm mesh at 10 s

6.3.2.1.2 Time step

To determine the effect of the time step size on the model predictions, three different time steps (t_s = 0.005 s, 0.01 s (baseline) and 0.02 s) were evaluated using the model. The time step size has a direct influence on the convergence of the numerical solution for this transient problem. **Figure 6.18** shows the temperature evolution at the center of the solute during dissolution for the ice/water case. The temperatures predicted with time step sizes of 0.005 s and 0.01 s coincide with each other up to 82 s. Also, the temperature distributions evaluated at 10 s for these two time step sizes, shown in **Figure 6.19**, are almost identical. Differences in velocity predictions may be observed in **Figure 6.19**. In contrast, the temperature evolution for the 0.02 s time step case indicates a dissolution time of ~36 s which is ~46 s

less than 0.01 s time step case indicating a substantial decrease in the dissolution time. The temperature distribution for the 0.02 s time step case at 10 s shows instabilities in the flow vectors along the solid-liquid interface. Based on these results, it was determined that 0.02 s is too large a time step for this dissolution model as it introduces considerable error and instability in the results whereas a smaller time step size (0.005 s) showed negligible difference in the final results.

Figure 6.18 Comparison of the dissolution time for ice/water case with three time steps 0.005 s, 0.01 s and 0.02 s

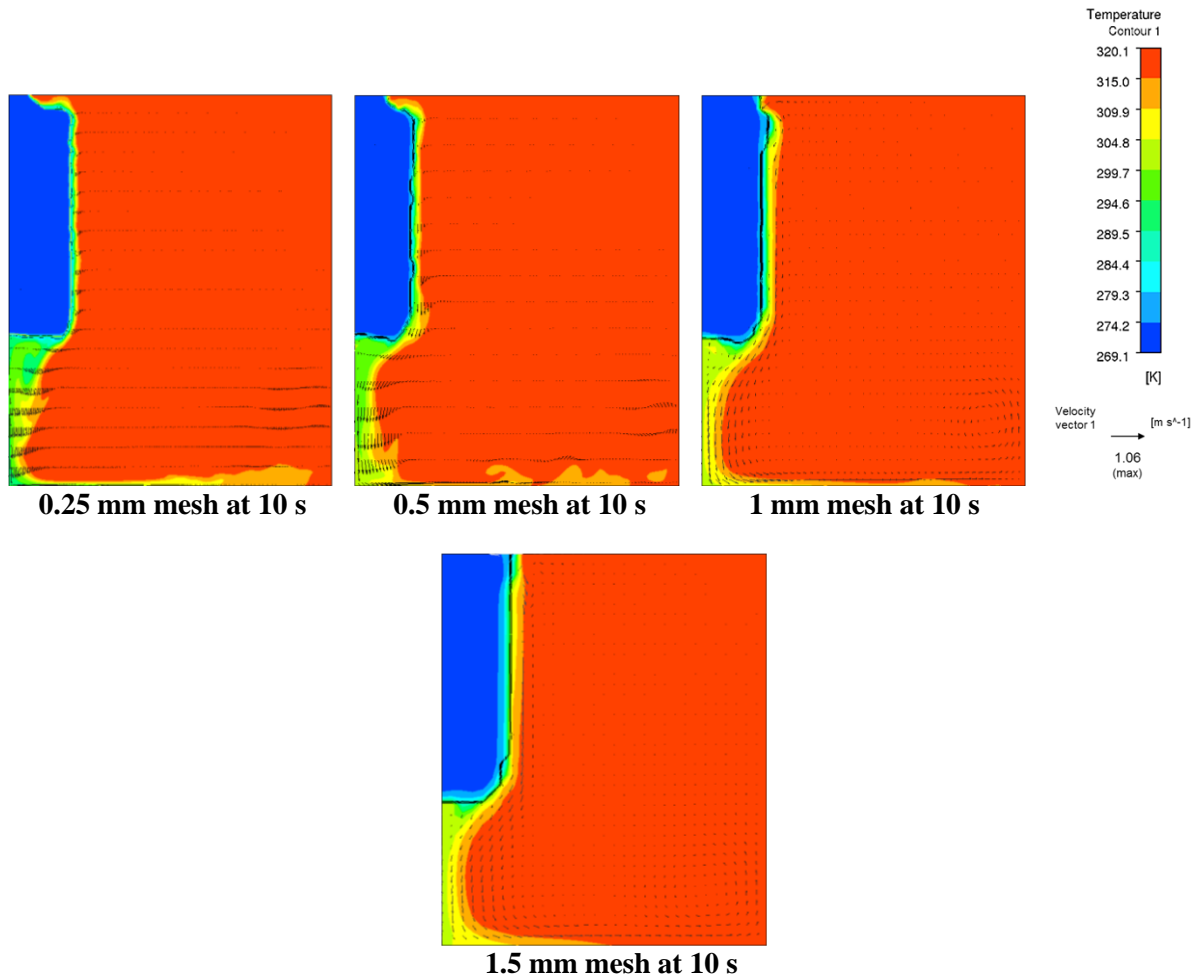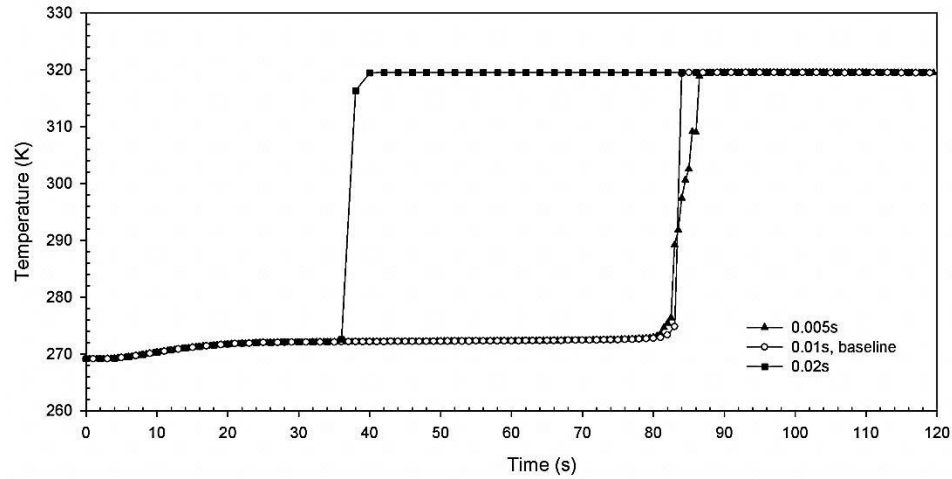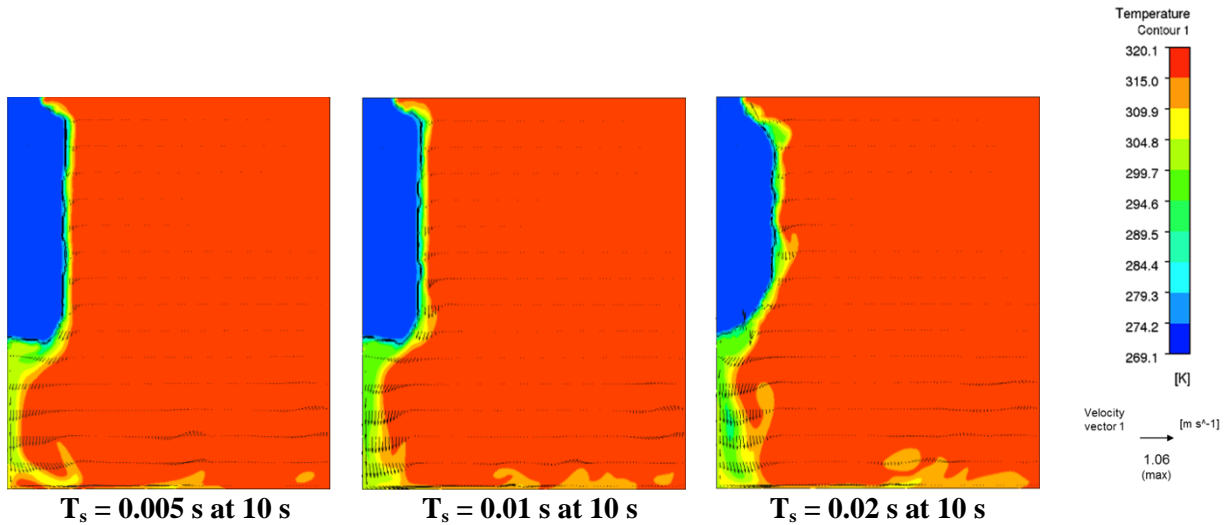| $T_s = 0.005$ s at 10 s | $T_s = 0.01$ s at 10 s | $T_s = 0.02$ s at 10 s |

Figure 6.19 Thermal and velocity distribution on the symmetry plane for cases modeled with 0.005 s, 0.01 s and 0.02 s time step at 10 s

6.3.2.2 Process Parameters

In addition to studying how the numerical parameters of the model affected the result, the process parameters affect the heat, mass and fluid (momentum) transport during the dissolution process was investigated. Changes to three process parameters were evaluated based on their effect on the interface behavior, dissolution time and temperature evolution in the solute. In this study, based on the particular parameter under study like, specific heat, the other coinciding and related parameters like, density, viscosity, conductivity, etc. were changed as well to suit the physics of the problem.

6.3.2.2.1 Solidus Temperature

The temperature evolution at the center of the solute during dissolution of a cold solute in a hot solvent exhibits characteristic features that have been discussed previously. Two important characteristics of the curve are: a) the temperature at which the solid solute begins to melt and, b) the temperature range over which melting of the solute occurs. In the model, this information defines the range over which the specific heat data is modified to account for the phase transformation to occur. The temperature evolution at the center of the solute predicted for different solidus temperature (270 K; 272 K (baseline) and 274 K) is shown in **Figure 6.20.** Here, the latent heat absorption range (added as a material property in effective specific heat) for all the cases was for 5 K temperature range. 'CpE(270K)_MP(1K)' indicates that the latent heat absorption temperature range starts at 270 K, finished at 275 K and the relative material properties, MP (viscosity, liquid fraction, conductivity and density) were varied over 1 K temperature range from 274 K to 275 K. Similarly for 'CpE(272K)_MP(1K)', melting starts at 272 K, finishes at 277 K and MP vary accordingly.

The results indicate that changing the solidus temperature shifts the temperature plateau associated with melting. For 'CpE(270K)_MP(1K)', the phase transformation initiates at 270 K (i.e. start of the region of constant temperature zone) and the total dissolution time was observed to be ~78 s which is ~4 s less than the baseline model. In contrast for 'CpE(274K)_MP(1K)' case, the total dissolution time was observed to be ~89 s which is ~7 s more than the baseline model 'CpE(272K)_MP(1K)'. Thus increasing the solidus temperature leads to an increase in the dissolution time despite maintaining the same melting temperature range. The experiments performed indicated that the phase change occurred at

87

~272 K in ice. Hence 272 K was chosen as the starting temperature of the CpE temperature range for the modeling work conducted related to ice/water case.
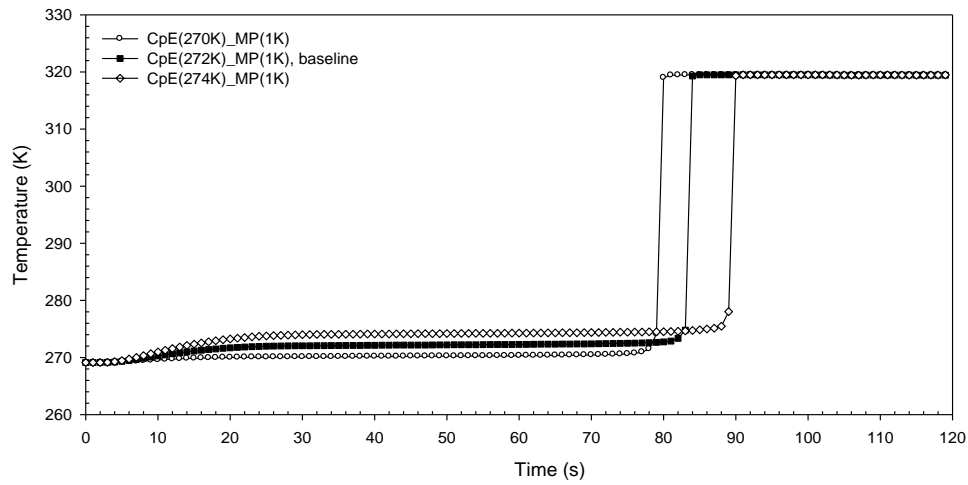
Figure 6.20 Effect of the solidus temperature on the dissolution kinetics

6.3.2.2.2 Melting Temperature Range

In addition to the solidus temperature, it is expected that the temperature range over which melting occurs will affect the overall dissolution time. It is known that pure water and ethanol exhibit specific melting points, in other words the phase transformation in these liquids occurs at a temperature. Requiring the absorption of latent heat over a narrow temperature range, such as 1 K, causes numerical instabilities in the CFX model. Thus, both water and ethanol were assumed to melt over a temperature range of a few degrees. The temperature range, i.e. 3 K, 4 K and so on, affects the duration of the phase change process.

The temperature predictions for the cases of ice melting using different temperature ranges to define the effective specific heat (CpE): 3 K, 4 K, 5 K (baseline), 6 K and 7 K, are shown in **Figure 6.21**. For latent heat absorption over 3 K range, the total dissolution time was ~10 s which highlights the numerical instability for cases with CpE varying over small temperature ranges. For CpE temperature ranges of 4 K, 5 K (baseline), 6 K and 7 K, the dissolution time was observed to be approximately the same (82 s). This suggests 3 K is the critical CpE window range beyond which any bigger CpE window

predicts a similar dissolution time. Hence, the model is insensitive to the temperature range used to vary the CpE beyond a certain critical range.
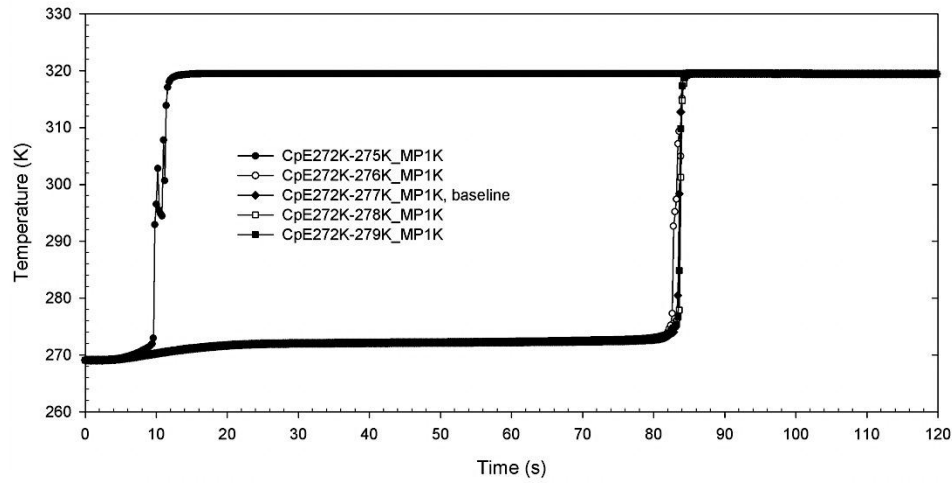
Figure 6.21 Effect of the effective specific heat window (CpE range) on the dissolution kinetics

6.3.2.2.3 Material Property Variation during Melting

Another important aspect influencing the dissolution time for the model is the temperature range over which viscosity, permeability (function of liquid fraction), density and conductivity are varied, referred as MP here. **Figure 6.22** shows the temperature prediction for the cases where the temperature range over which above mentioned material properties are varied, 0.5 K to 5 K. For example, 'CpE(272K-277K)_MP(0.5K)' suggests the melting range is from 272 K to 277 K while the MP varies from 276.5 K – 277 K. For the case where the MP is increased to 5 K consistent with the melting temperature range, the melting time is increased to 94 s i.e. ~12 s more than the baseline case. This is due to the formation of a boundary layer at the solid-liquid interface, which when large can significantly impede heat and mass transfer. For the other cases, no significant discrepancies were observed in the flow nor the dissolution time when compared to the baseline case MP(1K). The dissolution time for all cases except the MP(5K) case varied between 76 – 86 s. As can be observed no definite trend exists, the increase in dissolution time from MP(1K) to MP(2K) is ~3 s while from MP(2K) to MP(3K) is ~1 s suggesting a non-linear increase in time for 1 K increase in the material property variation range during melting.

89
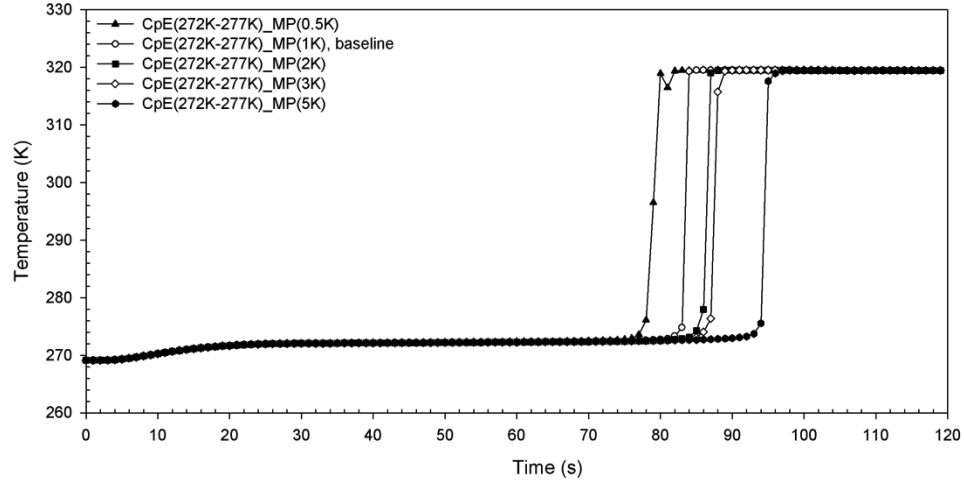
Figure 6.22 Effect of the melting temperature (MP) window on the dissolution kinetics

It is apparent from this sensitivity study that dissolution depends on the combination of many factors like solidus temperature, latent heat absorption range and range over which the other material properties are varied. The model is also sensitive to numerical parameters such as mesh size and time step. The selection of the solidus temperature determines the initiation of the absorption of latent heat while the selection of range over which liquid fraction and dynamic viscosity are varied determines the behavior at the solid-liquid interface thereby governing the end of the dissolution process. ANSYS CFX is a commercial package that has been adapted to model the dissolution process considered in this study. Considering the limitations of the package, like sensitivity to the latent heat absorption temperature range, the baseline model features are the result of careful formulation developed using the four experimental cases examined in this study and form the basis of an accurate dissolution model.

6.4   Application to the Al-Ti System

The model developed and validated for the ethanol/water system has been applied to the Al-Ti system to assess the model's applicability to the EBCHR process for Al/Ti-6Al-4V system. The ethanol/water model was modified by replacing the ethanol solute and water solvent with Aluminum and Titanium, respectively. This application of the model enables an assessment of the differences exhibited

between the two systems based on fluid flow during dissolution, temperature evolution for the solute and the solvent and solid-liquid interface profile. The ethanol/water experiments performed in this study are not directly analogous to the complex conditions that exist during EBCHR processing of Ti alloys because of differences in geometry, the electron-beam heat source, mass loss by evaporation, and heat losses at the boundaries. However, the two systems are influenced by the same fluid flow forces (buoyancy and Marangoni), which have been shown to govern the dissolution process. The application of the dissolution model in this section is an example of how the water/ethanol system can act as an analogue to a dissolution process, which involves temperature and composition dependent buoyancy and Marangoni forces.

The Al/Ti considers the same physics, assumptions, governing laws, domain and boundary conditions as described in Chapter 5, Section 5.1, 5.2, 5.3, 5.4 and 5.7 respectively. The geometry and the mesh size used are identical to the ethanol/water model formulation. The time step was changed to 0.001s to eliminate numerical instabilities.

The properties required for Al/Ti system include density, effective specific heat, dynamic viscosity and liquid fraction, thermal conductivity, diffusivity and surface tension coefficients based on temperature and composition. The thermo-physical properties used in the model for both Ti [89, 90] and Al [86, 89] are summarized in **Figure 6.23** and **Figure 6.24**, respectively.
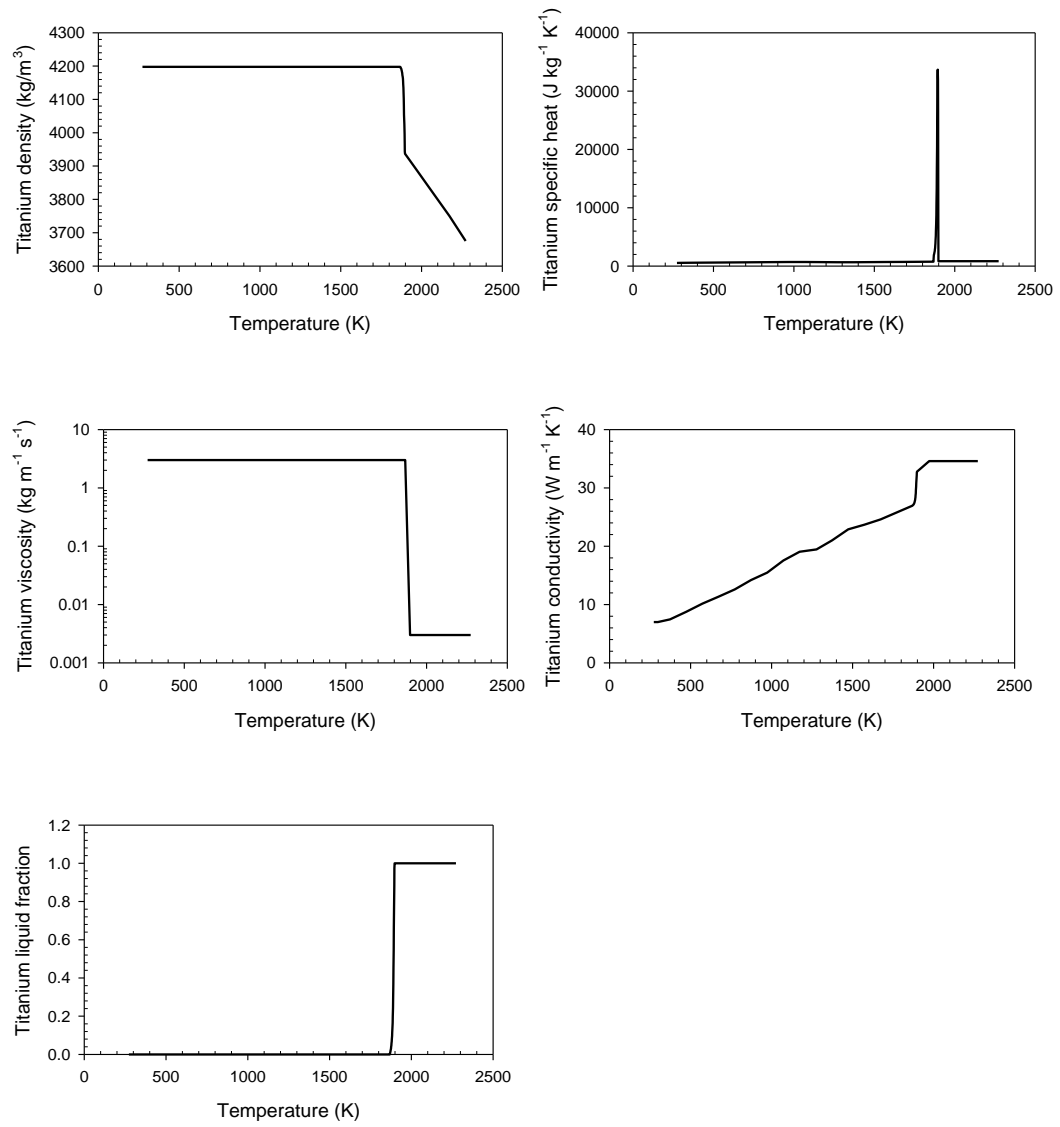
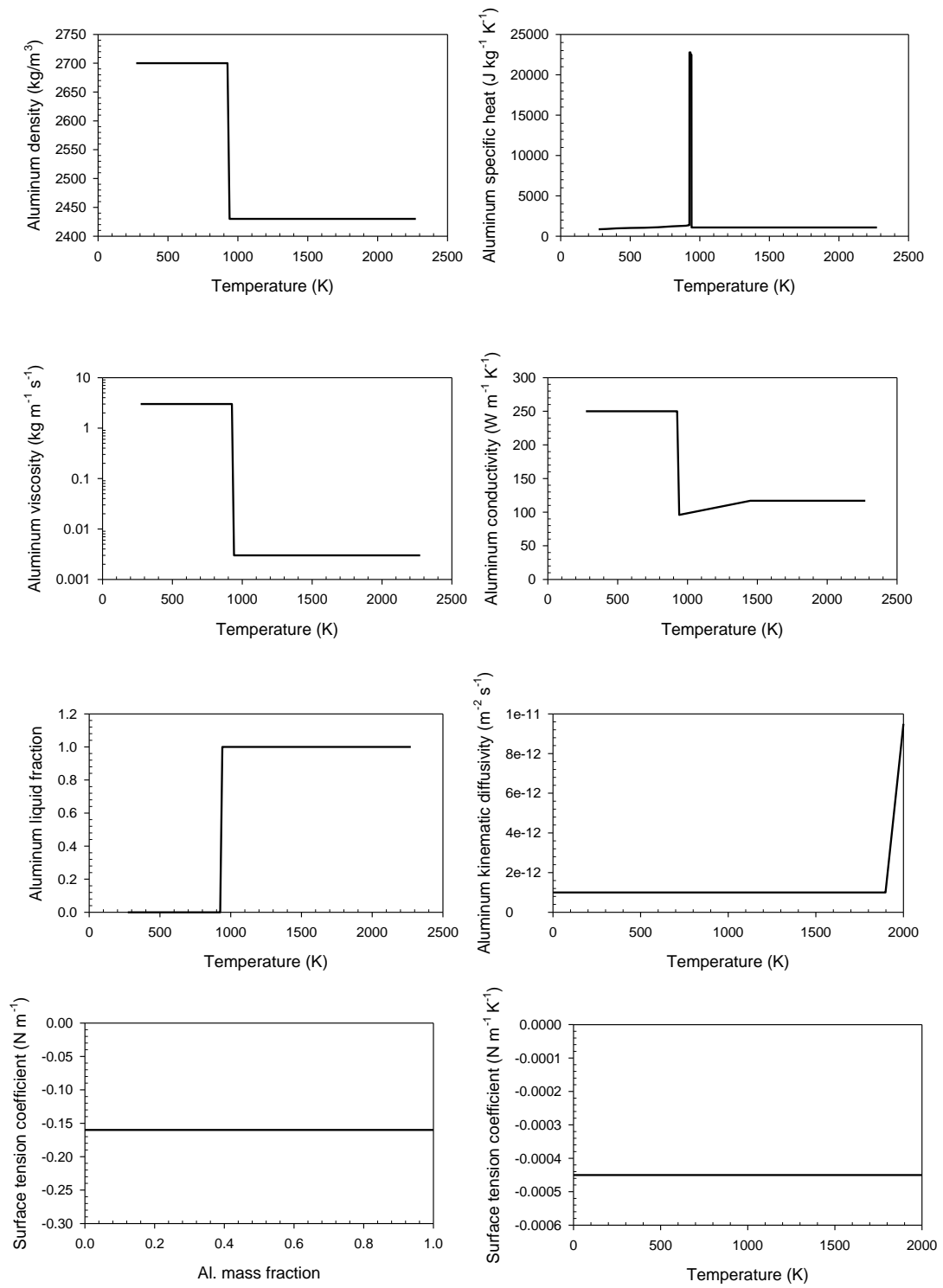**Figure 6.23 Thermo-physical properties of Titanium** [89, 90]

Figure 6.24 Thermo-physical properties of Aluminum [86, 89]

The aluminum solute and titanium solvent start with an initial temperature of 298 K and 2000 K, respectively. The temperature, solute mass fraction and dynamic viscosity contour plots with velocity vectors for the Al/Ti case are shown in **Figure 6.25**, **Figure 6.26** and **Figure 6.27**, respectively. Like Case IV of the ethanol/water system in section 6.1, this model considers the effect of thermal buoyancy, compositional buoyancy, thermal Marangoni and compositional Marangoni. Interestingly, the model highlights the influence and dominance of all four fluid drivers together at the same time but at different locations within the domain.

As in the ethanol/water cases (discussed in section 6.1.1) the large temperature difference between the solute and solvent results in hot Ti melt initially solidifying around the relatively cold Al solute. This is because of the low sensible heat of Ti above liquidus in comparison to Al. As Al pulls heat out from Ti, the temperature of Ti drops to liquidus and Ti starts to solidify. The freezing of Ti just adjacent to Al prevents mass and momentum transport across the interface but the thermal diffusion remains to be effective over time causing the solid Al to melt completely around the frozen case of solidified Ti.

The freezing of Ti leads to an increase in the density of Ti around Al, causing thermal buoyancy to dominate as in the ice/water cases, (Case I and II). Similarly, a decrease in temperature at and for near the interface increases the surface tension causing Marangoni forces that are directed inward and a preferential dissolution of the solid Al at the top, as previously observed in ice/water, case II. This phenomenon can be seen in the contour plots shown in **Figure 6.25-6.27** from 3 s to 12 s. At 12 s, the Ti solidified around the liquid Al melts away at the top, and the liquid Al moves upward due to its low compositional density. At this point, compositional buoyancy is dominant inside the solid Ti shell while on the other side of the Ti shell, thermal buoyancy continues to be dominant (refer to frames for 15 s and 16.5 s). The upward movement of Al decreases the surface tension at the top surface causing the compositional Marangoni forces to direct outward, as seen previously in ethanol/water (refer to Case IV).

From 15 s to 18 s, all four fluid flow forces are active and acting at different locations within the domain. At 18 s, the solid Ti lining (case) melts completely causing the thermal buoyancy and thermal

Marangoni forces to become reduced. The only influential fluid flow forces being active after 18 s are compositional buoyancy and compositional Marangoni.
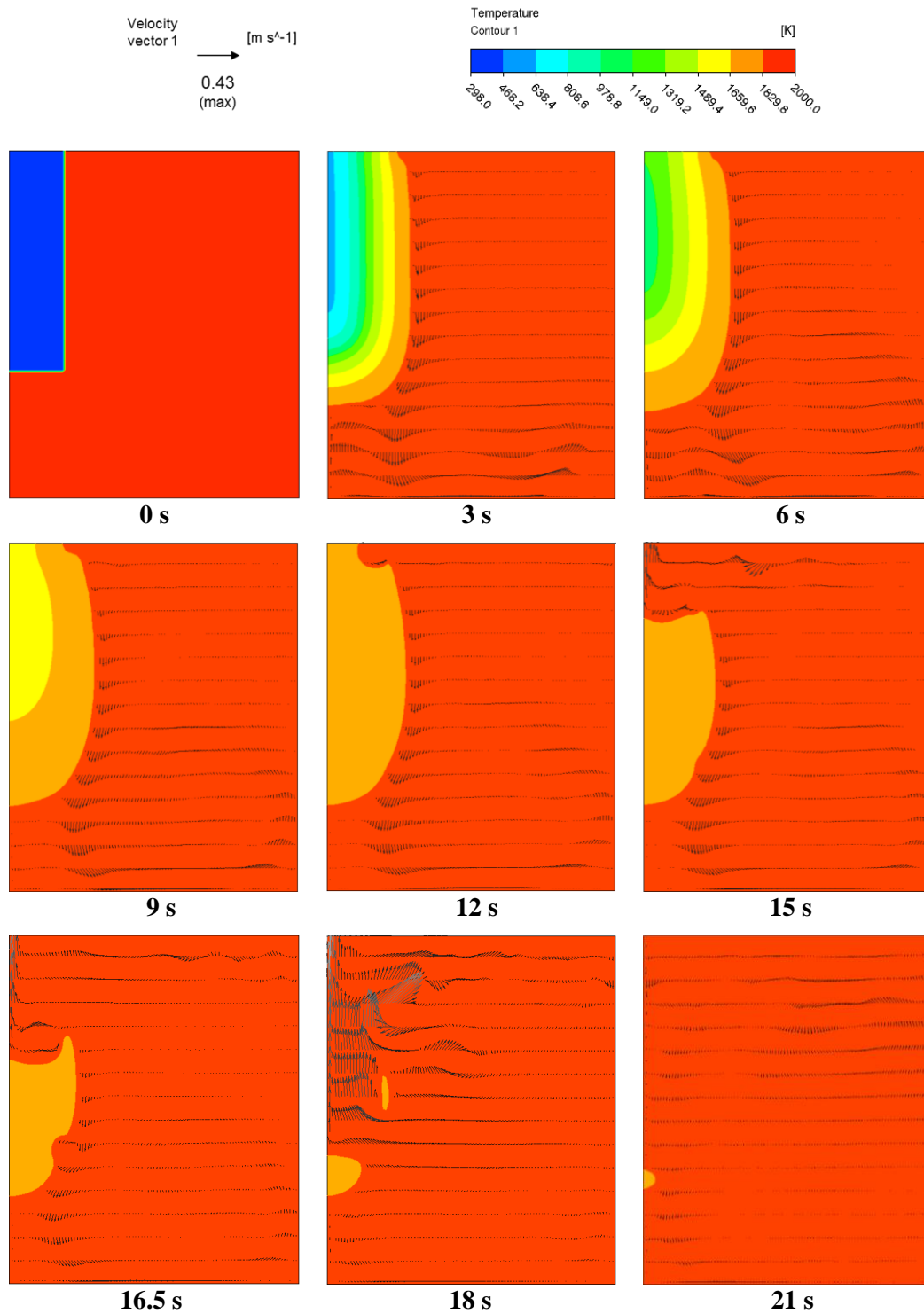
Figure 6.25 Al/Ti: Temperature distribution contour at every 3 seconds from the time of dipping
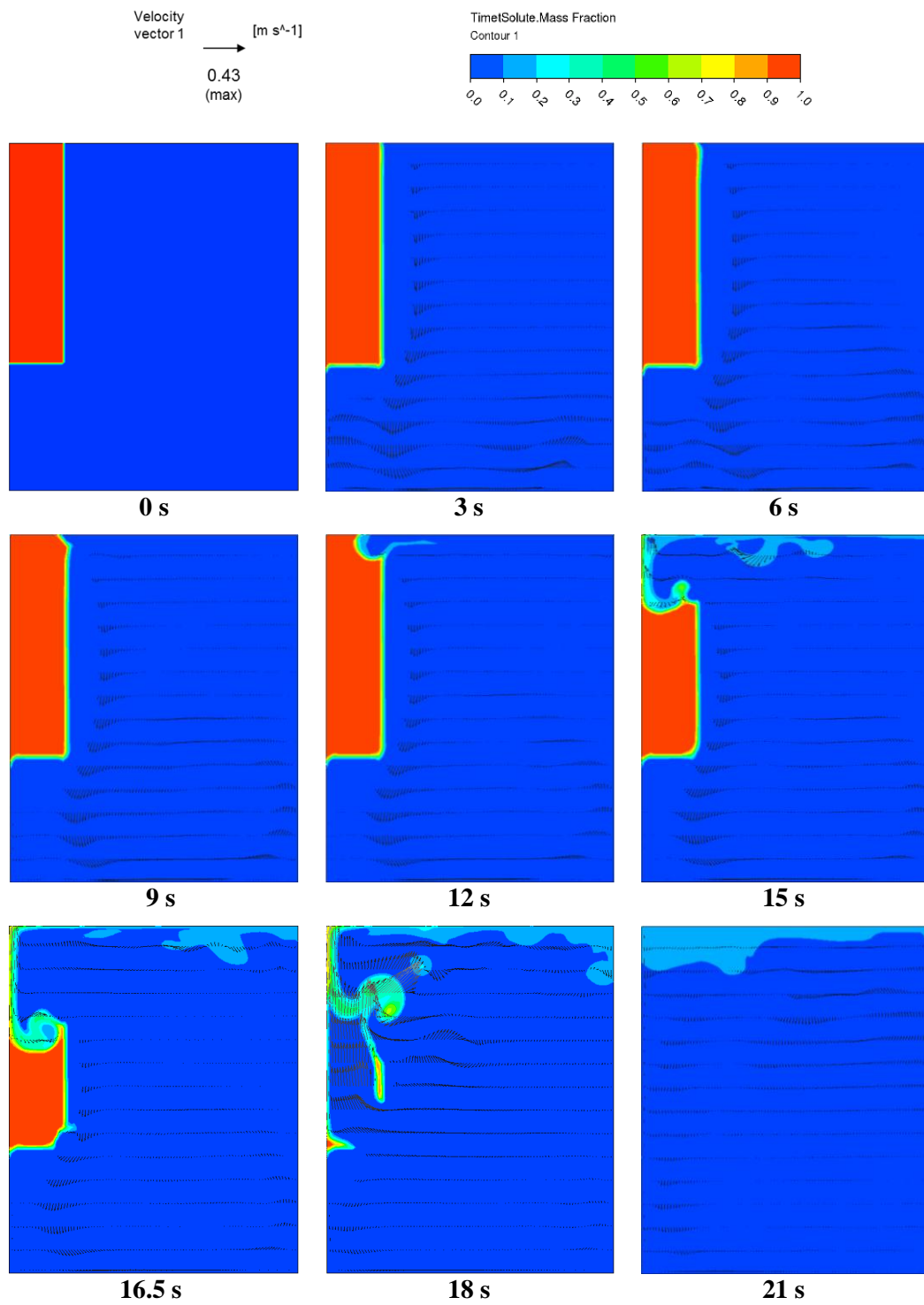
Figure 6.26 Al/Ti: Mass fraction contour at every 3 seconds from the time of dipping
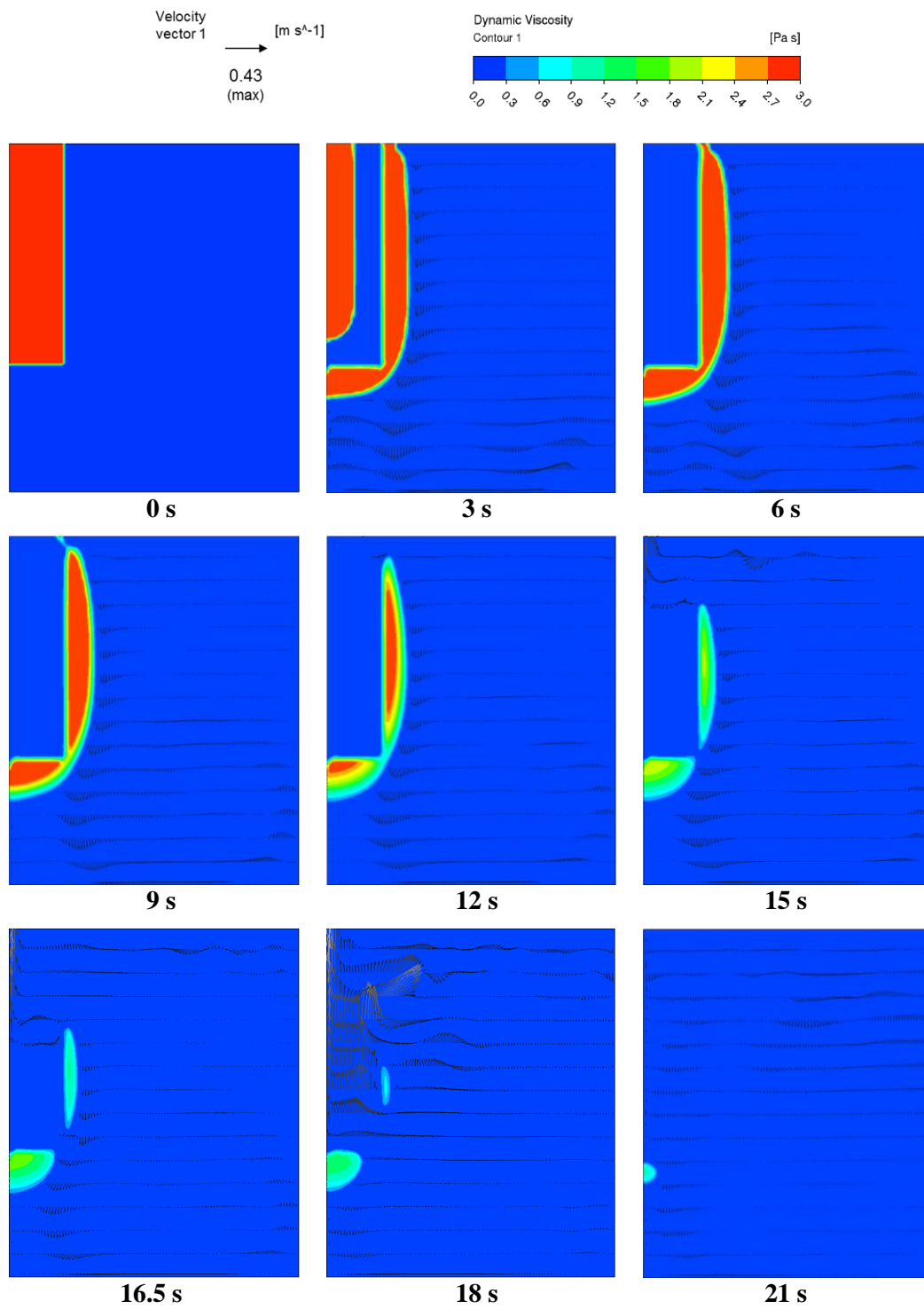
Figure 6.27 Al/Ti: Dynamic viscosity contour at every 3 seconds from the time of dipping

Figure 6.28 shows the temperature evolution at the center of the Al solute and in the Ti solvent. The temperature range over which the Al melts was assumed to be between 926 K and 941 K, i.e. a total of 15 K. Focusing on the Al temperature, there is an initial pause of 1 s after which the Al starts to heat up and a rapid increase in the temperature can be observed from 298 K at 1 s to 926 K at 5.7 s. The latent heat required to melt the Al is being supplied by the solidified Ti. As the Al melts, the solid Ti shell holds the Al melt inside while the temperature continues to increase. It is not until 12.5 s that the movement of Al across the interface initiates and mixes into the Ti melt by advection (dominant) and diffusion.
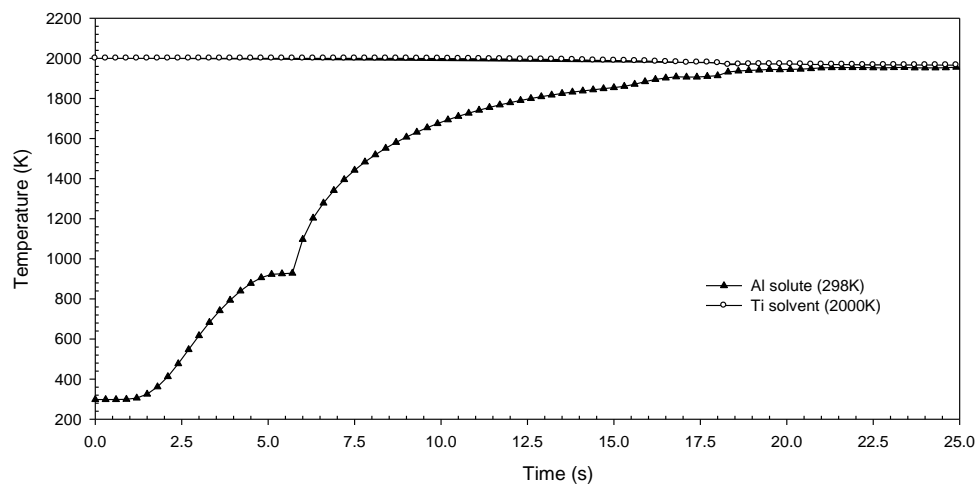
Figure 6.28 Al/Ti: Model prediction of the temperature evolution curve of Al (solute) dissolution in Ti (solvent)

7 Summary and Conclusions

7.1 Summary

In this study, an ethanol-water physical analogue model was developed to simulate the conditions present during the dissolution Al in Ti during electron beam cold hearth re-melting process. The experiment was formulated to develop an understanding of the influence of thermal buoyancy, thermal Marangoni, compositional buoyancy and compositional Marangoni forces. The physical modeling procedure involved dipping solidified ethanol or water (ice), acting as solute, in to water contained in a beaker. Since the fluid flow forces that are active depend on the thermo-physical properties of the material being dissolved, its concentration, and its location in the water solvent pool, it was possible to enhance or reduce Marangoni forces by changing the depth that the solute was dipped and to switch the compositional effects on or off by changing the solute.

3-D computational model of the physical analogue experiment was developed based-on the commercial CFD software package ANSYS CFX 12.0. The effects of thermal and compositionally driven buoyancy and surface tension (Marangoni) flows have been included in the model. The model also includes Darcy damping forces within the two-phase solid-to-liquid transition regime. The computational model was successfully validated by comparison with detailed experimental data from the ethanol-water analogue experiments. The computational model was used to quantify the fluid flow, temperature and compositional profiles during dissolution and to assess the influence of key process parameters, material properties, and numerical parameters.

The computational model was then modified for application the Ti-Al system by replacing the material properties of solid ethanol by Al and water by molten Ti. The same geometry and mesh size as the physical analogue experiments were employed for this analysis. The results showed the influence of the four types of Marangoni and buoyancy fluid flow forces that have been studied in this work. The results were consistent with expectations and provide support for the continued development of a multi-component thermo-fluid-compositional dissolution model for application to industrial processing conditions.

7.2 Conclusions

The coupled thermal-composition-fluid flow model developed in this work is capable of predicting the dissolution and homogenization process which occurs when a solid material is introduced into a liquid with a higher temperature. Comparing the data from the ice/water and ethanol/water cases indicates that the combination of thermal and compositional driven forces greatly change the fluid flow pattern and dissolution kinetics in comparison to a system with only thermal induced forces. It has also been shown in both the experiment and the model that for the pure ethanol in water case, composition buoyancy and Marangoni forces dominate those of thermal buoyancy and Marangoni forces.

From the experimental work it was concluded that a material positioned at the surface of a melt will take longer to dissolve compared to one which is completely immersed in the solvent. This is consistent with the change in surface area of the solute (ice or ethanol) exposed to the liquid solvent. It was also concluded that the freezing of the solvent around the solute material during dissolution does not occur if the amount of sensible heat above liquidus for the solvent is high.

The characteristic temperature plateau observed in the measured and predicted solute temperature data, as well as its duration are caused by the solid-to-liquid phase change and can be altered by modifying the relevant material property data such as the solid-to-liquid transformation temperature range, the latent heat of melting and the temperature range over which viscosity and permeability (material properties governing the formation of boundary layer at the solid/liquid interface) are varied.

7.3 Future Work

To bridge the gap between conditions present in the physical analogue experiments conducted in this work and industrial EBCHR processing, lab-scale experiments on the Al / Ti system should be conducted. The EB button melting facility available in the Advanced Materials Processing Engineering Laboratory at UBC could be used for these experiments. Similar to the ice/water and ethanol/water cases, quantitative measurement of temperature, composition, fluid flow and velocity should be sought and used to validate a computational model of these experiments. Quantifying the solid-liquid interface profile and

it's evolution during button melting experiments will be difficult in the Al-Ti system because of the high temperatures, vacuum environment and opacity of the system. To address these issues, interrupted dissolution experiments should be performed where the Al solute is dipped for a short duration and then removed from the pool. The shape of the solute can be compared with the model results for validation.

Like the ice/water case presented in this work, an experiment with solid Ti dipped into a liquid pool of Ti should be performed to study the effects and dominance of the temperature dependent Marangoni and buoyancy forces in the metal system. The basic Al-Ti model developed in this work highlighted the issue of freezing a layer of Ti solvent around the Al solute. It would be interesting to see if similar conditions occur with the Al / Ti-6Al-4V system in the EB button furnace.

The Al/Ti application based model discussed in Chapter 6, section 6.4 is required to be further developed by adding more complexities into the system which were not involved or significant in the ethanol/water system. Some of the important aspects which are needed to be considered/ included into the dissolution model are:

1) The effect of electron beam heat source at the top surface.

2) Replace the material properties of solvent from commercial pure Ti to Ti-6Al-4V alloy.

3) The effect of mass loss due to the evaporation of Al during the EBCHR of Ti-6Al-4V,

4) Alpha-beta phase transformation feature for Ti-6Al-4V alloy,

5) Heat transfer along the boundaries.

Another important thing to notice is that in ethanol/water, the water starts at a fixed temperature, the initial velocity is also fixed to 0 m/s and the initial pressure is set to 0 Pa which will not be the case with the Al/Ti system. This is because the electron beam heat source is used to melt the Ti solvent pool to a temperature below liquidus. This operation is performed in a vacuum environment. Also the continuously exposed moving/fixed beam on the solvent pool surface generates a high velocity, complex temperature and compositional fields within the pool. Hence prior to the dipping event, such an atmosphere will required to be developed and input as an initial condition into the model to generate such complex velocity, temperature and compositional fields at time 0 seconds.

Finally, it would be interesting to see the change in the flow pattern, dissolution time and behavior with Al being allowed to melt in Ti from different depths, like: partial or complete immersion of the Al solute into the Ti bath. And validate if the flow features and solid-liquid interface profile show certain analogy to the ethanol/water work.

8 Bibliography

[1] R. C. Picu and A. Majorell, "Mechanical behavior of Ti–6Al–4V at high and moderate temperatures—Part II: constitutive modeling," *Materials Science and Engineering: A,* vol. 326, pp. 306-316, 3/31, 2002.

[2] Technical data sheet - Titanium alloy Ti-6Al-4V. *CRS Holding Inc.* 2006. Available: http://cartech.ides.com/datasheet.aspx?i=101&E=269.

[3] A. Majorell, S. Srivatsa and R. C. Picu, "Mechanical behavior of Ti–6Al–4V at high and moderate temperatures—Part I: Experimental results," *Materials Science and Engineering: A,* vol. 326, pp. 297-305, 3/31, 2002.

[4] M. J. Donachie and J. Matthew, *Titanium: A Technical Guide.* ASM International, 2000.

[5] S. K. Kar, "Modeling of mechanical properties in alpha/beta-titanium alloys," pp. 1-226, 2005.

[6] K. Wilhelm, "Method for manufacturing titanium and alloys thereof," 2205854, 1940.

[7] E. H. Kraft. Summary of emerging titanium cost reduction technologies. EHK Technologies. Vancouver, WA. 2004, Available: http://www.ornl.gov/sci/propulsionmaterials/pdfs/Emerging_Titanium.pdf.

[8] T. Saito, K. Wakabayashi, S. Yamashita and M. Sasabe, "Production of Fe–Ti–Si alloys from the ilmenite ore and their magnetic properties," *J. Alloys Compounds,* vol. 388, pp. 258-261, 2/22, 2005.

[9] F. Habashi, Ed., *Handbook of Extractive Metallurgy.* Weinham: John Wiley & Sons Ltd., 1997.

[10] G. Lütjering and J. C. Williams, *Titanium.* Heidelberg: Springer - Verlag, 2007.

[11] International Titanium Association. Titanium: The ultimate choice. pp. 22. 2010. Available: http://www.titanium.org/chinese/Resources/Titanium%20The%20Choice.pdf.

[12] L. Toho Titanium Co., "Available at: www.toho-titanium.co.jp. " 2010.

[13] K. Suzuki, "An introduction to the extraction, melting and casting technologies of titanium alloys," *Metals and Materials International,* vol. 7, pp. 587-604, 2001.

[14] G. Ghazal, A. Jardy, P. Chapelle and Y. Millet, "On the Dissolution of Nitrided Titanium Defects During Vacuum Arc Remelting of Ti Alloys," *Metallurgical and Materials Transactions B,* vol. 41, pp. 646-659, 2010.

[15] W. H. Chang, R. A. Sprague and J. A. Stahl, "Method for the dispersion of hard alpha defects in ingots of titanium or titanium alloy and ingots produced thereby," 4622079, March 22, 1985.

[16] National Materials Advisory Board, NRC, "Titanium: Past, present and future," National Academy Press, Washington D.C., Tech. Rep. NMAB-392, 1983.

[17] P. Yuan, S. Shesh and O. Y. Kuang, "Electron beam melting and plasma arc melting," in *Modeling for Casting and Solidification Processing, Materials Engineering*, pp. 613-653, 2002.

[18] G. Z. Chen, D. J. Fray and T. W. Farthing, "Direct electrochemical reduction of titanium dioxide to titanium in molten calcium chloride," *Nature,* vol. 407, pp. 361-364, Sep 21, 2000.

[19] E. Crist, K. Yu, J. Bennett, F. Welter, B. Martin and S. Luckowski, "Manufacturing of PAM only processed titanium alloys," in Hamburg, Germany, 2003.

[20] J. Bellot, D. Ablitzer and E. Hess, "Aluminum volatilization and inclusion removal in the electron beam cold hearth melting of Ti alloys," *Metallurgical and Materials Transactions B,* vol. 31, pp. 845-854, 2000.

[21] B. Lautrup, *Physics of Continuous Matter, Exotic and Everyday Phenomena in the Macroscopic World.* Taylor & Francis, 2004.

[22] L. E. Scriven and C. V. Sternling, "The Marangoni Effects," *Nature Publishing Group,* vol. 187, pp. 186-188, 16 July 1960.

[23] P. D. Lee, P. N. Quested and M. McLean, "Modelling of Marangoni effects in electron beam melting," *Philosophical Transactions of the Royal Society of London. Series A: Mathematical, Physical and Engineering Sciences,* vol. 356, pp. 1027-1043, April 15, 1998.

[24] A. W. Woods, "Melting and dissolving," *J. Fluid Mech.,* vol. 239, pp. 429-448, 1992.

[25] T. Hibiya, T. Azami, M. Sumiji and S. Nakamura, "Surface Tension Driven Flow of Molten Silicon: Its Instability and the Effect of Oxygen," *Interfacial Fluid Dynamics and Transport Processes, Lecture Notes in Physics,* vol. 628, pp. 131-155, 2003.

[26] A. Eyer, H. Leiste and R. Nitsche, "Crystal growth of silicon in space lab - I: Experiments ES-321," in *Proceeding of Vth European Symp. Materials and Fluid Sciences in Microgravity,* Schloss-Elmau, Germany, 1984, pp. 173-182.

[27] K. C. Mills, B. J. Keene, R. F. Brooks and A. Shirali, "Marangoni Effects in Welding," *Philosophical Transactions: Mathematical, Physical and Engineering Sciences,* vol. 356, pp. 911-925, 1998.

[28] S. Shad, I. D. Gates and B. B. Maini, "Investigation and visualization of liquid–liquid flow in a vertically mounted Hele-Shaw cell: flow regimes, velocity and shape of droplets," *Measurement Science and Technology,* vol. 20, pp. 114005, 2009.

[29] A. C. Powell IV. Transport phenomena in electron beam melting and evaporation. *Ph. D Thesis, Massachusetts Institute of Technology* pp. 1-205. 1997. Available: http://hdl.handle.net/1721.1/39623.

[30] J. Bellot, D. Ablitzer, B. Foster, A. Mitchell, S. Hans and E. Hess, "Dissolution of hard-alpha inclusions in liquid titanium alloys," *Metallurgical and Materials Transactions B,* vol. 28, pp. 1001-1010, 1997.

[31] O. Velde, R. Grundmann and F. Rüdiger, "Theoretical and experimental investigations of electron beam surface remelting and alloying," *Metallurgical and Materials Transactions B,* vol. 31, pp. 1405-1417, 2000.

[32] D. Simon and U. Pal, "Mathematical modeling of a melt pool driven by an electron beam," *Metallurgical and Materials Transactions B,* vol. 30, pp. 515-525, 1999.

[33] Y. P. Lei, H. Murakawa, Y. W. Shi and X. Y. Li, "Numerical analysis of the competitive influence of Marangoni flow and evaporation on heat surface temperature and molten pool shape in laser surface remelting," *Computational Materials Science,* vol. 21, pp. 276-290, 7, 2001.

[34] T. L. Bergman and B. W. Webb, "Simulation of pure metal melting with buoyancy and surface tension forces in the liquid phase," *Int. J. Heat Mass Transfer,* vol. 33, pp. 139-149, 1, 1990.

[35] G. Goldschmied, E. K. Tschegg and A. Schuler, "Electron beam surface melting-numerical calculation of the melt geometry and comparison with experimental results," *J. Phys. D,* vol. 23, pp. 1686-1694, 1990.

[36] H. Yin and T. Emi, "Marangoni flow at the gas/melt interface of steel," *Metallurgical and Materials Transactions B,* vol. 34, pp. 483-493, 2003.

[37] C. Karcher, R. Schaller, T. Boeck, C. Metzner and A. Thess, "Turbulent heat transfer in liquid iron during electron beam evaporation," *Int. J. Heat Mass Transfer,* vol. 43, pp. 1759-1766, 5/15, 2000.

[38] K. W. Westerberg, M. A. McClelland and B. A. Finlayson, "Finite element analysis of flow, heat transfer, and free interfaces in an electron-beam vaporization system for metals," *International Journal for Numerical Methods in Fluids,* vol. 26, pp. 637-655, 1998.

[39] S. Semiatin, V. Ivanchenko and O. Ivasishin, "Diffusion models for evaporation losses during electron-beam melting of alpha/beta-titanium alloys," *Metallurgical and Materials Transactions B,* vol. 35, pp. 235-245, 2004.

[40] I. Langmuir, "The vapor pressure of metallic tungsten," *Phys. Rev.,* vol. 2, pp. 329-342, 1913.

[41] A. Powell, U. Pal, J. Van Den Avyle, B. Damkroger and J. Szekely, "Analysis of multicomponent evaporation in electron beam melting and refining of titanium alloys," *Metallurgical and Materials Transactions B,* vol. 28, pp. 1227-1239, 1997.

[42] V. Ivanchenko, O. Ivasishin and S. Semiatin, "Evaluation of evaporation losses during electron-beam melting of Ti-Al-V alloys," *Metallurgical and Materials Transactions B,* vol. 34, pp. 911-915, 2003.

[43] S. Akhonin, N. Trigub, V. Zamkov and S. Semiatin, "Mathematical modeling of aluminum evaporation during electron-beam cold-hearth melting of Ti-6Al-4V ingots," *Metallurgical and Materials Transactions B,* vol. 34, pp. 447-454, 2003.

[44] A. Guillou, J. P. Bars, E. Etchessahar, J. Debuigue and D. Charquet, "Dissolution du nitrure de titane dans le titane liquide et dans le TA6V," in *The Sixth Conf. on Titanium,* Cannes (France), 1988, pp. 697-699.

[45] R. N. Jarret, "Removal of defects from titanium alloys with E.B.C.H.R." in *Proc. Conf. on Electron Beam Melting and Refining - State of the Art - Edited by R. Bakish,* New Jersey (USA), 1986, pp. 332-346.

[46] R. N. Jarret, S. H. Reichman and R. G. Broadwell, "Defect removal mechanisms in hearth melted ti-6Al-4V," in *Proc. 6th World Conf. on Titanium,* Cannes, France, 1988, pp. 593-598.

[47] D. Ablitzer, "Transport phenomena and modelling in melting and refining processes," *J. Phys. IV France,* vol. 03, pp. 873-882, 1993.

[48] J. P. Bellot, A. Jardy, S. Bourguignon and D. Ablitzer, "Modelling of ti alloy melting by EBCHM: Impact of process parameters for hard alpha dissolution," in *RTO AVT Workshop on "Intelligent Processing of High Performance Materials",* Brussels, Belgium, 1998, pp. 12.1-12.8.

[49] J. P. Bellot, E. Floris, A. Jardy and D. Ablitzer, "Numerical simulation of the E.B.C.H.R. process," in *Conf. on Electron Beam Melting and Refining - State of the Art, Edited by R. Bakish,* RENO (USA), 1993, pp. 139-152.

[50] J. P. Bellot and A. Mitchell, "Hard-alpha particle behaviour in a titanium alloy liquid pool," in *Proc. Conf TMS,* San Francisco (USA), 1994, pp. 1.187-1.193.

[51] G. Ghazal, P. Chapelle, A. Jardy, J. Jourdan and Y. Millet, "Dissolution of High Density Inclusions in Titanium Alloys," *ISIJ International,* vol. 52, pp. 1-9, 2012.

[52] C. A. Heiple and J. R. Roper, "Mechanism for minor element effect on GTA fusion zone geometry," *Welding J.,* vol. 61, pp. 975, 1982.

[53] C. Limmaneevichitr and S. Kou, "Experiments to simulate effect of Marangoni convection on weld pool shape," *Welding Journal Newyork,* vol. 79, pp. 231-237, 2000.

[54] H. A. Joseph, P. W. Cleary, M. Prakash, V. Alguine, T. Nguyen and C. Scott, "SPH, MAGMAsoft and water analogue modeling of die fillings of a servo piston," in *Third International Conference on CFD in the Minerals and Process Industries,* CSIRO, Melbourne, Australia, 2003, pp. 587-592.

[55] P. W. Cleary, J. Ha, M. Prakash and T. Nguyen, "3D SPH flow predictions and validation for high pressure die casting of automotive components," *Appl. Math. Model.,* vol. 30, pp. 1406-1427, 11, 2006.

[56] B. G. Thomas, R. O'Malley, T. Shi, Y. Meng, D. Creech and D. Stone, "Validation of fluid flow and solidification simulation of a continuous thin-slab caster," in *Modeling of Casting, Welding, and Advanced Solidification Processes IX,* Shaker Verlag, GmbH, Aachen, Germany, 2000, pp. 769-776.

[57] Lan, X.K., Khodadadi, J.M., "Fluid flow, heat transfer and solidification in the mold of continuous casters during ladle change," *International Journal of Heat and Mass Transfer,* vol. 44, pp. 953-965, 2001.

[58] M. Reza Aboutalebi, R. I. L. Guthrie and S. H. Seyedein, "Mathematical modeling of coupled turbulent flow and solidification in a single belt caster with electromagnetic brake," *Appl. Math. Model.,* vol. 31, pp. 1671-1689, 8, 2007.

[59] R. Guthrie, "Mathematical and physical modelling of steel flow and solidification in twin-roll/horizontal belt thin-strip casting machines," *Applied Mathematical Modelling,* vol. 22, pp. 851-872, 1998.

[60] L. Shuaijun, X. Shoumei, M. Li and J. Allison, "Numerical simulation of air entrapment phenomenon during mold filling of high pressure die casting process," *Acta Metallurgica Sinica,* vol. 46, pp. 554-560, 2010.

[61] W. D. Bennon and F. P. Incropera, "A Continuum Model for Momentum, Heat and Species Transport in Binary Solid-Liquid Phase Change Systems: I. Model Formulation," *International Journal of Heat Mass Transfer,* vol. 30, pp. 2161 - 2170, 1987.

[62] W. D. Bennon and F. P. Incropera, "A Continuum Model for Momentum, Heat and Species Transport in Binary Solid-Liquid Phase Change Systems: II. Application to Solidification in a Rectangular Cavity," *International Journal of Heat Mass Transfer,* vol. 30, pp. 2171-2187, 1987.

[63] D. G. Neilson and F. P. Incropera, "Unidirectional solidification of a binary alloy and the effects of induced fluid motion," *Int. J. Heat Mass Transfer,* vol. 34, pp. 1717-1732, 7, 1991.

[64] C. Beckermann and R. Viskanta, "An Experimental Study of Solidification of Binary Mixtures with Double-Diffusive Convection in the Liquid," *Chemical Engineering Communications,* vol. 85, pp. 1-135, 1989.

[65] W. D. Bennon and F. P. Incropera, "The Evolution of Macrosegregation in Statically Cast Binary Ingots," *Metallurgical Transactions B,* vol. 18B, pp. 611-616, 1987.

[66] F. P. Incropera, A. H. H. Engel and W. D. Bennon, "Numerical Analysis of Binary Solid-Liquid Phase Change with Buoyancy and Surface Tension Driven Convection," *Numerical Heat Transfer,* vol. 16, pp. 407-427, 1989.

[67] F. P. Incropera, "Effect of buoyancy and externally induced forces on the solidification of binary mixtures," School of Mechanical Engineering, Purdue University, Indiana, Tech. Rep. DOE/ER/13759 - T1, 1997.

[68] M. McCay, T. McCay and J. Hopkins, "The nature and influence of convection on the directional dendritic solidification of a metal alloy analog, NH_4Cl, and H_2O," *Metallurgical and Materials Transactions B,* vol. 24, pp. 669-675, 1993.

[69] A. Ecker, D. Frazier and J. Alexander, "Fluid flow in solidifying monotectic alloys," *Metallurgical and Materials Transactions A,* vol. 20, pp. 2517-2527, 1989.

[70] H. Dharwadkar and A. Ghosh, "An ice-water model study on formation of blowhole-free skin with reference to solidification of steel," *Metallurgical and Materials Transactions B,* vol. 17, pp. 553-564, 1986.

[71] J. Mahmoudi and M. Vynnycky, "Modelling of fluid flow, heat transfer and solidification in the strip casting of copper base alloy (I). Water model," *Scandinavian Journal of Metallurgy,* vol. 30, pp. 21-29, 2002.

[72] A. D'Aubeterre, R. Da Silva and M. E. Aguilera, "Experimental study on Marangoni effect induced by heat and mass transfer," *Int. Commun. Heat Mass Transfer,* vol. 32, pp. 677-684, 4, 2005.

[73] M. A. Mendes-Tatsis and D. Agble, "The Effect of Surfactants on Marangoni Convection in the Isobutanol/Water System," *Journal of Non-Equilibrium Thermodynamics, Walter De Gruyter,* vol. 25, pp. 239-249, 2001.

[74] S. Dehaeck, C. Wylock and P. Colinet, "Evaporating Cocktails," *Phys. Fluids,* vol. 21, pp. 091108-1, 2009.

[75] R. C. Weast, *CRC Handbook of Chemistry and Physics.* CRC Press, Inc., 1981.

[76] "Physical data of Thermal Fluids - Water, " http://www.celsius-process.com/pdf/eau.pdf," *Celsius Process - Manufacturer of Process Equipment for the Chemical Industry,* pp. 1, 2010.

[77] "Physical data of Thermal Fluids - Ethanol," http://www.celsius-process.com/pdf/ethanol.pdf," *Celsius Process - Manufacturer of Process Equipment for the Chemical Industry,* pp. 1, 2010.

[78] J. Jian-Zhong Li. Study of liquid metals by electrostatic levitation. *Doctor of Philosophy, California Institute of Technology* pp. 1-96. 2010.

[79] K. Kalazhokov, Z. Kalazhokov and K. Khokonov, "Surface tension of pure aluminum melt," *Technical Physics,* vol. 48, pp. 272-273, 2003.

[80] ANSYS, Ed., *User Guide for ANSYS CFX 11.0.* 2006.

[81] R. B. Bird, W. E. Stewart and E. N. Lightfoot, *Transport Phenomena.* John Wiley & Sons, Inc., 2006.

[82] X. Zhao, D. M. Maijer, S. L. Cockcroft, D. Tripp, S. Fox and J. Zhu, "A three-dimensional steady state thermal fluid model of ingot casting process associated with electron beam melting of ti-6Al-4V," in *Proceedings of the 11th World Conference on Titanium,* Kyoto, Japan, 2007, pp. 1271-1274.

[83] S. Henke, P. Kadlec and Z. Bubník, "Physico-chemical properties of ethanol – Compilation of existing data," *J. Food Eng.,* vol. 99, pp. 497-504, 8, 2010.

[84] G. Vhquez, E. Alvarez and J. M. Navaza, "Surface Tension of Alcohol Water + Water from 20 to 50 degree.C," *J. Chem. Eng. Data,* vol. 40, pp. 611-614, 1995.

[85] H. Ohkubo, T. Murakami, Y. Yamazaki and R. Chandratilleke, "Crystal growth of ethanol water solution [for thermal energy storage]," in *Energy Conversion Engineering Conference and Exhibit, 2000. (IECEC) 35th Intersociety,* 2000, pp. 1019-1025 Vol.2.

[86] M. D. Lane, "A coupled thermal - fluid flow model of the horizontal direct chill casting process for T-ingot ," *Master of Applied Science - MASc, Materials Engineering,* pp. 1-101, 2007.

[87] W. Simpson and A. TenWolde, "Physical properties and moisture relations of wood, wood handbook - wood as an engineering material," USDA Forest Service, Forest Products Laboratory, Madison, WI, Tech. Rep. GTR-113:, 1999.

[88] M. Jeng, "The Mpemba effect: When can hot water freeze faster than cold?" *American Journal of Physics,* vol. 74, pp. 514-522, 2006.

[89] K. C. Mills, *Recommended Values of Thermophysical Properties for Selected Commercial Alloys.* Woodhead Publishing, 2002.

[90] T. Meng. Factors influencing the fluid flow and heat transfer in electron beam melting of Ti-6Al-4V. *Master of Applied Science - MASc, Materials Engineering* pp. 1-105. 2009.